A Single-Stage Reusable Launch Vehicle Concept

Abbos Yunusov

A thesis submitted in partial fulfillment of the requirements for the degree of

Master of Science in Aeronautics & Astronautics

University of Washington

2014

Reading Committee:

Kuen Lin
Dana Andrews
Adam Bruckner

Program Authorized to Offer Degree:
Department of Aeronautics & Astronautics

University of Washington

Abstract

A Heavy-Lift Reusable Single-Stage Launch Vehicle Concept

Abbos M. Yunusov

Chair of the Supervisory Committee:
Professor Kuen Y. Lin
Aeronautics & Astronautics

A reusable VTVL (vertical take-off, vertical landing), all-rocket SSTO (single-stage-to-orbit) launch vehicle is proposed to reduce the cost of space transportation. The concept vehicle is based on presently-existing or near-term technology, and incorporates several features to improve performance, including all-composite construction, lightweight pressure-stabilized tankage, and the use of a HIAD (hypersonic inflatable aerodynamic decelerator) - an inflatable heatshield - to return from orbit. Several different types of main engines, consuming various fuels, are considered. An ad-hoc MATLAB code is used to predict the empty mass of the vehicle, quantify the sensitivity of the design to empty mass growth, and the system life-cycle cost. A vehicle powered by tripropellant engines based on RD-701/RD-704 technology consuming liquid oxygen and liquid hydrogen and methane fuels is identified as the best performer.

Table of Contents

LIST OF FIGURES

LIST OF TABLES

Acknowledgments

I would like to thank the members of my thesis supervisory committee - the chair, Professor Kuen Y. Lin, as well as Professor Adam P. Bruckner and Dr. Dana G. Andrews - for their invaluable assistance in the preparation of this thesis.

Dedication

To my father

Chapter 1: Introduction

1.01: Motivation

The exploitation of space has the potential to yield enormous profits. However, with present-day means of space launch - various expendable rockets, characterized by costs of thousands of dollars per kilogram to orbit - the expense of launching the many heavy payloads needed to support activities such as asteroid mining is prohibitive. It is therefore desired to develop a new means of space launch - one which is technologically feasible and economically attractive.

1.02: Focus and scope

This study is concerned with determining the suitability of a certain reusable, rocket-powered VTVL SSTO concept for this application. Such a vehicle lifts off vertically from the surface of the Earth in the familiar manner. After ascending to orbit and deploying its payload, it deorbits itself, reenters the atmosphere, and restarts some of its main engines to perform a vertical powered landing - a liftoff in reverse.

The concept isn't a single specific design, but rather many variations on a theme, each with a common overall configuration and basic design features and varying parameters - i.e. the number and type of engines, thrust-to-weight ratio, etc.

The vehicle is capable of delivering a positive payload to a 200 km, 19.4°-inclination orbit. This corresponds to a putative launch site in the southern Big Island of Hawaii. It is capable of completing its mission and returning even in the event of a failure of any individual main engine at any point during the ascent, combined with one failing to start for the landing burn. The vehicle has no other abort modes.

Although only rocket engines are considered, results are obtained for designs using various types of engines and fuels. These include both single and dual-fuel designs, the latter either with two types of bipropellant ascent engine, or with tripropellant engines. These results are of interest since the various fuels considered have differing advantages and disadvantages - for example, liquid hydrogen offers the highest possible specific impulse, while denser hydrocarbon fuels allow a savings on structural mass and even a reduction in the V_{Δ} to orbit, due to decreased ascent losses.

1.03: Overview of methodology/objectives of study

The analysis proceeds from the standpoint of obtaining quantitative answers to three primary questions:

1. Can it be built?
2. How challenging will it be to develop?
3. How much will it cost?

The first question is addressed through mass analysis. The assumptions of the analysis allow the ascent performance to be determined entirely by several "external" parameters - for example, the number and type of engines and the desired takeoff thrust-to-weight ratio, from which follows the gross lift-off mass. The time-varying propellant consumption rates are integrated over the course of the ascent to obtain total quantities. Allowances are made for losses and to provide an ascent performance reserve, and for on-orbit and recovery (deorbit and landing) maneuvers. The empty mass of the vehicle is the sum of several component/subsystem masses, determined using a combination of physics-based and empirical models, plus a growth allowance, with the results of the mission simulation as inputs. The payload is whatever remains of the starting mass after the propellants and empty mass have been deducted - if this figure is positive, the design is considered to be feasible.

The second question is addressed by determining the empty mass growth characteristics. All aerospace vehicles experience mass growth during development. A small initial increase in the mass of some component may lead to a considerably greater total mass increase, due to the redesign necessary to accommodate it. (For example, a subsystem that proves heavier than anticipated will require the airframe to be beefed up to support it - and then beefed up a bit more to support its own increased weight, and so on.) Rocket-powered SSTOs are particularly vulnerable to this phenomenon. Here, sensitivity to mass growth is quantified as the change in empty mass with respect to a change in the payload mass [01].

The third question is addressed by determining the life-cycle program costs, with emphasis on the payload mass specific figure. The life-cycle cost is modeled as the sum of several component costs - non-recurring development costs, and recurring hardware production, propellant and operations costs. The recurring costs are modified by learning-curve effects, and computed on both a discounted and undiscounted basis.

There is also the question of which among the propellant combinations and main engines considered yields the best results.

All analytical methods are implemented as ad-hoc MATLAB codes. Dimensional quantities are in SI units. Many of the charts in this report are in a vector-based format. Readers of the electronic version may zoom in to examine them more closely without any loss in quality.

1.04: Overview of thesis

This thesis consists of five chapters and three appendices. Chapter 2 discusses the generalities of the problem, describes the key technologies, and includes several analyses demonstrating necessary capabilities. Chapter 3 describes the analytical methodology in more detail. Chapter 4 includes the key results obtained and their analysis. Chapter 5 presents the general conclusions and recommendations of this report.

004

Chapter 2: Preliminary discussion

2.01: Concept of operations

2.01.01: CONOPS/mission description

The vehicle is a VTVL (vertical take-off, vertical landing) SSTO. Its general features are as follows:

1. Unitary/single-stage configuration
2. Pure rocket propulsion
3. Vertical take-off
4. Ballistic direct ascent
5. Base-first reentry
6. Vertical powered landing

The mission flight phases include:

1. Vertical take-off from a prepared launch facility equipped with hold-down, flame-trench and sound-suppression.
2. Ascent to a 200 km circular orbit.
3. Deployment of payload in LEO.
4. A 24-hour wait in orbit for reentry phasing
5. An OMS deorbit burn
6. Maneuvering hypersonic glide
7. Post-hypersonic terminal flight
8. Powered vertical landing

The vehicle is capable of completing the following maneuvers:

1. Ascent to 200 km altitude and near-circular (within 100 m/s) velocity using its main engines
2. Various OMS burns, to include both the circularization and deorbit burns, of V_{Δ} = 200 m/s total
3. Various RCS burns of V_{Δ} = 100 m/s in total
4. A landing burn of V_{Δ} = 200 m/s, using restarted main engines, to cancel its terminal velocity and provide a few seconds of hover time

The vehicle is capable of completing its mission and returning even in the case of any individual main engine failing at any point during the ascent, followed by another failing to restart for the landing burn.

The vehicle operates unmanned.

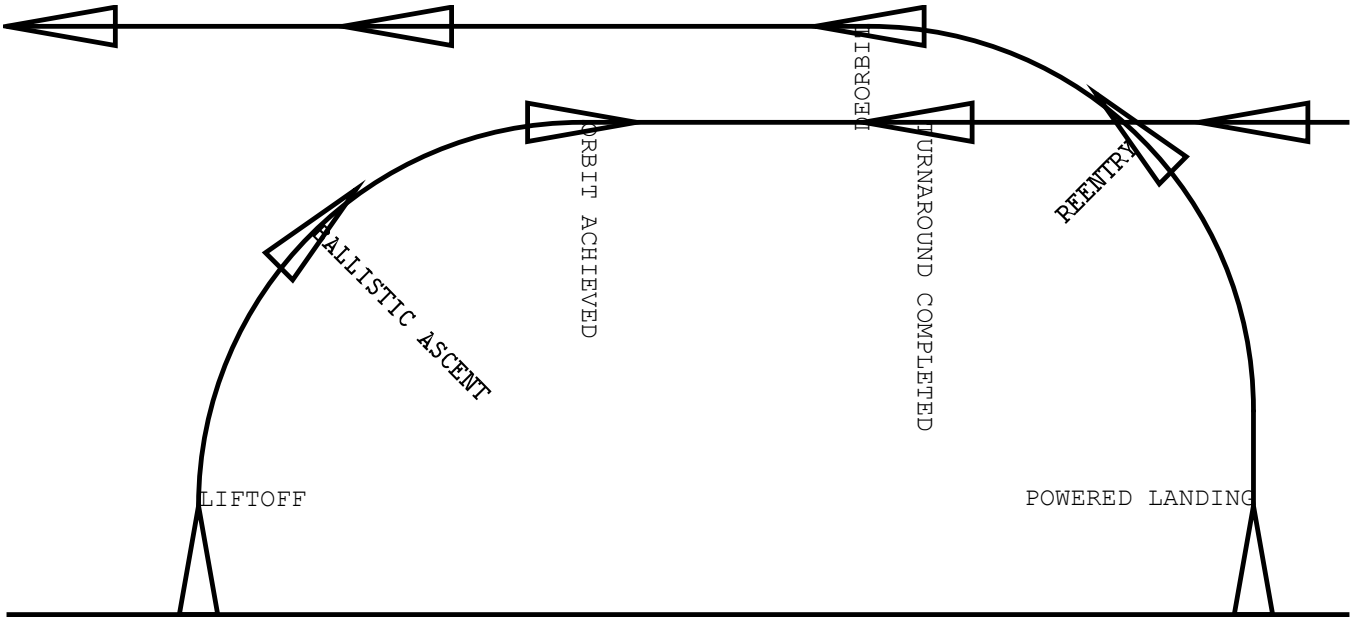

Figure 2.01.01-01: Illustration of CONOPS

2.01.02: Implications of CONOPS

A single-stage vehicle is more challenging to develop than one with two or more stages. It may nevertheless achieve lower transportation costs, due to its lower empty mass relative to payload than a TSTO. There is also no duplication of hardware (i.e. ascent engines or landing gear) between stages, and no need to arrange for the recovery of multiple stages.

The improvement in specific impulse offered by airbreathing is offset by several major disadvantages. For example, air-breathing vehicles require air intakes, which are heavy, draggy and complicated to engineer. They cannot take direct-ascent trajectories to orbit, but must linger at altitudes where there is sufficient air to operate in an air-breathing mode as they accelerate through their velocity range, which subjects the airframe to severe aeroheating and mechanical loads. To avoid losing altitude, they must be capable of generating aerodynamic lift, which requires either wings or lifting-body geometry. Finally, since airbreathing engines cannot operate at all above a certain altitude, an airbreathing vehicle will require some sort of rocket capability to complete its ascent anyway. As a result, airbreathers are heavier and more complicated - and therefore more challenging to develop and expensive - than their pure-rocket counterparts. In addition, suitable hypersonic airbreathing propulsion technology has yet to be demonstrated, while rocket technology has been capable of the necessary performance for decades.

The combination of vertical takeoff and base-first reentry ensures that ground-support and reentry drag loads are introduced to the vehicle structure in the same location and with the same orientation as the engine thrust loads. All these loads are reacted - not simultaneously - by the thrust structure, which must already be stressed for the main engine thrust. With this concept, as shown in Chapter 4, the structure is about a quarter of the empty mass.

Prior to lift-off, the vehicle is supported by its hold-down points at all times. The landing gear is extended only for landing and serves mostly to support the empty vehicle after it has touched down. This restricts the vehicle to operating from fixed pads. However, this is not a major disadvantage for something intended only as an efficient cargo transporter, as opposed to a military system. For example, multiple markets can be served by transporting their payloads to one of a few central launch sites, as opposed to performing launches from many different sites. It also permits a considerable savings on the mass of the landing gear, which need only be sized for about the empty weight of the vehicle, as there is also no RTLS abort mode.

Base-first reentry has several major advantages, which are detailed in Section 2.04 of this chapter. For example, it eliminates the need to perform a turn-around maneuver to orient the vehicle for the landing burn. It has the major disadvantage that the vehicle will have a very low lift-to-drag ratio during reentry, and therefore very limited cross-range capability. It will therefore have to remain in orbit for up to 24 hours for reentry phasing if it is to return to its original launch site. The main engines will also require protection.

2.02: Ascent

2.02.01: Flight physics of ascent

The performance of a rocket is described by the famous Tsiolkovsky equation [02]:

$$00. \rightarrow \quad V_{\Delta} = c_E \ln\left(\frac{m_0}{m_1}\right)$$

V_{Δ}, the "delta-V" or change in velocity, characterizes both the performance of a rocket vehicle and the performance required to fly on some trajectory or complete some maneuver. c_E, the effective exhaust velocity, characterizes the efficieny of the engine. The ratio m_0/m_1 is the ratio between the mass of the vehicle at the start and end of the burn, the difference being the mass of propellant consumed.

The thrust [02] is given by

$$01. \rightarrow \quad F_T = \dot{m}_P c_E$$

where $\dot{m}_P$ is the mass flow rate. The higher the effective exhaust velocity, the lower the mass flow rate required to produce a given thrust. The effective exhaust velocity depends primarily on the propellant chemistry, the design of the engine, and the ambient pressure. Rockets perform less well at sea level than in a vacuum, since the ambient pressure limits expansion through the nozzle. The weight-specific impulse I_S [02] is given by

$$02. \rightarrow \quad c_E = g_0 I_S$$

where $g_0 = 9.80665\ m/s^2$ is the standard gravity. Specific impulse has dimensions of time and is given in seconds. Engine performance is usually quoted in terms of specific impulse. This avoids the trouble of dealing with different unit systems.

The rocket equation may be rearranged into the form

$$03. \rightarrow \quad \frac{m_0}{m_1} = \exp\left(\frac{V_\Delta}{c_E}\right)$$

which provides the mass ratio needed to achieve some V_Δ given some c_E.

It is also useful to define a stage propellant mass fraction

$$04. \rightarrow \quad \zeta = \frac{m_P}{m_E + m_P}$$

where m_E is the empty mass of the stage and m_P is the mass of propellant it carries.

Including losses, the V_Δ required to achieve a low-Earth orbit is on the order of 9600 m/s. A modern engine, burning liquid oxygen and hydrogen, might achieve a vacuum I_S of 460 s, which corresponds to a mass ratio of approximately 8.40:1 for a single-stage vehicle. Assuming no payload, the vehicle will require a $\zeta = 0.8810$, which is a quite high value - and this is the bare minimum, with no provisions for recovery, performance reserve, etc.

A reusable single-stage vehicle will require additional V_Δ and hardware (thermal protection, landing gear, etc.) for recovery, and should be capable of carrying at least some payload.

These requirements increase the complexity and required mass ratio/propellant mass fraction further. The aerospace industry has therefore shied away from reusable stages.

2.02.02: Benefits of dense propellants

It is instructive to consider each of the three terms of the Tsiolkovsky equation as they individually pertain to rocket SSTOs. The necessary performance is attained with some combination of specific impulse and mass ratio that provides sufficient V_Δ.
Naively, LO2/LH2 (hydrolox) might be considered the "natural" propellant combination for an SSTO, as hydrolox engines have the highest specific impulse of any practical chemical rocket engines, thereby minimizing the required mass ratio. This is not necessarily the case [03].

First, hydrolox has a low "bulk density." A unit mass of propellant, as the engine consumes it, consists of both fuel and oxidizer at a certain ratio. Its bulk density is given by

$$05. \rightarrow \quad \rho_B = \frac{\Omega + 1}{\frac{1}{\rho_F} + \frac{\Omega}{\rho_X}}$$

where ρ_F is the density of the fuel, ρ_X is the density of the oxidizer, and Ω is the oxidizer-to-fuel ratio. Hydrolox engines generally operate at $\Omega \approx 6$, for a bulk density of $\rho_B = 362$ kg/m^3, a relatively low value. Kerolox (LO2/RP-1), by comparison, has a bulk density of $\rho_B = 1020$ kg/m^3. A higher bulk density tends to reduce empty weight and improve the propellant mass fraction, due to the reduction in the necessary volumetric capacity of the propellant tanks and the improved thrust-to-weight ratio of the engines, whose turbopumps scale in size and mass with the volumetric flow rate.

In addition, the use of dense propellants can actually lower the V_Δ to orbit by reducing ascent losses [03]. The total V_Δ to orbit has four major components:

1. Apogee velocity
2. Gravity losses
3. Drag losses
4. Back-pressure losses

The apogee velocity is the largest component of the total. It is only possible to maintain such a velocity above the sensible atmosphere. Gravity losses are associated with the work necessary to raise the vehicle to this altitude.

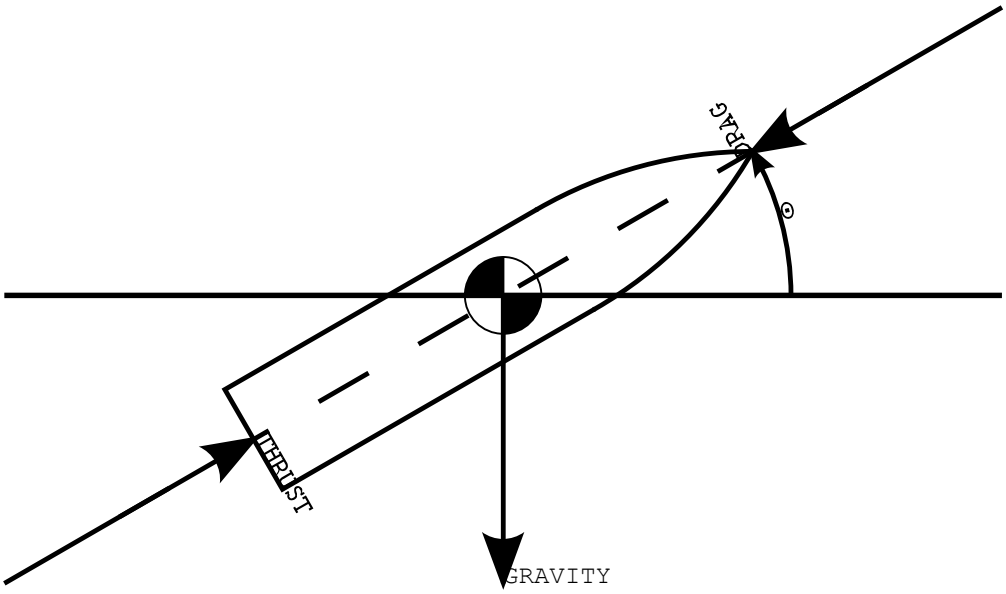

Figure 2.02.02-01: Free-body diagram for ascent flight

Consider a rocket in free flight. Neglecting aerodynamic drag, the force balance along its longitudinal axis is given by

$$06. \rightarrow \quad m_G \dot{V} = c_E \dot{m}_P - g m_G \sin\theta$$

where V is its velocity, m_G is its time-varying gross (total) mass, and θ is its flight-path angle. It is apparent that any vertical component of thrust means decreased downrange acceleration. The vehicle should follow an ascent trajectory in which it pitches over as early as possible, to allow it to achieve the necessary downrange velocity with minimum losses. It can only begin pitching over once it has acquired a sufficient vertical velocity component to avoid prematurely falling back to Earth. The use of dense propellants can reduce these losses.

Consider the case of two SSTO rockets, both starting at the Earth's surface and having identical starting masses, and maximum engine thrusts (and therefore liftoff thrust-to-weight ratios). They are started at the same time and must reach the same target orbit. One has hydrolox and the other kerolox engines [03]. Due to its lower specific impulse, the kerolox vehicle must have a higher mass flow rate than the hydrolox vehicle to produce the same thrust. It will therefore always have a lower mass - and therefore greater thrust-to-weight ratio and acceleration - than the hydrolox vehicle. It is said to have a steeper mass line. It will be able to pitch over, begin accelerating downrange, and reach the desired velocity sooner, and therefore experience fewer losses [03].

This can be demonstrated by constructing a simplified model of the ascent of the two vehicles and numerically integrating the equations of motion to determine the requirements and the ascent losses. The rotation of the Earth is neglected, and the vehicles are modeled as point masses following a zero-lift/gravity-turn ascent trajectory. The atmosphere is isothermal, with standard sea-level conditions and an 8000 meter scale height. The drag coefficient of both vehicles is assumed to remain constant. Note that the kerolox vehicle has a smaller base diameter/frontal area than the hydrolox vehicle, due to the smaller diameter/higher frontal thrust density of its engines. The engines are throttled to avoid exceeding a instantaneous thrust-to-mass limit and a variable (per design) dynamic pressure limit.

Table 2.02.02-01: Simulation parameters

	Hydrolox (scheme 1)	Kerolox (scheme 2)
Surface gravity	9.80665 m/s^2	9.80665 m/s^2
Scale height	8000 m	8000 m
Sea-level ambient pressure	101325 Pa	101325 Pa
Sea-level ambient density	1.2250 kg/m^3	1.2250 kg/m^3
Starting mass	1876 MT	1876 MT
Starting T/W	1.15	1.15
Base diameter	20.9 m	15.24 m
Drag coefficient	0.50	0.50
Dynamic pressure limit	25 kPa	20 kPa
I_S (sea—level/vacuum)	297.0 s/331.0 s	366.0 s/452.3 s

Table 2.02.02-02: Ascent results

	Hydrolox vehicle	Kerolox vehicle
Apogee velocity	7698 m/s	7699 m/s
Losses, gravity	1490 m/s	1394 m/s
Losses, drag	272 m/s	224 m/s
Losses, back-pressure	215 m/s	106 m/s
Total V_Δ	9793 m/s	9540 m/s
Mass ratio	9.103:1	18.927:1

The plotted trajectories terminate at 100 km altitude, although the apogee is higher. Note that the kerolox vehicle follows a shallower trajectory.

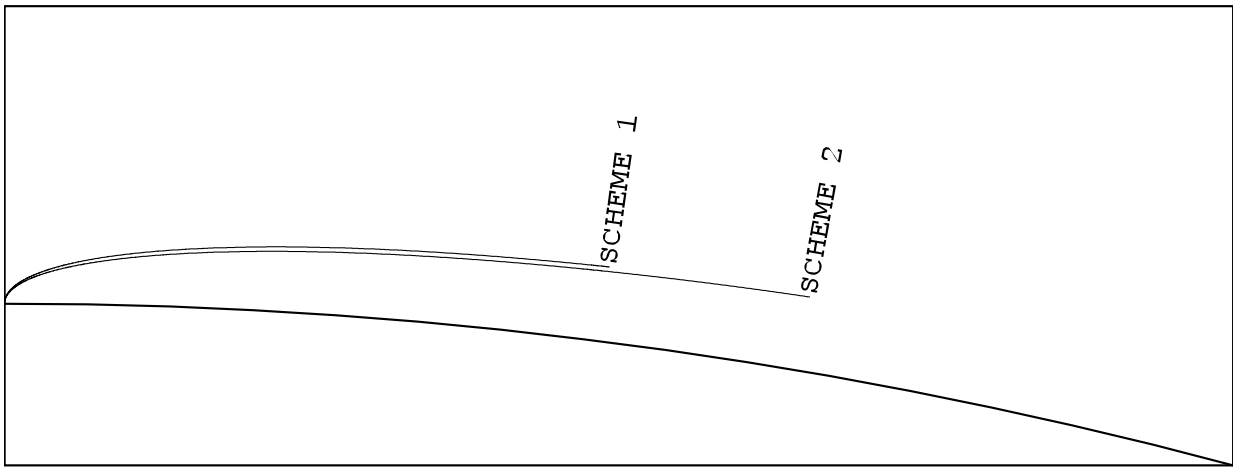

Figure 2.02.02-02: Ascent trajectories of hydrolox and kerolox vehicles

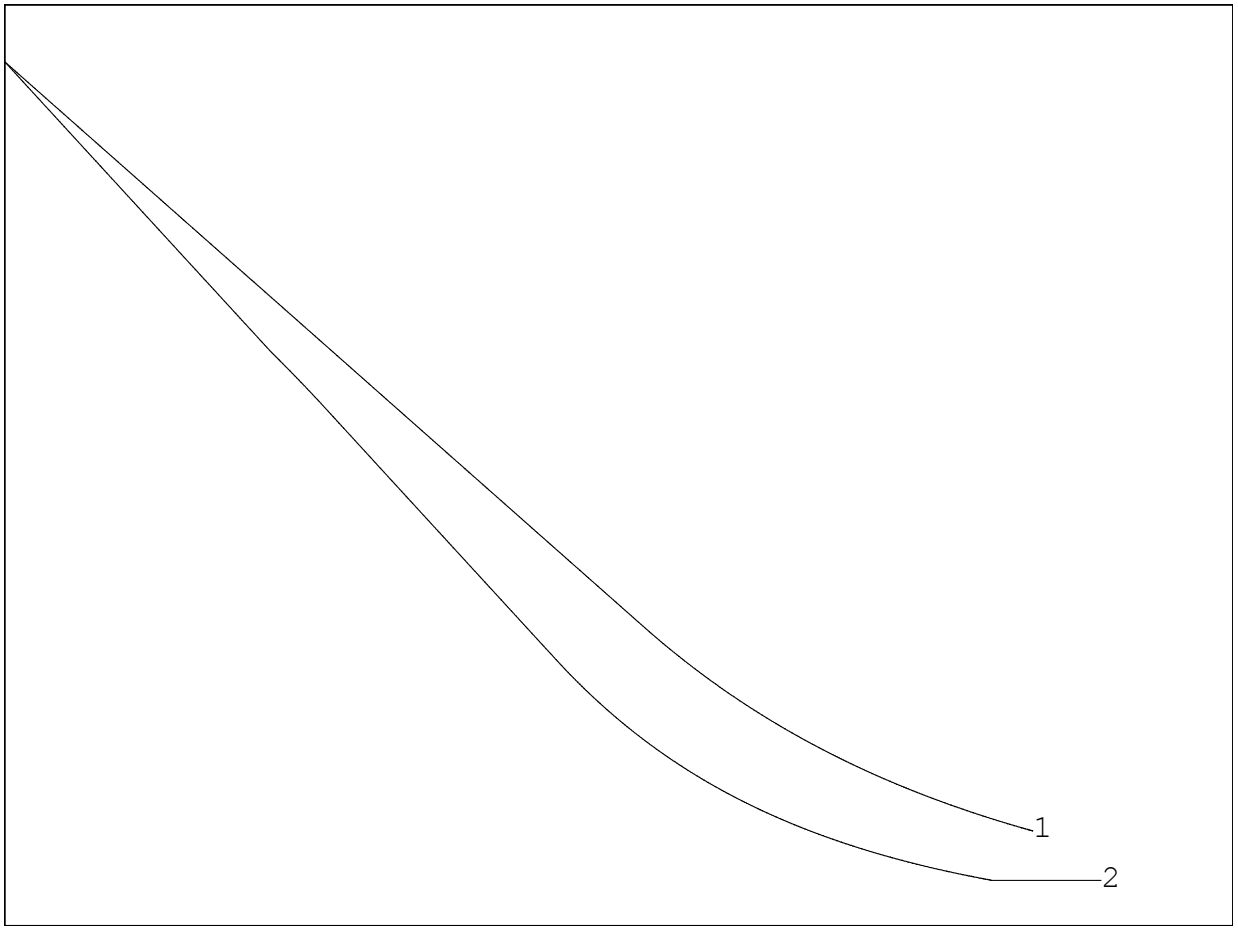

Figure 2.02.02-03: Gross mass histories of hydrolox and kerolox vehicles

These results show that the use of dense propellants can reduce the ascent V_{Δ} requirements.

It is also possible to make use of both propellant combinations on a single vehicle, either by using two types of engines - hydrocarbon-fueled booster engines and hydrolox sustainers - or with a tripropellant engine, in order to improve the specific impulse while retaining a high bulk density.

2.02.03: Mass ratios

Several 1950s/1960s-era rocket stages have had very high propellant mass fractions, similar to what would be required in this application. The most noteworthy example is the first generation of Atlas rockets. In their ancestral form, they were "1.5STO" or "stage-and-a-half" vehicles, since they employed ground-started parallel boosters fed from the core stage, which were jettisoned during the ascent [04].

The core stage included very thin stainless-steel pressure-stabilized integral tanks. The designers thereby achieved a very low structural weight and a very high mass ratio/propellant mass fraction. For example, the CGM-16D Atlas-D [05] core stage had a gross mass of 113 050 kg and an empty mass of 2 347 kg, for $\zeta = 0.9792$. By comparison, the model kerolox vehicle in the previous section, assuming it required an additional 500 m/s for recovery at the same vacuum specific impulse, requires only $\zeta = 0.9546$ to complete its mission, albeit with zero payload. This demonstrates that rocket engines have adequate performance for an SSTO RLV application.

Although the required mass ratio is twice as high, it can be shown that, in theory, the kerolox vehicle will have, for a given payload capacity, a lower empty mass, as its structure and engines - which together comprise about half the empty mass - will be much lighter.

2.02.04: Illustrative example

The previous example served to demonstrate the existence of the dense-propellant effect and illustrate the theory. An additional example - less theoretical and more practical - is provided to demonstrate the effect on empty mass.

Here, the hydrolox and metholox propulsion schemes are compared. Each vehicle has a certain number of main engines - SSMEs or metholox-conversions of NK-33s, as detailed in Subsection 2.03.01 and Appendix A - at the reference size. These results are generated by the same code used to obtain the final results, which implements the methods described in Chapter 3.

Table 2.02.04-01: Input parameters and key mass results

SCHEME	HYDROLOX	METHOLOX
ENGINES	16	26
T/W_0	1.15	1.15
MASS, STARTING	2295744 kg	3764720 kg
MASS, EMPTY	202370 kg	166550 kg
MASS, STRUCTURE	50496 kg	43684 kg
MASS, MAIN PROPULSION	65795 kg	50598 kg
MASS, PAYLOAD	18047 kg	23869 kg
V_Δ	9673 m/s	9441 m/s

The metholox vehicle, at a lower empty mass, can transport a larger payload. Non-recurring costs, and engine and vehicle production costs - the latter of which are the bulk of program costs, as per the cost-estimating relations in Section 3.03, and as the results in Subsection 4.03.02 demonstrate - will be lower for the metholox vehicle.

As expected, the vehicle structure and main propulsion subsystems are lighter for the metholox vehicle than the hydrolox vehicle, due to the difference in bulk density and engine thrust-to-weight ratio. This mass savings $(22009\ \text{kg})$ accounts for about three-fifths of the total $(35820\ \text{kg})$ difference between the two vehicles. The metholox vehicle also benefits from the dense-propellant effect, as the 232 m/s difference in V_Δ between the two vehicles demonstrates.

The metholox vehicle does have a larger gross weight and consumes more ascent propellants, but this is of little significance, as propellants account for only a small part of the total program cost.

2.03: Propulsion

2.03.01: Main propulsion

A total of five main engine designs are considered:

1. RS-25 SSME (LO2/LH2) [06]
2. NK-33 (LO2/RP-1) [07]
3. RD-704 (LO2/LH2/RP-1 + LO2/LH2) [08]
4. Modified NK-33 (LO2/LCH4)
5. Modified RD-704 (LO2/LH2/LCH4 + LO2/LH2)

All are pump-fed, staged combustion liquid-propellant rocket engines, with fixed bell nozzles. They are gimbaled to provide thrust vector control on ascent. All engine types are assumed to be restartable for the landing burn if necessary, and capable of being throttled to the necessary low power level.

These engines do not necessarily exactly represent current designs, but are parametrized from various references. This application would require the development of new engines capable of withstanding a sufficient number of firings to be economical. It is assumed that such engines will have performance no worse than their baselines.

The NK-33 boosters in both mixed propulsion schemes have slightly lengthened (although with the same area ratio) nozzles, in order to ensure a common exit plane with the SSME sustainers.

The tripropellant engines have, in addition to one for the oxidizer, separate sets of pumps and injector orifices for each of the two fuels used. In Mode 1, the tripropellant mode, which is intended for use at low altitude, both sets of fuel pumps are operated. In Mode 2, the bipropellant mode, the hydrocarbon pumps are shut down, and the engine only consumes hydrogen fuel [08].

The main engines are scaled to the necessary thrust level from their respective reference sizes. The thrust-to-mass ratio and specific impulse are held constant, while the linear dimensions scale with the square root of the thrust. Reference main engine properties are given in Appendix A. In other words, the main engines are "rubberized." [09]

Different combinations of these engines are used. The propulsion schemes considered are:

1. Pure hydrolox (RS-25)
2. Pure kerolox (NK-33)
3. Pure metholox (Modified NK-33)
4. Mixed hydrolox/kerolox (RS-25 + NK-33)
5. Mixed hydrolox/metholox (RS-25 + Modified NK-33)
6. Tripropellant hydrokerolox (RD-704)
7. Tripropellant hydrometholox (Modified RD-704)

Where necessary, engine performance is estimated using the NASA CEA (Chemical Equilibrium with Applications) code [10]. Performance figures estimated using CEA are compared to published figures in order to obtain correction factors. The performance of the metholox NK-33 conversion is predicted by applying the ratio between the published specific impulse of the kerolox NK-33 and the value predicted by CEA, in order to account for nozzle losses, and the performance of both the hydrokerolox and hydrometholox RD-704s is predicted by comparison with CEA results and published figures for the SSME, which has a similar expansion ratio and chamber pressure.

2.03.02: Secondary propulsion

The vehicle uses an existing design of OMS engine - the RL10B-2. It is described in Appendix A. Two engines are installed, and are not scaled. For attitude control, the vehicle is equipped with a set of RCS thrusters. These are fed with pressurized gaseous oxygen (GO2) and gaseous hydrogen (GH2) from gaseous accumulators.

It is very difficult to feed both pump and pressure-fed engines from the same set of tanks, since it is unsafe to supply pump-fed engines with propellant at the very high pressures required for pressure-fed thrusters. In addition, with gaseous propellants, the inlets are always submerged and the propellant lines are always filled. All that must be done to fire the RCS thrusters is to open a regulator. Since high-pressure gas vessels are heavy for their (mass) capacity, the accumulators are only sized for about 60 seconds of continuous firing, and are periodically recharged with gas generated onboard from stored LO2 and LH2 by a gas generator. This gas has other uses - for example, to repressurize the integral tanks or to generate hydraulic power. The gas generators include combustion chambers, heat exchangers, turbines and gas compressors. They burn LO2 and LH2 to generate high-pressure GO2 and GH2. The combustion products are vented offboard.

The RCS thrusters are scaled down from an older variant of the RL10, the RL10-3A3. As RL10s are expander-cycle engines, a similar engine should be able to operate without pumps, provided it is supplied with gaseous propellants at the necessary temperature. The RCS thrusters are scaled on the basis of their thrust-to-mass ratio with the injected mass of the vehicle. The ratio is that of the thrust of the Marquardt R-40 RCS (3870 kN) of the Shuttle Orbiter to the on-orbit mass (109 000 kg) of that vehicle [62][81]. Reference properties are described in Appendix A.

2.04: Entry

2.04.01: Physics of entry

To estimate the conditions the vehicle will encounter and to determine general trends, reentry flight is modelled under the assumptions:

1. The re-entering vehicle is modelled as a point mass.
2. The curvature and rotation of the Earth are neglected.
3. The atmosphere is isothermal and its density exponentially decreases with altitude.
4. Aerodynamic drag is the only force acting on the vehicle.
5. The drag coefficient of the vehicle is constant.

Given these assumptions, the vehicle will maintain a constant horizontal flight-path angle γ. The basic equation of motion is

$$07. \rightarrow \quad \dot{V}_\infty = -\frac{0.5 A_D C_D V_\infty^2 \rho_\infty}{m_G}$$

where A_D is the drag reference area, C_D is the drag coefficient, m_G is the gross mass of the vehicle, V_∞ is the free-stream velocity, and ρ_∞ is the ambient density.

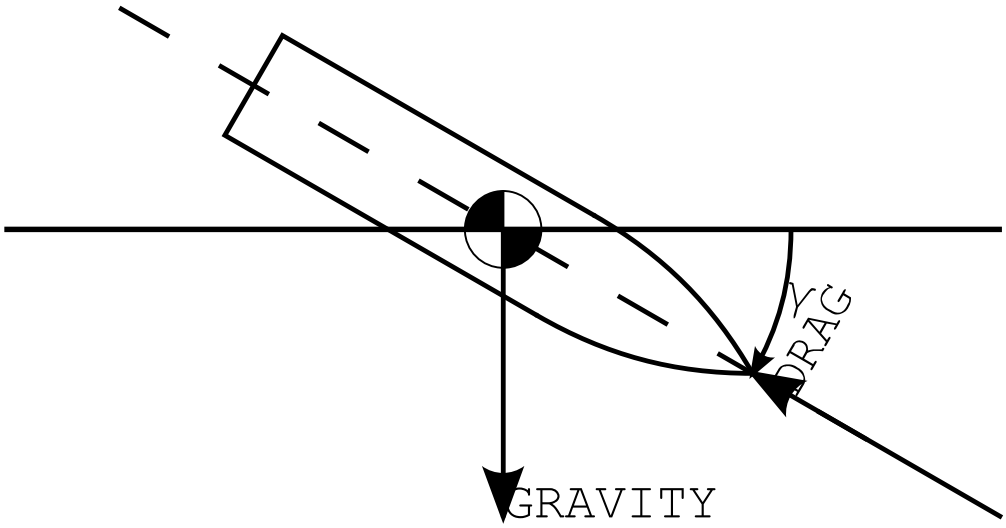

Figure 2.04.01-01: Free-body diagram for vehicle in reentry flight

The ballistic coefficient

$$08. \rightarrow \quad \beta = \frac{m_G}{A_D C_D}$$

characterizes the flight dynamics of a particular design. Leaving aside the details of the derivation, the equation of motion can be manipulated and integrated to obtain several useful expressions.

The maximum acceleration is given by

$$09. \rightarrow \quad \mathbf{a} = \frac{V_0^2 \sin\gamma}{2e\bar{z}}$$

where V_0 is the entry velocity, e is Euler's constant, and $\bar{z}$ is the scale height.

It occurs at an altitude

$$10. \rightarrow \quad z_{AMAX} = \bar{z} \ln\left(\frac{\bar{z}\rho_0}{\beta \sin\gamma}\right)$$

where ρ_0 is the sea-level density. Note that the maximum acceleration is sensitive only to the entry velocity and flight-path angle. The vehicle should reenter at the shallowest possible flight-path angle to keep the acceleration - for which the airframe must be stressed - within limits.

The windward surface is assumed to be a spherically-blunted right circular cone. At Earth-orbital reentry velocities, convective heating is the dominant mode of heat transfer. The maximum heating rate occurs at the stagnation point, which will be on the spherical segment.

It is approximately equal to

$$11. \rightarrow \quad \dot{q} = 1.83 \times 10^{-4} V^3 \sqrt{\frac{\rho_\infty}{r_{NOSE}}}$$

where r_{NOSE} is the nose radius. It has dimensions W/m^2. The total heat load per unit area, with dimensions J/m^2, is obtained by time integration.

The maximum heating rate occurs at an altitude

$$12. \rightarrow \quad z_{QMAX} = \bar{z} \ln\left(\frac{3\bar{z}\rho_0}{\beta \sin\gamma}\right)$$

and a velocity

$$13. \rightarrow \quad V_{QMAX} \approx 0.846 V_E$$

where V_E is the entry velocity. This results in a peak heating rate

$$14. \rightarrow \quad \dot{q} \approx 1.11 \times 10^{-4} V_0^3 \sqrt{\frac{\beta \sin\gamma}{3 r_{NOSE} \bar{z}}}$$

This is the method developed by Allan and Eggers and originally published in N.A.C.A Report 1381 [11]. The entry parameters in Table 2.04.01-01 correspond to the case where a vehicle in a 200 km circular orbit performs a 50 m/s deorbit burn, lowering its perigee to 33.7 km altitude. The given starting altitude of 100 km corresponds to the entry interface condition - above this altitude, the vehicle is assumed to be traveling in a vacuum.

Table 2.04.01-01: Representative entry simulation parameters

Scale height	$\bar{z}$ = 8000 m
Sea-level density	ρ_0 = 1.2250 kg/m^3
Entry altitude	z_E = 100 km
Entry velocity	V_E = 7854.4 m/s
Flight-path angle	γ = −0.7185°
Peak deceleration	**a** = 17.79 m/s
Nose radius	r_{NOSE} = 1 m

The next set of figures was generated by integration of the equation of motion from the starting conditions given in Table 2.04.01-01 to the end of hypersonic flight, arbitrarily taken to be Mach 5, or approximately 1700 m/s.

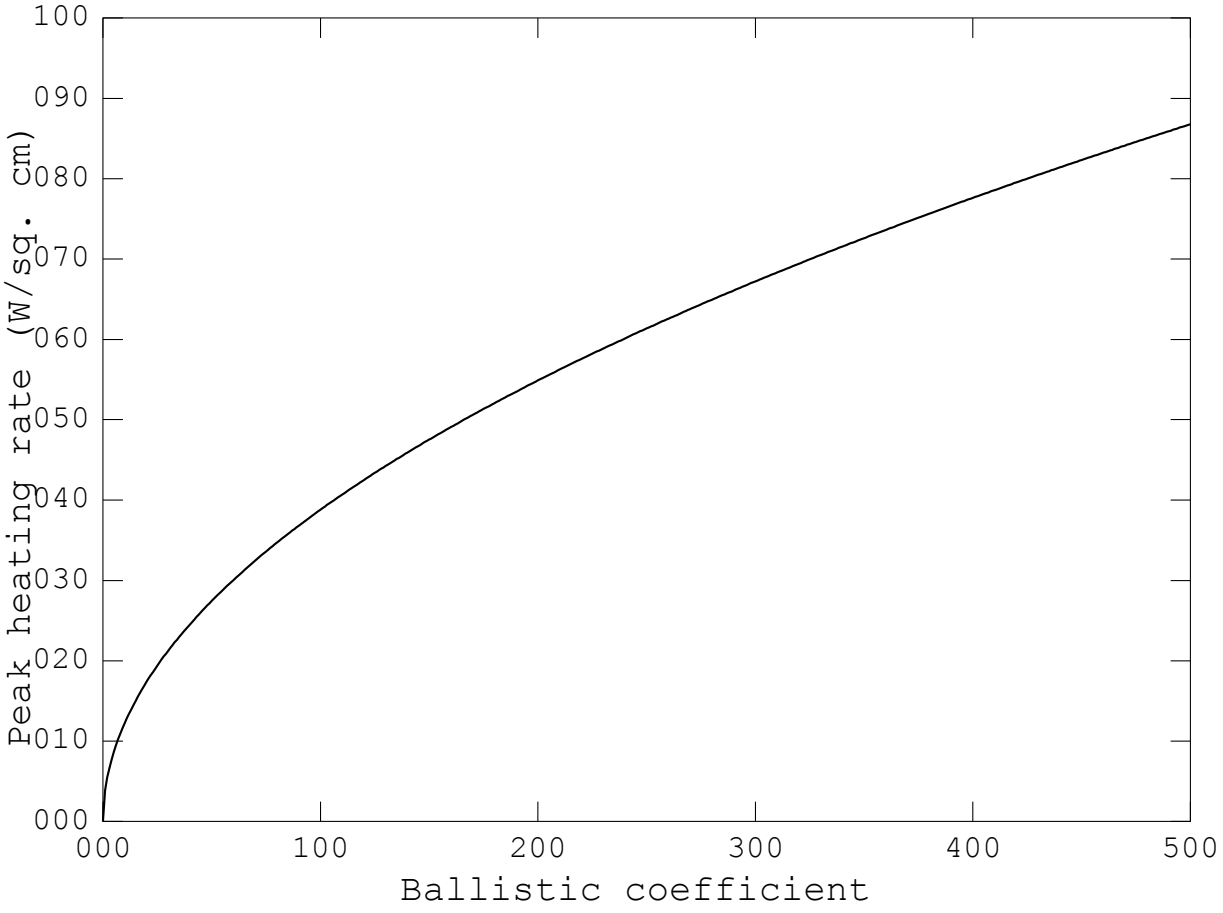

Figure 2.04.01-02: Peak heating rate vs. ballistic coefficient

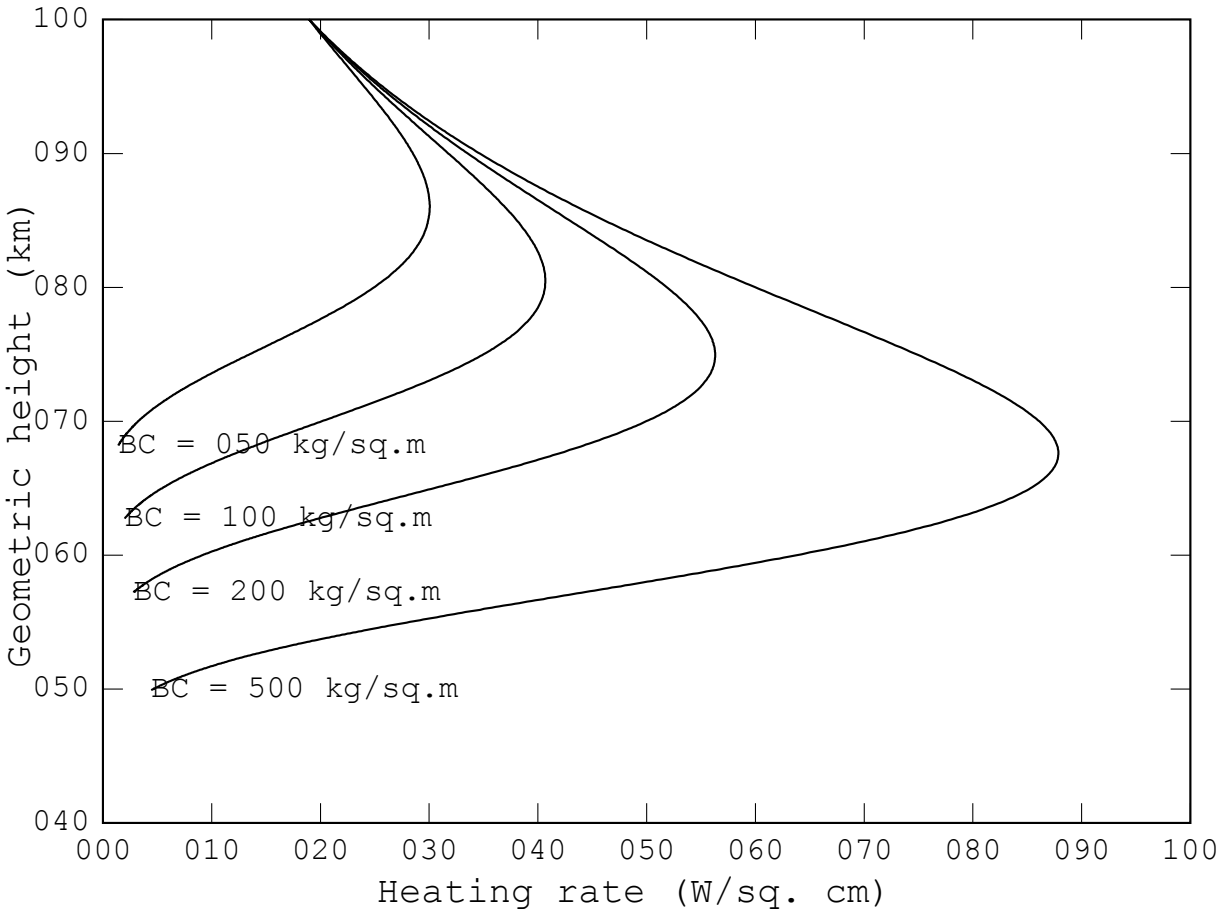

Figure 2.04.01-03: Time-varying heating rate

Note that in addition to reducing the peak heating rate, a lower ballistic coefficient also raises the altitude at which it occurs.

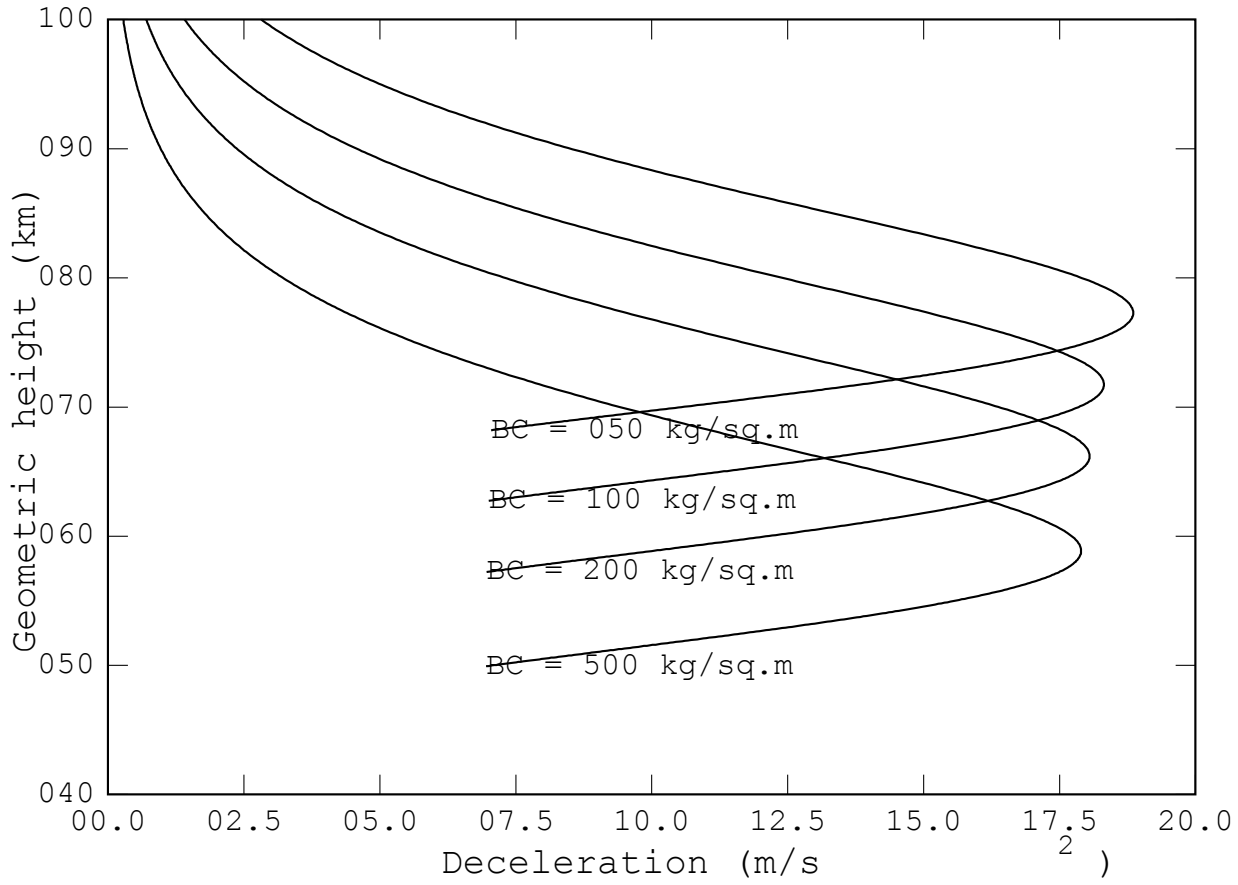

Figure 2.04.01-04: Time-varying deceleration and dynamic pressure

The peak deceleration is relatively insensitive to the ballistic coefficient.

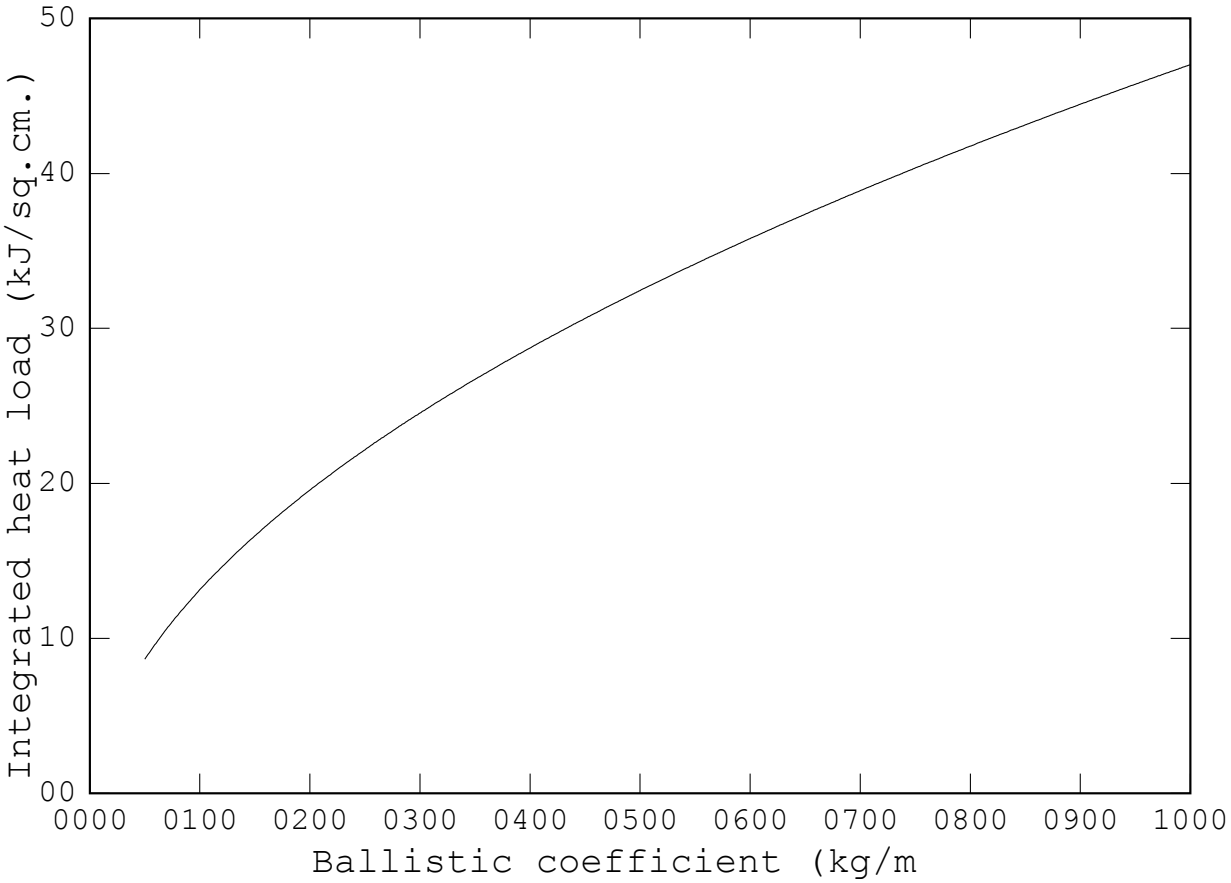

Figure 2.04.01-05: Integrated heat load vs. ballistic coefficient

With such a shallow flight-path angle, the neglection of gravity is not entirely valid, as in practice gravity will steepen the trajectory. Nevertheless, the preceding results are still indicative of the general trends.

Higher ballistic coefficient correspond to higher peak heating rates and integrated heat loads. It is evident that the vehicle should have the lowest possible ballistic coefficient in order to minimize the heating rate. A vehicle with a low ballistic coefficient will decelerate while still in the thin upper atmosphere, so that it will be traveling slowly once it has descended into the thicker lower atmosphere.

For reentry, the vehicle should be as draggy as possible - for the same reason a parachute should be as draggy as possible. However, this is exactly the opposite of what is desired during the ascent, during which drag losses must be minimized. The comparison to a parachute is deliberate - the vehicle can reconcile these disparate requirements by deploying a flexible structure to increase its area for reentry.

022

2.04.02: Hypersonic inflatable aerodynamic decelerators

The vehicle employs a hypersonic inflatable aerodynamic decelerator (HIAD) to perform a high-drag reentry. This device is normally kept undeployed in a compact, packed state.

The HIAD envelope, whose windward surface is covered in ablative material, is supported by an internal inflatable bladder. The bladder is composed of a series of toroids, which form a conical frustum. The bladder is pressurized with hot hydrogen from the onboard gas generators. Such stacked-toroid blunted cone (STBC) configurations [12] must be attached to the circumference of some sort of centerbody, from which they extend outward as they deploy.

The HIAD is attached to an extensible aft centerbody (XAC). This is located centrally on the base of the vehicle, inboard of the engines. The XAC is extended well clear of the main engines prior to entry interface to allow the HIAD to deploy cleanly. It includes a rigid, thermally-protected nosecap, since the HIAD only extends outward.

The XAC is attached to the base of the vehicle using screwjacks. These can provide the necessary stroke length at a low weight, and require no power to remain extended, even under load. For purposes of mass estimation, catalog data on a commercially-available line of heavy-duty screwjacks is used as a baseline [13]. However, the leadscrews in a screwjack - which react all loads from the HIAD/XAC into the vehicle during reentry - are long and thin, and therefore prone to crippling and buckling. The vehicle must therefore avoid excessive deceleration during reentry.

This provides for a low ballistic coefficient and protects the engines during reentry. Ballistic coefficients on the order of 100 kg/m^2 are practicably achievable, corresponding to peak heating rates on the order of 40 W/cm^2 and total heat loads of 15 kJ/cm^2.

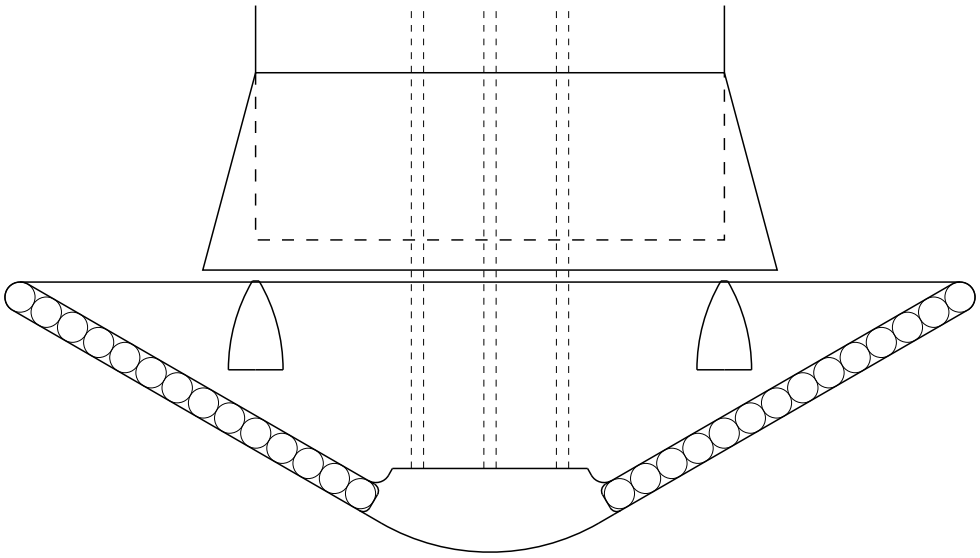

Figure 2.04.02-01: General configuration of HIAD/XAC

HIAD technology is being developed by NASA in support of interplanetary missions, where their capability to allow the vehicle to increase its drag without being constrained by the diameter of the payload fairing on the launch vehicle is useful [14]. There are plans to scale HADs to large diameters in order to land large payloads on Mars [15]. NASA is proceeding from successful sub-orbital flights to orbital reentry test flights.

After end-of-hypersonics, the HIAD is discarded at high altitude, to reduce wind dispersion. There does not appear to be any way to retract/repack it in flight, and it would be destroyed during the landing burn in any event.

Some development of flexible TPS technology is required for this application. It has been proposed to use a HIAD to land a large (80 MT) payload on the Martian surface. This application would entail two (aerocapture and entry) heating pulses [15]. Peak heating and total head load during aerocapture are estimated to be 110 W/cm^2 and 12.5 kJ/cm^2, in excess of what would be encountered here [15]. Candidate materials include phenolic-impregnated carbon felt (a flexible analogue to rigid PICA), a flexible version of SIRCA-15, and a silicone-impregnated silica felt blanket [15]. The envelope includes insulation (Pyrogel), a gas barrier (Kapton) and a mechanical load-carrying substrate (Kevlar). The pressurized bladder is composed of several layers of Kevlar cloth, with the innermost layer coated with silicone for gas-tightness. Both the envelope and bladder are composed of numerous joined radial segments [16].

Mass input properties are provided in Appendix B.

2.04.03: Prediction of HIAD aerodynamic characteristics

To determine the vehicle's re-entry footprint/cross-range capability, it is necessary to simulate the reentry flight phase. This requires the prediction of the aerodynamic characteristics of a sphere-cone configuration [17]. The pressure distribution on the surface of an object in hypersonic flow can be accurately predicted using the Newtonian impact theory. The incident flow impinges upon a flat surface with some area A inclined to it at an angle θ.

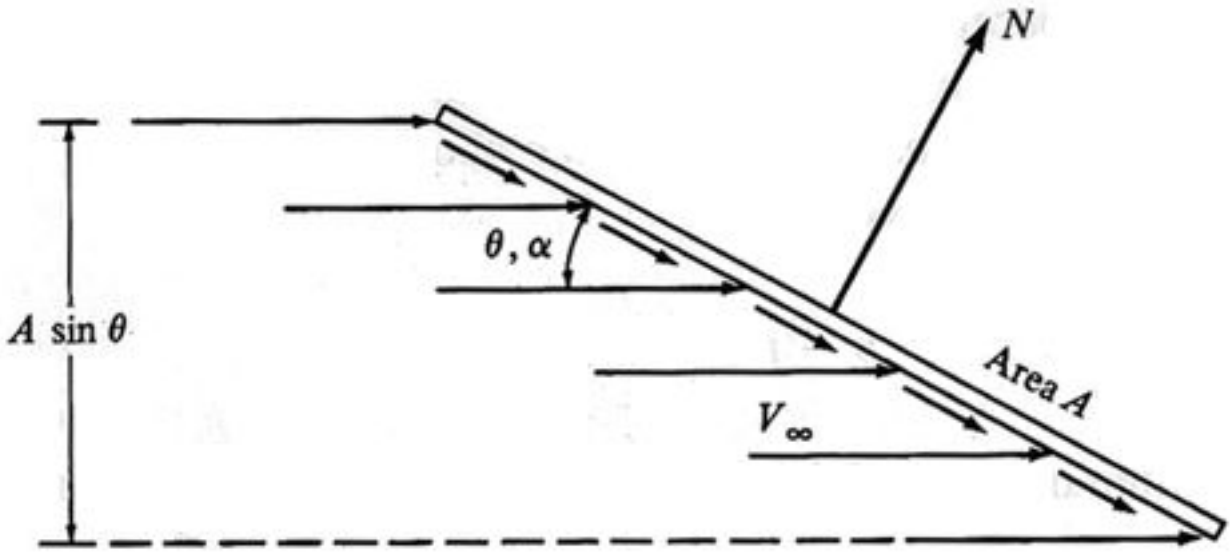

Figure 2.04.03-01: Micromechanics of Newtonian flow [18]

The component of the momentum of the flow normal to the surface is nullified, while the tangential component is preserved. The pressure coefficient across the surface is given by

$$15. \rightarrow \quad C_P = 2\sin^2\theta$$

The general definition of the pressure coefficient is

$$16. \rightarrow \quad C_P = \frac{P - P_\infty}{0.5\rho_\infty V_\infty^2}$$

where P is the local static pressure, P_∞ is the free-stream static pressure, V_∞ is the free-stream velocity and ρ_∞ is the free-stream density . Only the windward surface experiences any aerodynamic pressure. The leeward surface is shadowed and does not contribute to the aerodynamics.

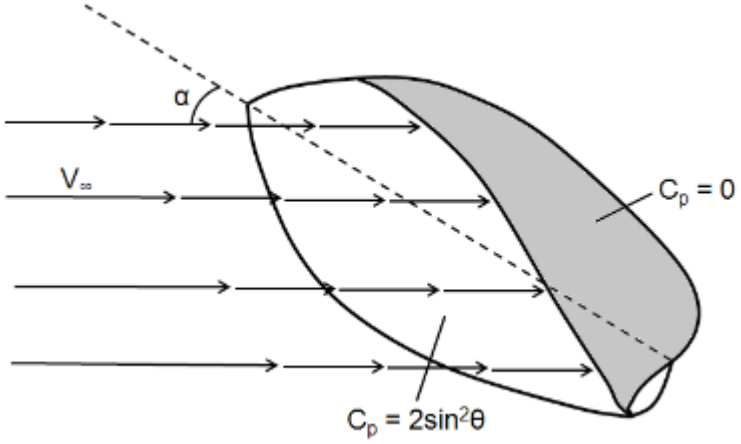

Figure 2.04.03-02: Flow shadowing [17]

The aerodynamic characteristics are estimated by modeling the windward surface as a collection of facets, over each of which the pressure is constant. The vector sum of the net resultant forces is resolved into lift and drag components. This method is implemented as an ad-hoc MATLAB code.

The code, given an input geometry and the angle of attack, determines:

1. Lift and drag forces acting on the forebody
2. Lift and drag coefficients, normalized with respect to the maximum projected area
3. Location of the aerodynamic center

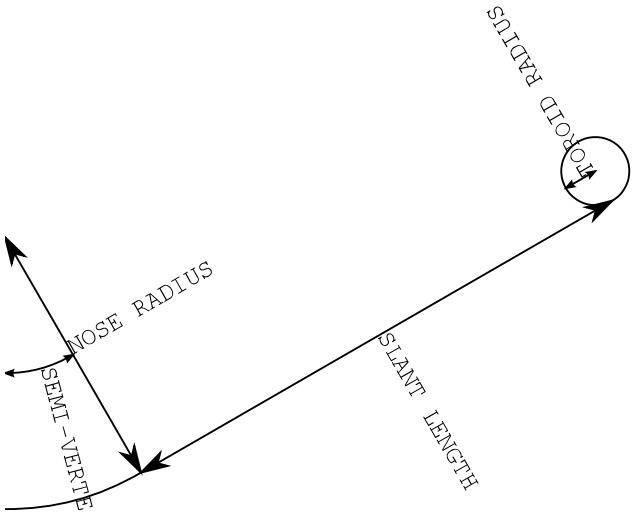

Figure 2.04.03-03: Illustration of forebody geometry [PLACEHOLDER]

The preceding figure illustrates the parameters used to describe the geometry of the forebody and the coordinate system used.

Some consideration, if only at a conceptual level, must be made of the wake flow, especially as it pertains to leeward heating. For an actual blunt-body configuration, especially one inclined to the flow, the total flowfield is quite complicated. It suffices to say that the flow will expand aft of the shoulder of the forebody.

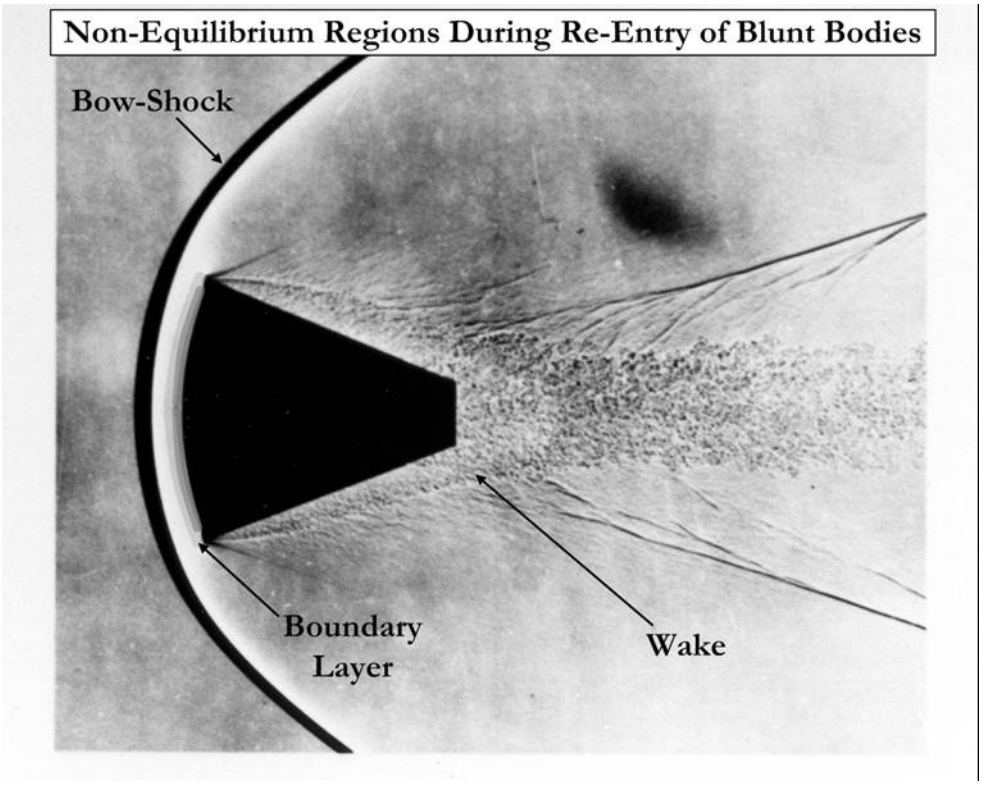

Figure 2.04.03-04: Real blunt-body flow [19]

Here, it will be assumed that the flow merely undergoes Prandtl-Meyer expansion around the shoulder, separating from the surface once it has turned through the maximum angle and continuing at this angle. This flow must not impinge on the airframe.

This is one of the criteria that limits the maximum angle of attack at which the configuration can operate. Another is the semi-vertex angle. The smaller the semi-vertex angle, the larger the arc the spherical portion of the forebody subtends. The stagnation point must remain on this spherical segment. A sharper cone is less limited by this criterion.

Comparison with an analogous case - the convective and radiative heating-rate distributions experienced on the surface of the Apollo CM during Apollo 4 - indicate that, provided that there is no wake flow impingement, the leeward heating environment will be gentle. For instance, according to Table I of NASA TN D-5969 [20], at one representative location on the windward meridian of the aft cone, the convective heating rate - at that location, there was no significant radiative heating - was only 5.6% of the peak zero-angle-of-attack stagnation heating rate on the leeward surface. The maximum temperature recorded by a thermocouple at a 0.20-in depth was only approximately 500°F .

The diameter of the HIAD is much larger than the maximum body diameter, so that the airframe is set well back from the shoulder. The entry velocities and ballistic coefficient are also much lower than for an Apollo CM returning from a lunar mission.

Mass allowances are made for ascent TPS, which doubles as external insulation for the ascent propellant tanks. It is assumed that they provide adequate protection. This TPS, which is essentially aerogel (Pyrogel or similar) insulation, is in the form of numerous modules glued to the airframe, possibly with strain-compatibility provisions included, for easy replacement.

2.04.04: Hypersonic glide flight phase

The vehicle generates lift during the hypersonic glide phase of reentry, both in order to decrease its rate of descent and to perform cross-range maneuvers. Since the forebody is axisymmetric, the vehicle must be inclined to the flow to generate lift.

This is accomplished by mounting the XAC at a small angle, so the forebody is slightly skewed. The precise angle is chosen so that at some small angle of attack, the center of mass of the vehicle falls along the aerodynamic line of action. The vehicle will trim to whatever angle of attack this corresponds to. Steering is accomplished by using the RCS to bank the vehicle.

This angle is fixed, since the provisions required to allow it to be changed in flight would be far too heavy and complicated. However, as the XAC is already designed to extend and retract, some variation in the location of the CM can be compensated for by the existing provisions.

For the entry simulation, the vehicle is simulated as a point mass, and maintains a constant angle of inclination to the flow, so that the vehicle flies at a constant L/D ratio.

At 2000 m/s, the vehicle banks so that its lift vector is pointing straight downward, so as to "pickle" itself onto the landing site. The HIAD is impulsively discarded at 1700 m/s.

The dynamics of HIAD jettison require further investigation. On a purely conceptual level, It is assumed that the RCS can fire to nullify any stray angular velocity components. The jettison provisions will have to ensure that the event is symmetric, to minimize the perturbation, and that the remains of HIAD are discarded cleanly, without fouling on the vehicle, which would cause asymmetric aerodynamic loads and possibly uncontrollable tumbling and consequent loss of the vehicle.

The vehicle initially maintains a zero bank angle in order to reduce its rate of descent. After it has passed the point of maximum acceleration, it steps to and maintains a constant bank angle. The cross-range capability is determined by sweeping through a range of such bank angles.

Table 2.04.04-01: Forebody geometry

Nose radius R_N	1.00
Frustum slant length L_S	2.00
Toroid diameter $2R_T$	0.05
Semi-vertex angle θ_N	60°

In the preceding table, the geometric parameters are normalized with respect to the nose radius. The entry parameters are as per Table 2.04.01-01.

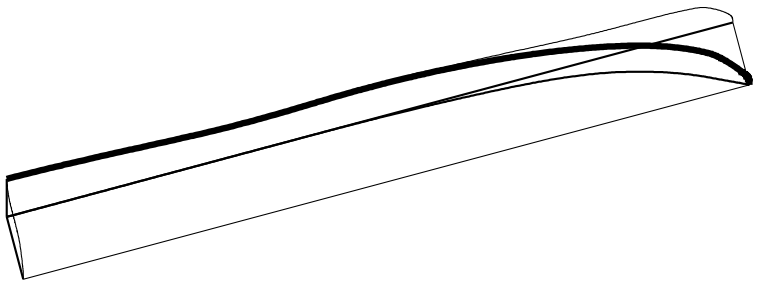

Figure 2.04.04-01: Isometric view of representative trajectory

The preceding figure is an isometric view of a typical return trajectory. The vehicle maintains a 30° angle of inclination and is banked at 60°. It maneuvered to 196 km transverse to the ground track. The maximum deceleration was 37.3 m/s^2. Peak heating and the total heat load were 48.5 W/cm^2 and 7.8 kJ/cm^2, respectively.

Entry flight is simulated using an ad-hoc MATLAB code numerically integrating the equations of motion according to a method derived from one detailed in reference [21].

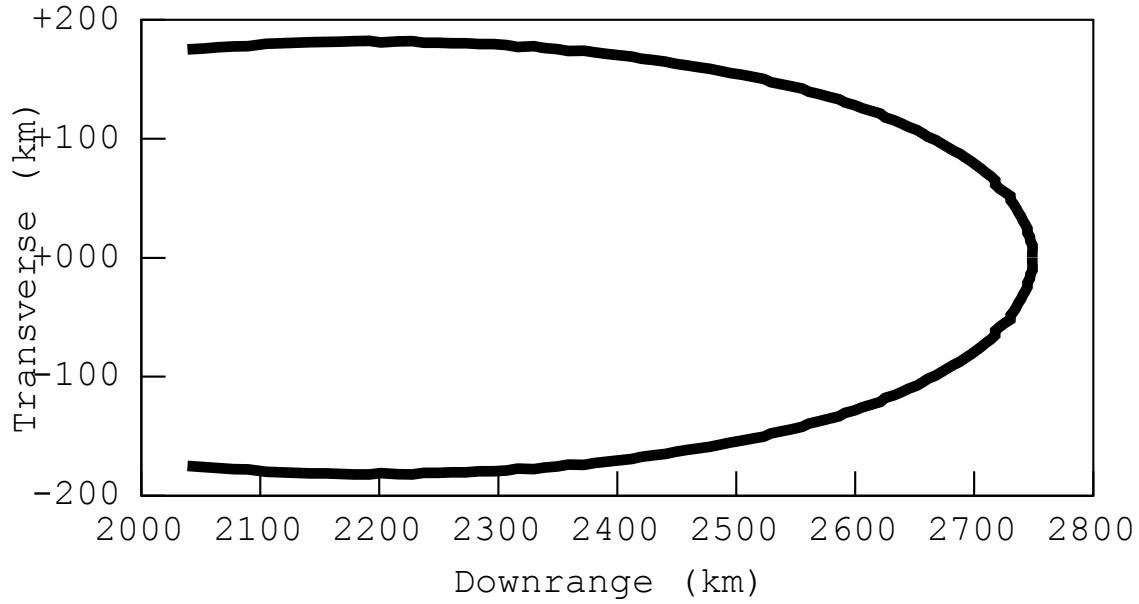

Figure 2.04.04-02: Entry footprint

The preceding figure was generated by varying the bank angle from 0° to 60°, with a 40 m/s^2 deceleration constraint. The angle of inclination is 30°. Based on these results, the vehicle can maneuver up to almost 200 km to either side of the ground track. It can therefore be conservatively stated to have about ±150 km of cross-range - modest, but sufficient for this application.

2.04.05: Terminal flight phase

The vehicle must be able to reliably target a landing pad of reasonable size. The main source of dispersion will be due to winds aloft encountered during terminal flight. For terminal maneuvering, the vehicle deploys a steerable parafoil.

The vehicle can compensate for a 3000 m lateral positioning error at 7000 m altitude against a 15 m/s wind. Descent time will be about 100 seconds. This implies that the vehicle should be able to maintain a glide ratio $\Lambda = 0.65$, assuming that it can maneuver for the entirety of descent. This corresponds to a canopy loading of about $60\ kg/m^2$ [22].

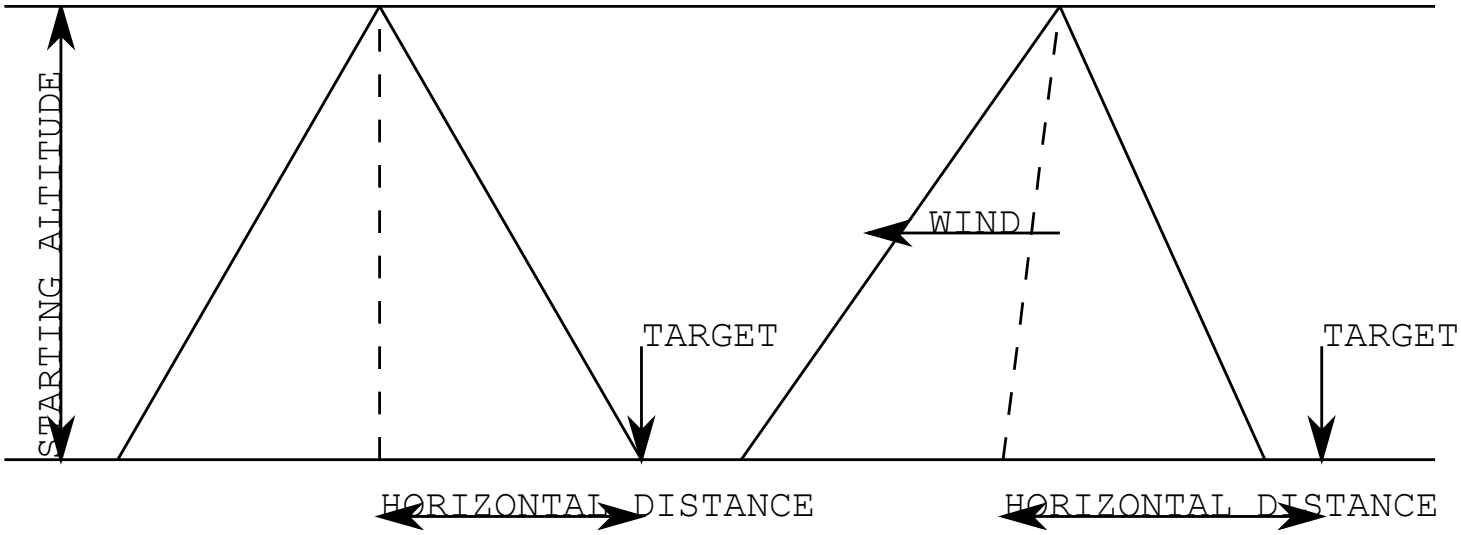

Figure 2.04.05-01: Illustration of parachute descent

Existing maneuvering parachute systems have about 5% the mass of the maximum payload at canopy loadings around 15 kg/m^2 [23][24]. Their mass is assumed to scale with the canopy area. It follows that the mass of the necessary parafoil system can be estimated at about 2.5% the mass of the payload - the empty vehicle with landing propellants.

2.05: Materials, structures and manufacturing

2.05.01: Material - IM-reinforced BMI laminates

To reduce mass, the vehicle structure is composed of intermediate-modulus (IM) carbon fiber/bismaleimide resin (BMI) laminates. This provides mechanical properties similar to aluminum alloys, but at a lower density. Bismaleimide resins have the advantage of higher service temperatures - up to around 200°C - than epoxies [25].

Design properties are provided in Appendix B.

2.05.02: Composite cryotanks

The ascent propellant tanks will account for most of the structural mass of the vehicle. All main engines considered consume liquid oxygen, and all but one use either liquid hydrogen, liquid methane, or both.

It is challenging to use CFRP (carbon fiber reinforced plastic) laminates to contain cryogenic propellants. Carbon fiber has a small negative coefficient of thermal expansion, while the resin matrix has a large positive coefficient of thermal expansion [26].

When the laminate is thermally cycled, strain incompatibility between the phases of the laminate results in microcracking, which is exacerbated by cryogenic embrittlement of the matrix. Cryogens can seep through these microcracks [26]. Leaking cryogens are a major fire hazard, can produce cryopumping/icing on the external surfaces of the tank, and can accumulate somewhere only to boil off later [26]. The tank structure is also subjected to other forms of damage - bird/lightning strikes, various forms of impact damage, etc. [26]

It is preferable to externally insulate the tanks, with the laminates directly wetted by cryogens. Cryogenic propellant tanks require insulation in any event, to minimize boiloff and prevent the formation of frost or liquid air on their exterior surfaces. External insulation can also function as thermal protection, saving mass.

One approach is to include a barrier feature in the laminate, which retains its impermeability even in the event of damage to the matrix. This may be a special thin coating on the surface of the laminate, or a film/membrane buried within it [26][27]. Another is to fabricate the inner layers (those wetted by cryogens) using thin plies, resulting in a denser, more permeation-resistant laminate [28]. In addition, the matrix material can be toughened by various techniques [27].

2.05.03: Material processing and manufacturing

All laminates are laid up from prepreg, primarily using either ATL (automatic tape laying) or AFP (advanced fiber placement) processes, in which a multi-axis industrial robot places strips of prepreg on the tool surface [29]. ATL is suitable only for simpler surface geometries, but is faster. State-of-the-art deposition rates are about 20 kg/hr and 5 kg/hr, respectively [30].

The prepreg is laid up onto a breakdown tool, which is a type of mandrel that can be disassembled and extracted from inside the cured part through a hole [31]. As part of NASA's Composite Cryogenic Technology Demonstration project, several Boeing/Janicki-produced test articles, fabricated using such tooling, have been successfully tested [31][32][33].

After layup, laminates are debulked to eliminate void content. High-performance laminates are debulked/cured at elevated pressure in an autoclave. However, the large size of the major structural components of the vehicle - which should be fabricated in one piece for best results - precludes autoclave processing. The propellant tanks may be up to 20 meters in diameter, over twice as much as the biggest autoclaves today [34].

In addition, these parts may require thousands of hours for layup, during which time the prepreg will lose tack and drape and spontaneously cure. It is therefore necessary to improve the out-of-autoclave and out-life characteristics of BMI prepregs, and to increase deposition rates.

With an OOA (out-of-autoclave) material system, the part would be vacuum-bagged and cured at ambient pressure in a large oven. As will be detailed shortly, the vehicle's ascent propellants are stored in a common-bulkhead integral tank pair. A special type of breakdown tool is used. This tool has two major components - one with a convex capsule-shaped tool surface, and another generally similar one with an inverted concave end, to conform to the curvature of the common bulkhead. Material to comprise the aft and common bulkhead as well as part of the thickness of the fuel compartment barrel is laid up on the convex tool portion, before the concave tool is moved into position and the remainder of the fuel container barrel, the oxidizer container barrel, and the forward bulkhead are laid up. With layup complete, the part is cured, and the tools disassembled and extracted.

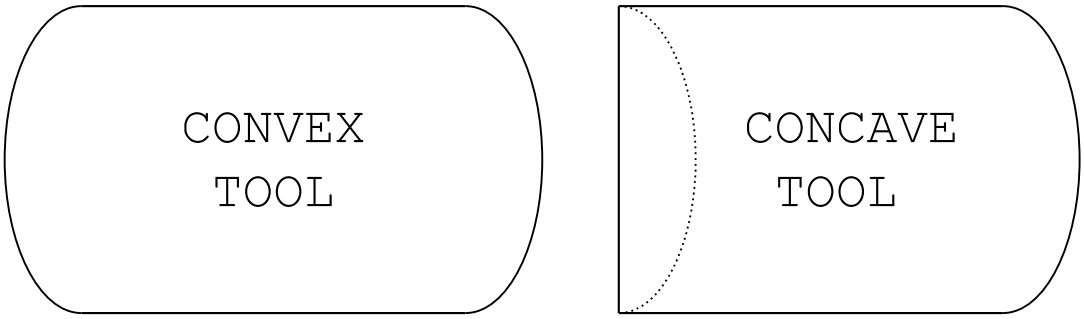

Figure 2.05.03-01: Conceptual design of tooling

One possible fabrication process is in-situ fiber placement. Fully-impregnated prepreg is heated with hot nitrogen gas and compacted with a roller as it is laid up. This process can accommodate complex surface geometries and achieve good laminate consolidation without autoclave curing. It has been demonstrated with BMI prepregs and identified as a candidate process for fabricating composite cryotanks [28].

There is wide general interest in OOA processing, including for BMI prepregs, due to the potential for major cost savings, as well as for composite launch vehicle structures [35]. In that application, limited material out-life has been recognized as a challenge [36]. These technologies are active research areas. The necessary improvements in basic technology represent plausible developments.

2.06: Concept description

2.06.01: Vehicle configuration

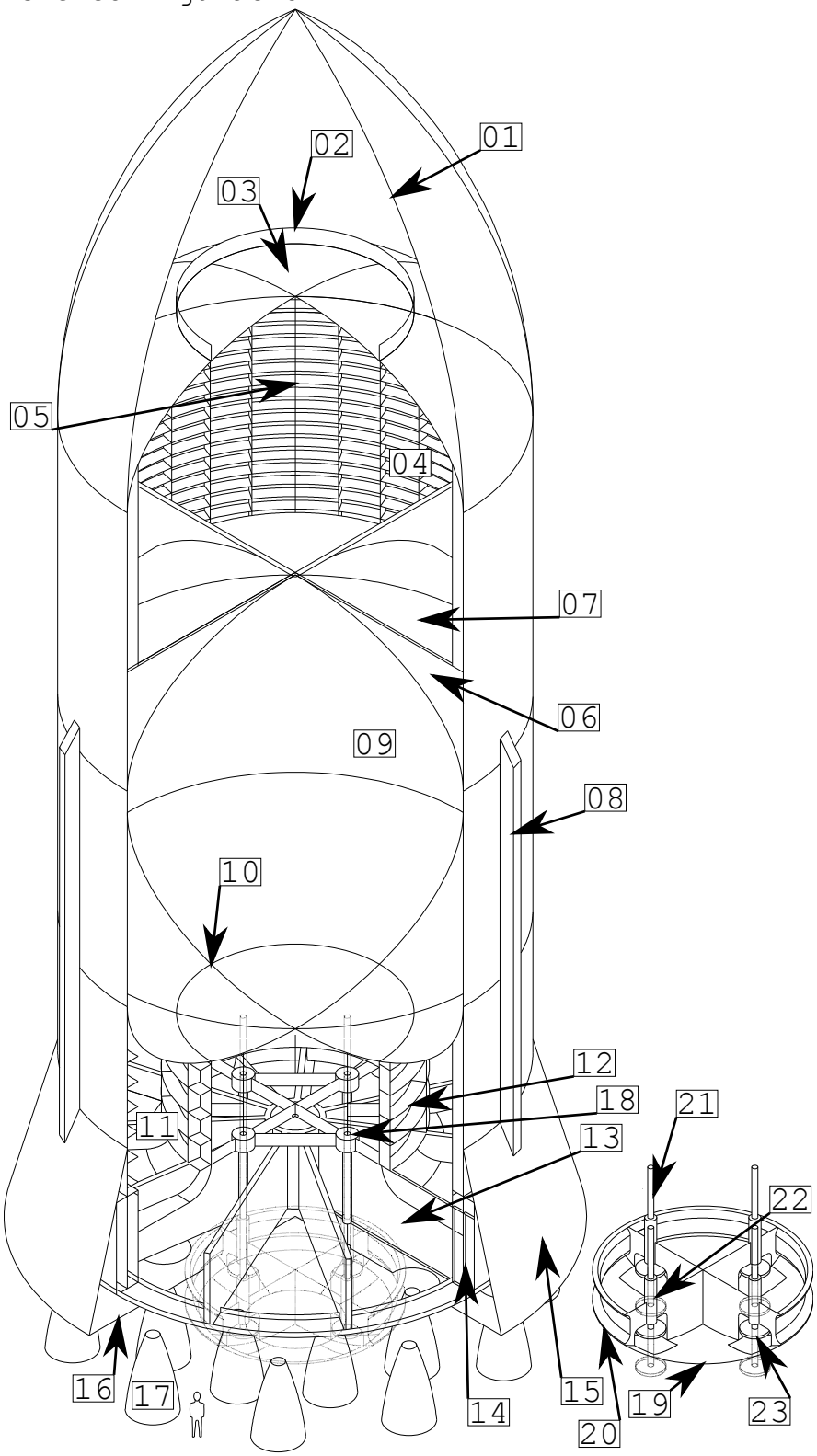

Figure 2.06.01-01: Diagram of concept vehicle

The legend for the preceding figure follows. Note that some details have been omitted for clarity. The diagram is an embedded .svg file - readers of the electronic version may zoom in without any loss of quality.

01: Forward shroud
02: Payload interface ring
03: ITS bulkhead (forward)
04: ITS oxidizer (LO2) container
05: Oxidizer container anti-slosh baffles
06: Oxidizer container anti-vortex baffles
07: ITS bulkhead (common)
08: Oxidizer line tunnels
09: ITS fuel (LH2) container
10: ITS bulkhead (aft)
11: Secondary fuel (RP-1/LCH4) container
12: Secondary fuel container anti-slosh baffles
13: Thrust structure beams
14: Thrust structure barrel
15: Aft fairing
16: Base heatshield
17: Ascent engines
18: Screwjack gearboxes
19: XAC rigid nosecap
20: HIAD attach rings
21: Screwjacks
22: Landing leg hydraulic cylinders
23: Landing legs

Notably, the secondary LO2 and LH2 tankage, the RCS and OMS engines, and most of the propellant feed lines, have been omitted. Although the secondary fuel container (11) is depicted as annular, its actual design is purely conceptual at this stage.

In addition, the components of the HIAD (the envelope and bladder) have been omitted for clarity.

Note the human figure among the main engines for scale. This will be a very large vehicle.

The ascent and OMS engines are arranged in one or more concentric rings on the base of the vehicle around the XAC. They are spaced to permit the main engines to deflect to the limits of their 7° half-angle gimbal pattern without colliding with each other. The vehicle has 12 RCS thrusters arranged to provide full three-axis rotational control. A conical base fairing and base heatshield protect the main engines from aerodynamic loads and the heat of their exhaust plumes. The trailing edge of the base fairing is aft of the gimbal plane, to permit the main engines to fit inside. They penetrate circular apertures in the base heatshield. Flexible curtains seal the gaps between the main engines and the aperture edges.

The thrust structure notionally consists of a number of thrust posts, a cylindrical reinforced barrel section, which supports the outboard engines, and a number of crossbeams, which support the XAC and any inboard engines. The thrust structure barrel section is contiguous with the integral tank system, with which it has a common diameter. Various items of equipment (electrical and hydralic power supplies, avionics, etc.) are packaged inside the thrust structure, mounted between the crossbeams. This is similar to the arrangement employed on the Boeing S-IC [37].

Ascent propellants are stored in the integral tank system, which includes of pressure-stabilized ("balloon") fuel and oxidizer containers, separated by a common bulkhead. On the ground, the tanks can be mechanically tensioned/externally supported. They are pressurized either by externally-supplied helium, or autogenously by hot propellant gases produced by either the main engines or the gas generators.

The oxidizer is stored forward to provide the engines with a longer moment arm and improve control authority on ascent. The tank walls consist of cylindrical barrel sections for both compartments and hemi-ellipsoidal aft, forward and common bulkheads. All bulkheads have a 2:1 aspect ratio. The common bulkhead is oriented convex-forward, since the pressure in the fuel container will be higher than in the oxidizer container. It also places the aftmost point of the integral oxidizer container close to the outer mold surface, allowing it to be drained by lines running around the outside of the integral fuel container.

Propellants for other maneuvers are stored in non-integral tanks. The tanks containing oxidizer for the OMS, RCS and landing burns are mounted to the inner wall of the ITS oxidizer compartment. Those containing fuel for the OMS, RCS and possibly the landing burns are mounted inside the ITS fuel compartment.

For mixed/tripropellant-propulsion designs, the secondary fuel tanks (which contain the hydrocarbon fuel used) are mounted aft of the rear bulkhead. The RCS accumulators are mounted inside their respective ITS containers. All propellant tanks are configured for single-point filling.

The payload attachment system is directly attached to the forward ITS bulkhead. A tangent ogival shroud protects the payload and reduces drag on ascent. It is jettisoned during ascent. The cost is reduced by mass production. Jettisoning the shroud prevents entry wake flow impingement by shortening the vehicle. The recovery parafoil system is also located forward - the canopy/canopies are packed in containers mounted on the forward bulkhead, to which the risers attach. The bulkhead is reinforced to support these loads. For thermal protection and to insulate the propellant tanks, the outer surfaces of the vehicle, including the forward bulkhead, and the common bulkhead (to prevent one propellant boiling another) are covered in aerogel insulation.

The aforementioned XAC is attached to the vehicle by numerous screwjack extenders. The leadscrews are rigidly fixed to the XAC, while the gearboxes are attached to the thrust structure. As their stroke is quite long, they penetrate apertures in the aft ITS bulkhead and extend into "sheaths" inside the ITS fuel container. Actuation is hydraulic. The XAC itself is cylindrical, with a rigid sphere-cone nosecap. The landing gear consists of a several of short, hydraulically-extended pad-type landing legs. On landing, they extend through apertures in the nosecap, breaking through the flexible TPS (which also covers the rest of the nosecap surface) stretched across them. They may require cutters. The leadscrews are notionally attached to the breeches of the landing gear hydraulic cylinders.

The HIAD is packed atop and around the XAC. Its envelope is contiguous with the TPS on the rigid nosecap. The deployed envelope is supported by an internal pressurized bladder, which consists of a series of concentric toroids forming a conical frustum. It attaches to the XAC, by a series of clevis joints, directly to a forward circumferential attachment ring, and by straps running around the exposed leeward surface of the bladder to an aft one.

The screwjacks support all XAC loads - primarily for reentry and landing. They extend the XAC clear of the main engines, allowing the HIAD to be deployed cleanly. After HIAD deployment, the XAC retracts, to protect it during the landing burn. Since it is the closest part of the vehicle to the ground, it is the logical place to put the landing legs. This provides sufficient ground clearance for the main engines at a reduced penalty, albeit at the expense of a narrow stance.

2.06.02: Ground handling

Handling on the ground is by paired heavy long-wheelbase trucks equipped with robotic arms. These are similar to, but larger than, some existing designs, such as the MZKT-79221, which is a Soviet/Russian mobile ICBM transporter. These pick the vehicle up by its hold-down points. The vehicle is moved only when empty of propellants. Due to its high center of mass and the narrow stance of its landing gear, the vehicle is picked up by the ground handling trucks immediately after landing. The vehicle is serviced on the pad underneath a mobile shelter, which is moved aside prior to liftoff.

Figure 2.06.02-01: MZKT-79221 mobile ICBM carrier [38]

Figure 2.06.02-02: MV Mighty Servant 2 carries the damaged Samuel B. Roberts [39]

For long-distance surface transport, the vehicle can be carried on the deck of a heavy-lift ship. Semi-submersible heavy lift ships are routinely used to transport much larger and heavier payloads. For example, in 1988 the USS Samuel B. Roberts (FFG-58) was returned to the US for repairs aboard the *MV Mighty Servant 2* after it struck an Iranian mine in the Persian Gulf . The vehicle can be transported overland using heavy-haulage techniques. The vehicle, less engines and payload fairing, is transported within a protective shelter on the deck.

If both the origin and destination are spaceports, the vehicle can also ferry itself by ascending from one site but landing at another.

2.07: Historical VTVL projects

2.07.01: HATV/WCSS single-stage

In 1946, Martin and North American Aviation prepared proposals for a "single-stage satellite" under a USN program called HATV, for High-Altitude Test Vehicle. [40][41] The motivation was that in 1946, no one had built or flown any multi-stage rockets. They were not intended to be reusable and included no provisions for recovery.

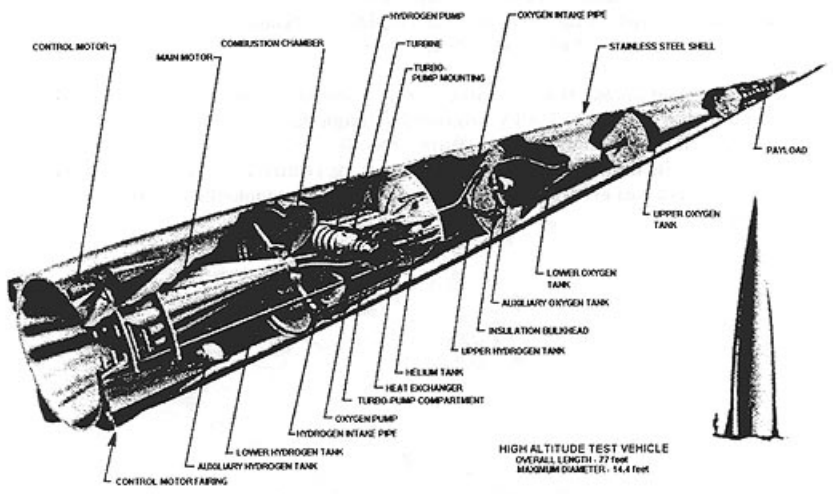

Figure 2.07.01-01: Martin HATV [41]

Note that, as late as the mid-1950s, almost a decade later, both the R-7 Semyorka and the Atlas employed a parallel staging scheme, in order to avoid the uncertainty that then surrounded starting a large liquid-fueled rocket engine at altitude.

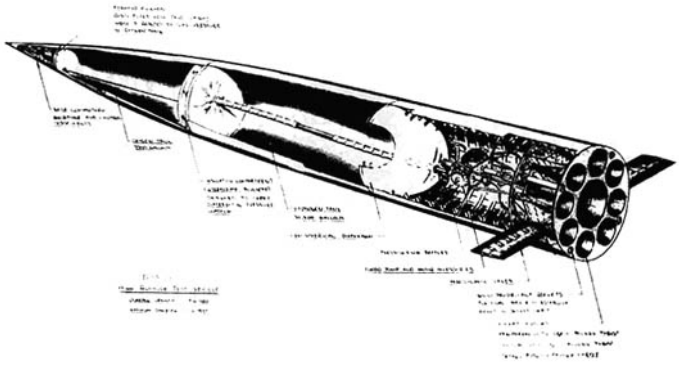

Figure 2.07.01-02: NAA HATV [41]

In response, the USAAF commissioned the famous "World-Circling Space Ship" study from Project RAND, then part of Douglas [40][41]. The baseline version of the WCSS was a four-stage vehicle, but a single-stage version was also considered. Like the Martin and NAA proposals, it was expendable [40][41]. Sources vary with respect to whether Douglas submitted an SSTO proposal as part of the HATV tender process or if their concept was developed later under the WCSS proposal [40] [42].

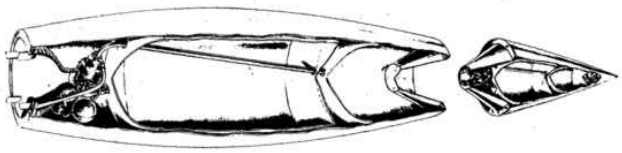

Figure 2.07.01-03: Douglas WCSS (single-stage version) [41]

The designers proposed many innovative features. All vehicles were to include lightweight pressure-stabilized tankage [42][43][44].

The NAA HATV may be particularly noteworthy - it was powered by a central sustainer engine surrounded by eight lower-expansion engines, all hydrolox. The booster engines were intended to operate at low altitude to provide additional thrust early in the ascent before being shut down [44]. They may have operated at a higher O/F ratio than the sustainer in order to increase the bulk density, although the resulting elevated combustion temperatures would have strained the metallurgy of the era.

2.07.02: Phillip Bono

Phillip Bono, a Douglas Aircraft Company engineer, is considered to be the father of the VTVL SSTO [45]. Beginning with the ROOST (Recoverable One-Stage Orbital Space Truck), a vehicle which was intended to land on the water surface and apparently even used an inflatable "drag cone" (to be pressurized by hydrogen gas) for recovery, he prepared a series of design studies for various VTVL SSTOs [46]. These included the ROMBUS, Deimos, Hyperion, and several others. All had the same fundamental CONOPS - a vertical powered take-off, non-lifting ascent, base-first reentry, and a vertical powered landing. Later proposals used a plug-nozzle, a type of aerospike engine, instead of a number of discrete bell-nozzle engines [46].

One of his designs, the SASSTO (Saturn Application Single-Stage-to-Orbit) is a good example of a classical VTVL SSTO. Though nominally derived from the Douglas S-IVB, it ultimately ended up having little in common with the baseline. The SASSTO was powered by a hydrolox aerospike engine, with the nozzle doubling as an actively-cooled heatshield for reentry. It used partially-frozen "slush" hydrogen to increase bulk density. [47]

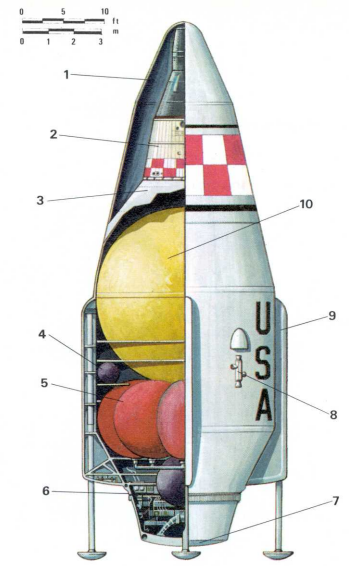

Saturn Application Single-Stage-To-Orbit (SASSTO). *Key:* 1. Optional fairing around two-man Gemini capsule; 2. Gemini adapter section; 3. Transition support structure; 4. Orbit injection/retro- and attitude-control propellant tanks *(6)*; 5. Toroidal liquid-oxygen tank; 6. Annular combustion chamber; 7. Truncated plug nozzle and re-entry heat shield; 8. Attitude-control system *(4)*; 9. Retractable landing legs *(4)*; 10. Spherical liquid-hydrogen propellant tank.

Figure 2.07.02-01: Douglas SASSTO [48]

These design features reflect two persistent motifs: having a single piece of hardware/vehicle structure perform multiple duties, and increasing the bulk density, both in order to achieve a mass savings. As with many other proposals, protecting the vehicle base area, where the engines are located, was identified as a challenge.

2.07.03: Chrysler SERV

In the 1970s, NASA evaluated several different proposals for what would become the STS, including the Chrysler SERV (Single-stage Earth-orbital Reusable Vehicle), a VTVL SSTO. Of the various proposals, it was the only SSTO and the only one intended to normally fly unmanned [46].

The vehicle was powered by a hydrolox aerospike engine, composed of numerous modules arranged around the base circumference. These were considered to be technically risky. In addition to these, the vehicle included a number of jet engines for landing, since NASA required that the vehicle be able to compensate for large descent positioning errors [46].

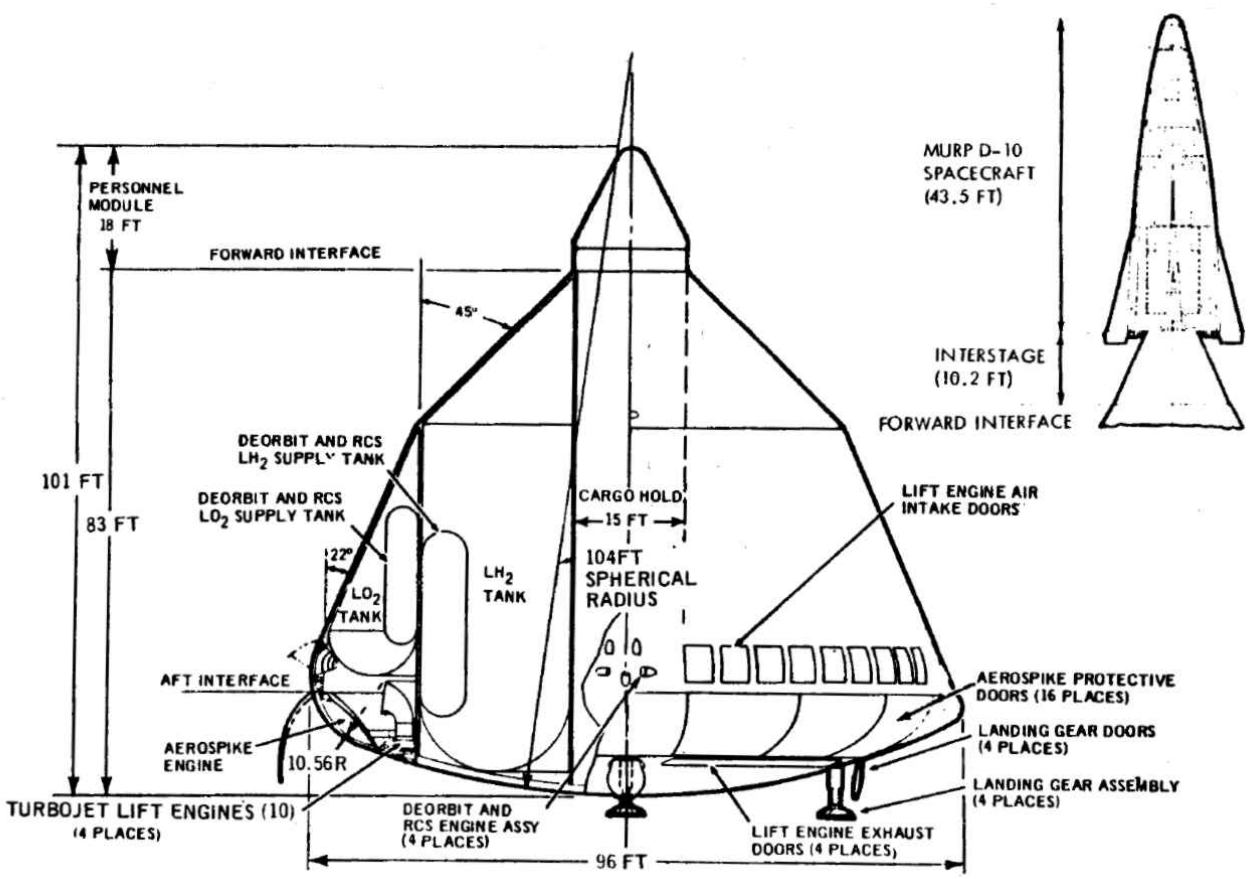

Figure 2.07.03-01: Chrysler SERV [49]

It was intended to perform a base-first reentry, during which the main engines were protected by hatches. Thanks to its large diameter, it would have experienced gentle heating on reentry.

Unfortunately, although the work done was very thorough and credible, the SERV proposal was politically incorrect. NASA favored various types of lifting (i.e. winged or lifting-body) vehicles, and the fact that the SERV was only optionally manned did not endear it to the astronaut corps. [49]

2.07.04: Robert Salkeld/MAKS

In the 1970s, Robert Salkeld, an engineer at the System Development Corporation, was the first to propose the use of multiple (both hydrocarbon and hydrogen) fuels on a single SSTO, in order to obtain some of the benefits of both. He considered the use of both separate hydrogen and hydrocarbon-burning engines, but identified true tripropellant engines as better performers [46].

Later, in the 1980s, the Soviets developed a design for a small air-launched spaceplane known as the MAKS, which was quite similar to some of Salkeld's early proposals for small air-launched spaceplanes. The MAKS was to have been carried aloft by a modified Antonov An-225 Mriya. The baseline design was not quite an SSTO, since it carried its propellants in an external tank, which was jettisoned to impact in a remote ocean area downrange. A fully-reusable/unitary derivative, the MAKS-M, was planned as a follow-on [50].

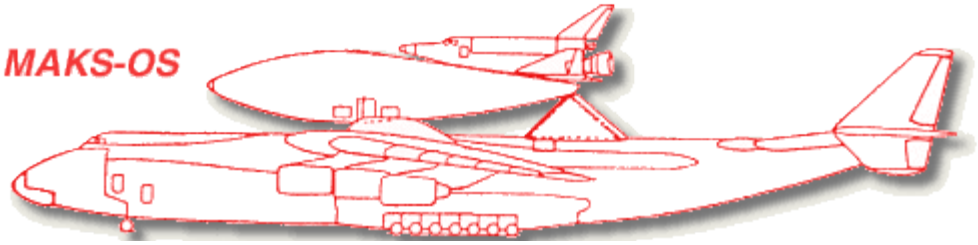

Figure 2.07.04-01: MAKS-OS with drop tank and An-225 carrier [51]

The MAKS is noteworthy as the application for which the RD-701 was developed. This was a tripropellant hydrokerolox engine. As intended for installation on the MAKS, it included two separate combustion chambers and nozzles, which were fed by a common set of pumps. The RD-704 is the single-chamber version of this engine [52].

Although the project ended with the collapse of the Soviet Union and no full-up hardware was built, a sub-scale demonstrator was built and operated, validating the basic principles over the course of 50 test-firings [50]. The engine had reached an advanced stage of design - 80% of the drawings had been completed [53].

2.07.05: Boeing Leo

In the 1970s, NASA studied the construction of a "Satellite Power System" to meet the future energy needs of the US with space solar power. Many RLV proposals were considered to meet the enormous space transportation requirements of this project, including at least one VTVL - the Boeing LEO, or as it was nicknamed, the "Big Onion." (The origin of this nickname is obscure.) This vehicle was powered by 24 hydrolox sustainer and 24 kerolox booster engines, for a takeoff thrust of 162 MN. The base heatshield was water-cooled. Protecting the base area on reentry was identified as a major concern [46].

The vehicle was to operate from a network of canals and artificial lagoons. The landing site was to have been a 5 km diameter artificial pond, which is certainly one way to address the landing accuracy problem [46].

Figure 2.07.05-01: Boeing LEO/"Big Onion" [46]

This proposal illustrates the scalability of VTVL SSTOs to very large sizes. It also anticipates this thesis, in that this vehicle was designed for a similar mission - very high-throughput space transportation.

2.07.06: McDonnell-Douglas DC-X/Delta Clipper

In the 1980s, under the rubric of the Strategic Defense Initiative, the US considered various means to defend against a massed Soviet ICBM strike. In order to launch the space-based elements of the system, several different SSTO RLV designs were considered [54]. General Dynamics and McDonnell-Douglas both proposed VTVLs [55]. The McDonnell-Douglas proposal is most noteworthy, since it resulted in actual hardware - the famous Delta Clipper Experimental (DC-X) [54].

The DC-X was a prototype intended to explore some of the operational characteristics of a VTVL SSTO. It demonstrated vertical take-offs, powered soft-landings, and horizontal divert maneuvers. The team achieved substantial results on modest funds. Unfortunately, funds to continue work were not forthcoming after the prototype was destroyed in a 1996 accident [54]. As with the SERV, the DC-X was unpopular with NASA management, who favored the Lockheed Martin X-33/VentureStar.

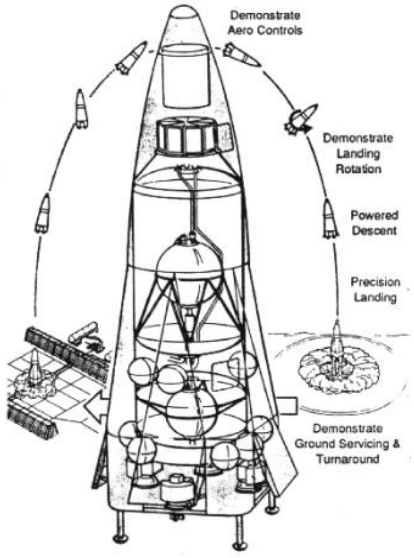

Figure 2.07.06-01: McDonnell-Douglas DC-X/Delta-Clipper [54]

Unlike most VTVL SSTOs, the Delta Clipper was intended to perform a nose-first reentry in order to obtain sufficient cross-range performance. This required that the vehicle turn around in mid-air - a sort of aerial somersault - to land. The DC-X did not have the performance to achieve orbit, which in any event was not its intended purpose. (The planned DC-Y follow-on was to demonstrate orbital capability, and be succeeded by the production DC-1.) It did include many composite parts to reduce mass, including a CFRP LH2 tank, and a gaseous-propellant RCS, like the one proposed for this vehicle.

Chapter 3: Methodology

3.01: Mission simulation

The assumptions of the mission simulation [56] are that:

1. The vehicle is a point mass, whose orientation continuously coincides with its flight path.
2. The rotation of the Earth is neglected. However, this is not a flat-Earth model - the curvature of the Earth is included, and gravity varies with altitude according to the familiar inverse-square law.
3. The ambient pressure and density vary with the geometric height according to an isothermal height-scaling model.
4. The vehicle's drag reference area is simply its base area, and its drag coefficient is a constant $C_D = 0.5$.
5. Engine specific impulse varies linearly with ambient pressure.
6. During ascent, the engine is throttled to maintain the instantaneous thrust-to-mass ratio to under 40 N/kg and the dynamic pressure to under 25 kPa.

Design inputs include:

1. The number and type of main engines
2. The liftoff thrust-to-weight ratio
3. An engine scale factor
4. For mixed and tripropellant propulsion schemes, the switchover criterion

For mixed-propulsion vehicles, the booster engines are throttled to limit the instantaneous total thrust-to-mass ratio at or below the value of the switchover criterion. Booster engines are shut down in pairs, with the remaining engines throttled back up as necessary. (This value will be repeatedly exceeded as the vehicle is relieved of the weight of the weight of propellants, since the main engines have a minimum throttle setting.) When all the booster engines have been shut down, the sustainer engines are throttled and shut down in pairs as necessary to maintain the 40 N/kg limit.

In tripropellant schemes, when the engines are operating in Mode 1, the tripropellant mode, they are shut down in pairs to maintain the vehicle's instantaneous total thrust-to-mass ratio to the switchover criterion. When the Mode 1 thrust of the remaining engines is sufficiently high that all would have to be shut down to avoid exceeding the limit, the engines are switched en bloc to Mode 2. The vehicle subsequently limits its instantaneous thrust-to-mass ratio to 40 N/kg by throttling and shutting down remaining engines in pairs.

During the course of the simulated ascent, the gross mass of the vehicle is decremented at every time step and the quantities of propellant consumed incremented. This allows the burnout mass and ascent propellant requirements to be determined even if nothing is known about their values beforehand.

The ascent V_Δ is obtained by continuously incrementing the acceleration the vehicle would experience at a given time in the absence of losses. Drag, gravity and back-pressure losses are computed by continuously incrementing the acceleration lost to these causes.

The vehicle starts its flight at some small kick angle relative to the vertical. The angle is chosen so that the vehicle achieves the desired orbit via a gravity turn. There is no way to determine the kick angle except to try different values until the correct one is found.

MECO (main engine cut off) occurs when the predicted apogee equals or exceeds 200 km altitude. If MECO occurs within the sensible atmosphere, the effect of drag on the vehicle is neglected, but the deceleration the vehicle would experience is incremented to obtain a V_Δ figure. Notionally, the OMEs (orbital maneuvering engines) fire to counteract this drag. They are fired again at apogee to circularize the orbit. The unpowered exoatmospheric flight phase is modelled as a portion of a patched-conic trajectory. (MECO may occur above the sensible atmosphere.) The circularization burn is modelled as impulsive. These OMS burns must sum to no more than 100 m/s for the trajectory to be considered feasible.

This method, since it neglects the rotation of the Earth, provides the propellant consumption for a launch due north or south. The propellant consumption for a launch to a lower inclination can also be determined. Due to the rotation of the Earth, there will be a certain velocity boost or penalty, depending on the latitude of the launch site and the launch azimuth.

The total V_Δ is known for all times during the ascent. The ascent propellant savings is the difference between the mass of the ascent propellants at burnout and at the time when the vehicle has achieved this V_Δ less the downrange component of the rotational velocity of the launch site. This allows for the payload capacity to any inclination and from a launch site at any latitude to be determined.

Propellant requirements for the OMS, RCS and landing burns are determined using Tsiolkovsky's equation, with the MECO mass as the starting mass. For the landing burn, the sea-level specific impulse is used.

3.02: Mass estimation

For the ascent propellants, the following are added to the propellant requirements:

1. A performance reserve sufficient for 2% of V_{Δ} to orbit
2. Startup losses [57]
3. In-flight losses and vents [57]
4. Trapped/residual propellants [57]

LO2 and LH2 to supply the gas generators and OMS, and possibly for the landing burn, is stored in its own set of tanks. Allowances are made to provide sufficient propellants to meet RCS heating, ITS repressurization and HIAD inflation requirements. The RCS propellants are stored at low pressure in order to maximize storage density in the accumulators, while the repressurization/inflation gas is as hot as possible, in order to achieve sufficient pressure with the minimum quantity of propellant. Propellant requirements for heating and are calculated by assuming that these gases are calorically perfect.

With the total quantities of the various propellants known, the volumetric capacity of the propellant tanks can be determined. A 2% ullage fraction is assumed throughout. Given this geometric and mass information, the empty mass of the vehicle can be estimated. A 15% mass margin is applied to the mass of the vehicle less main engines, and 7.5% to the main engines. The payload is the difference between the allowable inert mass and this predicted empty mass.

The estimated empty mass is the sum of over 30 individual mass items. These include the major structural components of the vehicle (the integral tank system skin, thrust structure, etc.), the main and secondary engines and associated subsystems, forward thermal protection/insulation, the various recovery provisions, and so on.

Most of these masses are estimated using various empirical MERs (mass-estimating relationships) obtained from a database [57]. However, the mass of the various propellant tanks - both internal and non-integral - is estimated using a simple physics-based model.

The ITS containers consist of cylindrical barrel sections and hemi-ellipsoidal bulkheads. Since the time-varying acceleration of the vehicle and the fluid level in each container is known, the maximum hydrostatic pressure in the containers can be determined [58]. A simplified stress analysis is performed, according to whose assumptions the barrel sections are uniformly-pressurized cylinders, and the bulkheads uniformly-pressurized oblate hemispheroids. Worst-case values are obtained and used for design.

The non-integral propellant containers are modelled as uniformly-pressurized spheres for purposes of mass estimation, with a knockdown factor of 3. Note that the secondary ascent propellant tanks - those containing hydrocarbon fuels - are notionally toroidal, as depicted in Figure 2.06.01-01. The exact length of the vehicle body between the leading edge of the thrust structure and the apex of the aft bulkhead is indefinite - it is assumed that, due to the large knockdown factor used to estimate the mass of the secondary ascent fuel tanks, there is a sufficient structural mass allowance to close the design.
The mass of the forward shroud, aft fairing and aft heatshield is determined by multiplying their area by an assumed smeared thickness (as per Table B.01-02) and applying a 5% margin. The material density is as per Table B.01-01.

The empty mass growth factor is also of interest.

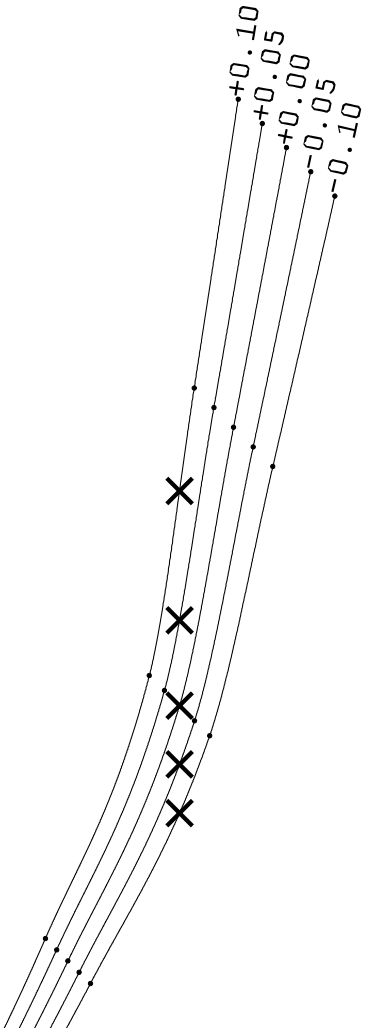

Figure 3.02-01: Schematic of mass-growth estimation methodology

The preceding figure illustrates the method used to determine the empty mass growth factor. Additional data are interpolated and extrapolated from simulation results. The empty mass growth factor - defined as the change in the estimated empty mass for a unit change in payload mass - is the slope of the interpolating curve. The black dots represent directly-obtained design points. The various curves correspond to structural mass growth cases. The 0% case is with the input mass properties as per Appendix B, while the others are with a relative change in the total strucural mass. Xs are interpolated results with the same payload as the 0% structural mass growth case. The mass growth study is generally according to the method of reference [01].

An increase in the structural mass requires a larger vehicle to obtain the same payload capacity. For example, with metholox tripropellant engines, a 22-engine vehicle with a payload of 58136 kg grows from 200222 kg to 216909 kg between the 0% and 5% structural mass growth cases. The various mass items (propellant masses, components, etc.) can be estimated by interpolation in this manner as well, and add up to the correct empty and gross mass totals, which indicates that this method is valid.

3.03: Cost estimation

The system life-cycle cost is assumed to consist of the components:

1. Non-recurring vehicle development cost
2. Non-recurring engine development cost
3. Recurring bare vehicle (less engines) production cost
4. Recurring engine production cost
5. Recurring sacrificial component (payload fairing, HIAD, parafoil) production cost
6. Recurring propellant cost
7. Recurring operations cost

The aforementioned recurring operations cost is considered to include all vehicle and engine maintenance, refurbishment and operations costs. Extra vehicles and engines are procured in anticipation of any losses.

All recurring costs are modified by a power-law experience-curve effect [59], given by

$$17. \rightarrow \quad C_N = C_1 n^{\log_2(b)}$$

where C_N is the cost of the Nth unit produced, C_1 is the first-unit costs, and b is the learning percentage.

Costs, and the ROI, are calculated both on a non-discounted and exponentially-discounted basis, with yearly compounding. The discounting law is given by [60]

$$18. \rightarrow \quad V_1 = \frac{V_0}{(1 + k)^n}$$

where V is an un-discounted value, either positive or negative, k is the discount rate (i.e. the cost of money), and n is the number of compounding periods (here, years) into the future.

Customers are charged at a 50% markup on the non-discounted lifetime average payload-mass specific cost - that is, the non-discounted total program cost, divided by the total mass of payloads launched over the course of the program.

First-unit procurement costs are generated using cost-estimating relations (CERs) derived from TransCost 7.1, with some corrections applied, as the published CERs yield some anomalous results [61].

The assumptions of the cost model are:

01. Development costs are evenly distributed over a five-year period.
02. The five-year development period is followed by a two-year test flight period, for which two vehicles - and sufficient engines - are procured.
03. The two-year test period is followed by a 20-year revenue service period.
04. The program is steady-state - a constant fleet size and total annual flight rate is maintained during the revenue service period.
05. For purposes of calculating discount-rate effects, the compounding periods are years. All acquisitions in a given year are assumed to be in the same compounding period.
06. Replacement vehicles, excepting attrition spares, are procured at equal intervals.
07. Replacement engines, excepting attrition spares, are procured annually in a quantity sufficient for the number of planned revenue flights in that year.
08. Attrition-spare vehicles, with full engine sets, are procured annually in a quantity sufficient to cover anticipated losses (i.e. crashes) in that year. This is assumed to cover any insurance requirements.

09. The vehicle input data are:
    9.1: A maximum annual flight rate of 150 flights/year
    9.2: A 300-flight service life
    9.3: A 10^{-3} chance of loss per flight
10. The engines are assumed to have a service life of 50 flights.
11. An 8% annual discount rate/cost of money is assumed.
12. The operations cost is assumed to cover all necessary activities to complete a mission. A comprehensive operations cost of $1M USD per flight is assumed. This corresponds to about a 1400-man workforce working for 24 hours at $30/man-hour.
13. Bare-vehicle (less main engines) DDT&E (design, development, test and evaluation) costs are predicted by the cost-estimating relationship [61]

$$19. \rightarrow \quad C = 365.4M^{0.48} + 2000$$

where C is the DDT&E cost of the vehicle in engineering man-years, less engines, and M is its empty mass, less engines.
14. Main-engine DDT&E cost is predicted by the CER [61]

$$20. \rightarrow \quad C = 280.6 \times M^{0.52}$$

where C is the DDT&E cost (again in man-years) and M is the mass of the main engine.
15. Bare-vehicle TFU (theoretical first-unit) cost is predicted by the CER [61]

$$21. \rightarrow \quad C = 1.81M^{0.63}$$

where C is the TFU cost in man-years.
16. Main engine TFU is predicted by the CER [61]

$$22. \rightarrow \quad C = 6.90M^{0.52}$$

where C is the TFU cost in man-years.
17. Costs predicted by the preceding CERs are denominated in engineering-man years. One engineering man-year is assumed to be $290000 in 2014 USD [61].
17. For determining the TFU, sacrificial components are assumed to cost $250 per kg of estimated component mass.
18. Propellant costs are as per Table A.01.01-02.

Chapter 4: Results and analysis

4.01: Mass estimates

4.01.01: Basic results

These results are with structural input mass properties as per Appendix B, i.e. with no relative increase or decrease. The primary figure of merit for selecting design properties is the ratio of payload mass to vehicle empty mass. The intention is to obtain fairly (although not exactly) optimal designs, in order to determine their general vicinity, compare propulsion options, and obtain quantitative estimates. It is important to note that these vehicles do not all have the same payload. The different propulsion schemes may still be compared on the basis of these results, however, since each propulsion scheme is at its best, and the maximum size to which the vehicle may be scaled with a given propulsion scheme is certainly an important indicator of merit, and in practice, it would be best to build the largest vehicle possible, since larger vehicles are more cost-efficient.

Lower thrust-to-weight ratios are optimal. For all seven propulsion schemes, the takeoff thrust-to-weight ratio of 1.15 is about the lowest that will still permit the vehicle to make orbit.

For both mixed-propulsion designs, the optimal switchover criterion is around 25 N/kg, which value was used here. For tripropellant designs, the main engines operate in the tripropellant mode all the way to MECO.

The engine codes are in the format SS/BB, where SS is the number of sustainer engines and BB is the number of booster engines. In Table 4.01.01-01, M_0 is the starting (gross lift-off) mass, M_E the empty mass, and M_P the payload mass. The schemes are coded based on the fuels used - H for hydrogen, K for kerosene and M for methane. In the two mixed-propulsion schemes, the fuel codes are separated by a slash.

Table 4.01.01-01: Tabulation of major vehicle parameters

SCHEME	ENGINES	T/W_0	CRIT	$M_0/10^3$ kg	$M_E/10^3$ kg	$M_P/10^3$ kg	M_P/M_E	V_Δ (m/s)
1 H	20/00	1.15	N/A	2951.7	252.8	39.3	0.156	9606
2 K	26/00	1.15	N/A	3763.0	154.9	15.4	0.099	9462
3 M	26/00	1.15	N/A	3764.7	166.6	23.9	0.143	9442
4 H/K	10/10	1.15	25	2844.0	190.8	31.9	0.167	9768
5 H/M	14/06	1.15	25	2910.4	215.6	35.1	0.163	9746
6 HK	22/00	1.15	N/A	3103.8	188.2	45.9	0.244	9613
7 HM	22/00	1.15	N/A	3102.7	200.2	58.1	0.290	9611

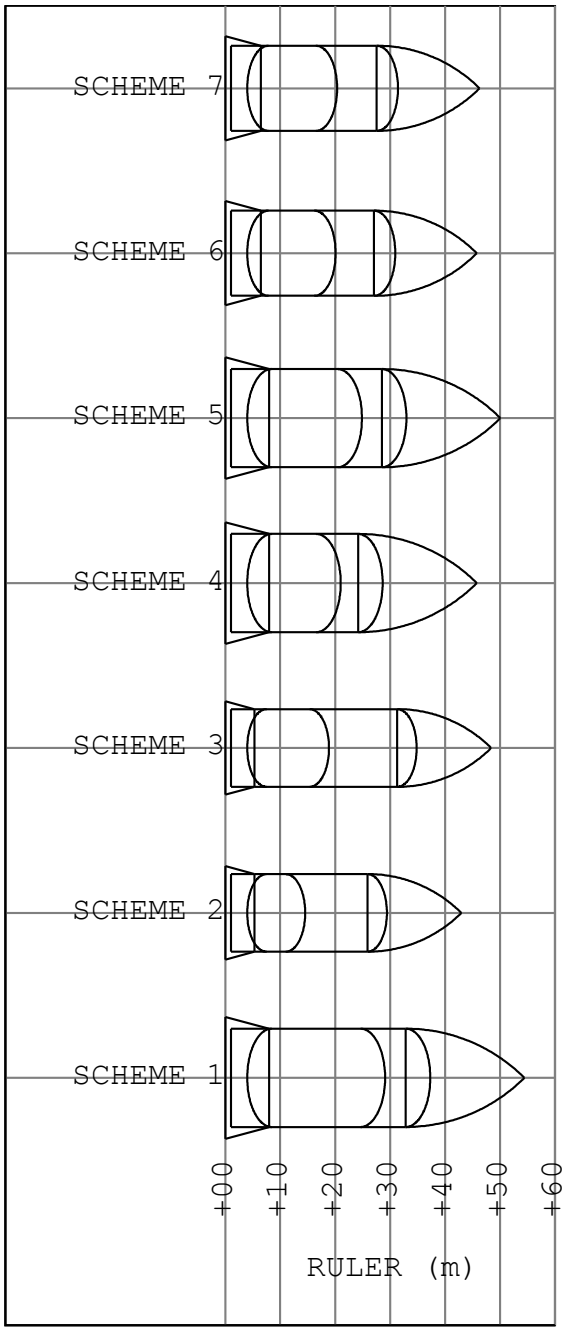

Figure 4.01.01-01: Relative sizes for various propulsion options

The preceding figure depicts the variation in size between designs using the various propulsion schemes. The main engines, XAC and non-integral propellant tanks are omitted for clarity. The relative sizes of the integral propellant containers depends on the density of the integral fuel and the use of a secondary fuel. Schemes 2 and 3, which have the smallest integral fuel containers, have hydrocarbon integral fuels.

These sizes - which result in differing payload masses for the various vehicles - have not been chosen arbitrarily. As mentioned, for each propulsion scheme, there is some ideal number of engines which optimizes the ratio of payload to empty mass. Any more or any less is suboptimal. If the number of engines is greater, the ratio - and even the actual payload - will start to decrease, even as the empty mass and program cost increase, which these results (they are for the pure hydrolox vehicle, but are qualitatively similar to those for the other propulsion schemes) illustrate.

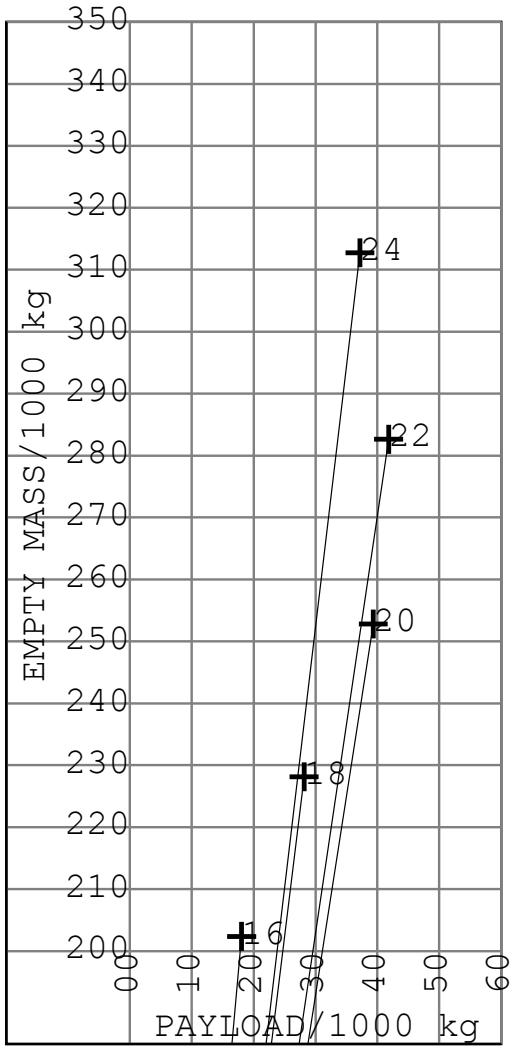

Figure 4.01.01-02: Predicted empty vs. payload mass for hydrolox vehicles with various numbers of main engines

The tail attached to each data point is a line connecting the origin to the data point. Its slope is the ratio between the empty mass and the payload mass. Lower ratios/slopes are better. It is evident that the 20-engine design optimizes this objective.

Figure 4.01.01-03: Undiscounted transportation cost vs. total mass launched for hydrolox vehicles with various numbers of main engines

In addition, as the preceding chart shows, the 20-engine hydrolox vehicle undercuts all other pure hydrolox designs. For all program sizes/total masses launched, the transportation cost, and therefore the total program cost, for the 20-engine vehicle is less than for vehicles with other numbers of main engines.

Improved payload performance at larger sizes (up to a point) is obtained for several reasons. These include the well-known square-cube law, according to which a larger vehicle will have a greater ratio between its enclosed volume and its surface area. This reduces the mass of propellant tankage - less structure is required to enclose their contents.

Above a certain number of engines, however, the vehicle enters a negative-growth regime - the payload mass decreases even as the empty mass and costs increase. This is primarily due to increases in the relative mass (with respect to the total empty mass) of the structure and recovery provisions.

Since the vehicle can only have up to two concentric circles of main engines (more might result in an excessively complex and heavy thrust structure), above a certain number of engines, the increase in the required base area/base diameter results in a reduction in frontal thrust density, increasing ascent losses. It also increases the diameter of the integral tank system (whose mass is sensitive to its diameter, since the stresses in the barrel sections/bulkheads are proportional to the diameter) and the surface area of the base heatshield and aft fairing. Additionally, the screwjacks, which are heavy items, must be made longer in order to allow the HIAD to clear the outboardmost main engines on deployment.

Transportation costs are proportional to the ratio of the payload to the empty mass of the vehicle, which is the main driver of hardware production costs, the largest component of the total program cost. Therefore, for a given propulsion scheme, transportation costs are minimized by maximizing the ratio of the payload mass to the empty mass.

For all other propulsion schemes, the designs that have been chosen (in terms of the number of sustainer/booster main engines) have these two important properties: maximum ratio of payload to empty mass, and minimum transportation costs.

Note that these vehicles have low fineness ratios, since there must be a sufficient base area for the ascent engines and XAC.
This is advantageous - it results in a stiffer airframe, and prevents wake flow implementing during reentry.

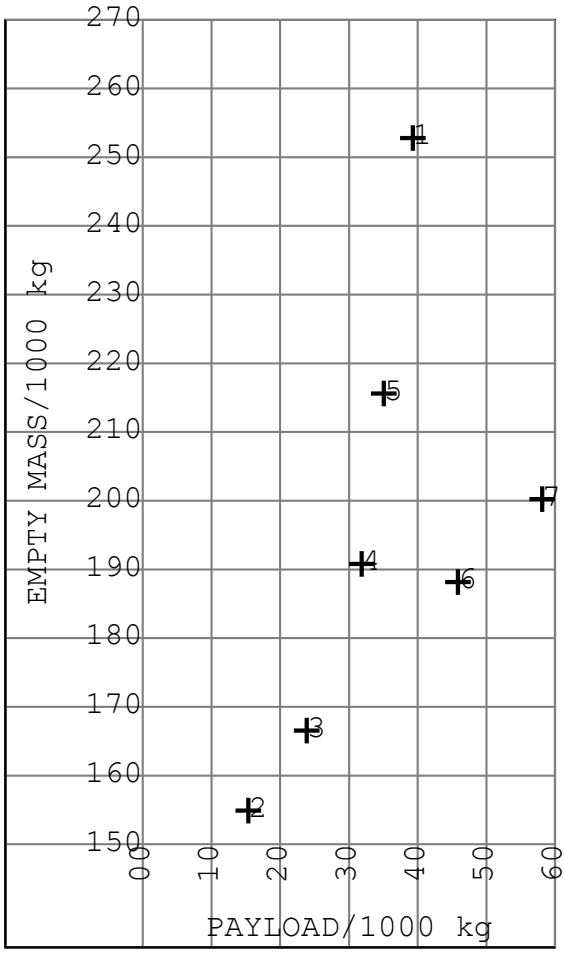

Figure 4.01.01-04: Predicted empty vs. payload mass

Note that, in the preceding figure, Schemes 2 and 3 (pure kerolox and metholox, respectively) cluster together, since their main engines are similar to each other and they both have the same number. As a result, they have the same base/frontal area and ITS diameter, although - as can be seen from Figure 4.01.01-01 - the metholox vehicle, with its less dense fuel, is longer. Schemes 6 and 7 likewise cluster together, for similar reasons.

Scheme 1 - the pure hydrolox vehicle - is the largest and heaviest. This is due to the low bulk density of its hydrolox propellant combination, and the low frontal thrust density/thrust-to-weight ratio of its main engines, which are baselined from the SSME.

The tripropellant vehicles outperform their mixed-propulsion counterparts. They are smaller and lighter but have a much greater paload capacity.
This is partly due to the greater frontal thrust density/thrust-to-weight ratio of the RD-704-derived tripropellant engines.

Some of the advantage of the RD-704-derived tripropellant engines may not be due to the use of three components per se, but simply because they represent more advanced/capable technology. They represent more recent technology than the NK-33/SSME. In particular, they operate at a very high chamber pressure - about 290 bar [08], as compared to approximately 200 bar for the SSME [06] and 150 bar for the NK-33 [07], which results in a higher thrust-to-weight ratio, higher frontal thrust density, and better expansion - especially at lower altitudes - through the nozzle.

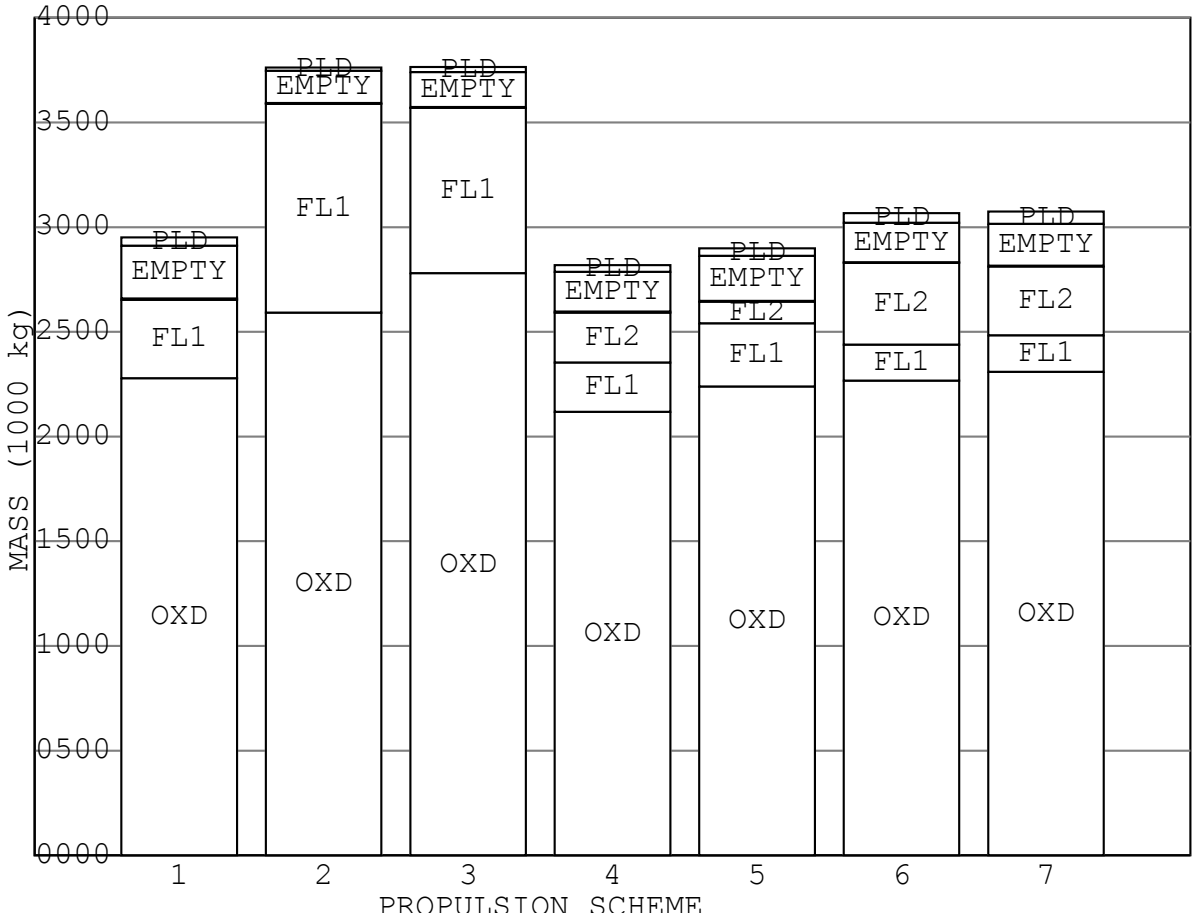

Figure 4.01.01-05: Gross mass breakdowns

In the preceding figure, "FL1" signifies the integral fuel, and, for mixed/tripropellant schemes, "FL2" the secondary fuel. "OXD" includes all oxidizer, including for post-ascent maneuvers.

LH2 carried for post-ascent maneuvers is included, but not labelled - the quantity is very small.

Schemes 2/3 and 6/7 have very similar GLOMs, since they have the same takeoff T/W and number of main engines, which have similar thrusts. Due to the difference in O/F ratio, schemes employing methane use a smaller quantity of hydrocarbon propellant and more oxidizer than those employing rocket kerosene. The tripropellant vehicles both carry less liquid hydrogen and more hydrocarbon fue than their mixed-propulsion counterparts, reducing their empty mass.

Some of these results (that is, the difference between the mixed/tripropellant vehicles) may be an artifact of the engine operation scheduling for mixed-propulsion vehicles, according to which the booster engines are shut down in pairs before the sustainer engines. Whatever the reason, the tripropellant vehicles use relatively more hydrocarbon fuel and therefore operate at a higher bulk density than the mixed-propulsion engines.

4.01.02: Empty mass breakdowns

These results are with input mass properties as per Appendix B. For the empty mass breakdowns in this section, the category codes are:

01. PMN: Main propulson
02. PSC: Secondary propulsion (OMS, RCS, associated equipment)
03. STC: Structure
04. FTP: Forward TPS
05. RCV: Non-sacrificial recovery provisions
06. MSC: Miscellaneous/other
07. SHD: Forward shroud (sacrificial)
08. PFL: Landing parafoil (sacrificial)
09. HAD: HIAD (sacrificial components - bladder, envelope)
10. MGN: Growth
11. TOT: Total

These tabulated mass data are in kilograms.

Table 4.01.02-01: Absolute empty mass breakdowns

SCHEME	1	2	3	4	5	6	7
PMN	82302	50029	50598	60987	69661	57168	59230
PSC	1450	1267	1295	1362	1403	1359	1394
STC	62991	38088	43684	47989	54963	47527	51210
FTP	8280	4908	5510	7062	7668	5909	5968
RCV	20283	9903	11090	14934	16876	14608	16149
MSC	15450	14369	14491	13256	14061	13987	14535
SHD	5247	3283	3283	5247	5247	3942	3942
PFL	6508	3550	4031	4305	5000	5106	5693
HAD	21899	11397	13023	13918	16370	16898	18998
MGN	28372	18111	19545	21740	24378	21676	23103
TOT	252781	154904	166550	190801	215627	188179	200222

Note that Scheme 1 has a very heavy main propulsion system, mainly due to the low thrust-to-weight ratio of the SSME baseline, and a heavy structure, due to its low bulk density.

Table 4.01.02-02: Relative empty mass breakdowns

SCHEME	1	2	3	4	5	6	7
PMN	0.3256	0.3230	0.3038	0.3196	0.3231	0.3038	0.2958
PSC	0.0057	0.0082	0.0078	0.0071	0.0065	0.0072	0.0070
STC	0.2492	0.2459	0.2623	0.2515	0.2549	0.2526	0.2558
FTP	0.0328	0.0317	0.0331	0.0370	0.0356	0.0314	0.0298
RCV	0.0802	0.0639	0.0666	0.0783	0.0783	0.0776	0.0807
MSC	0.0611	0.0928	0.0870	0.0695	0.0652	0.0743	0.0726
SHD	0.0208	0.0212	0.0197	0.0275	0.0243	0.0209	0.0197
PFL	0.0257	0.0229	0.0242	0.0226	0.0232	0.0271	0.0284
HAD	0.0866	0.0736	0.0782	0.0729	0.0759	0.0898	0.0949
MGN	0.1122	0.1169	0.1174	0.1139	0.1131	0.1152	0.1154
TOT	1.0000	1.0000	1.0000	1.0000	1.0000	1.0000	1.0000

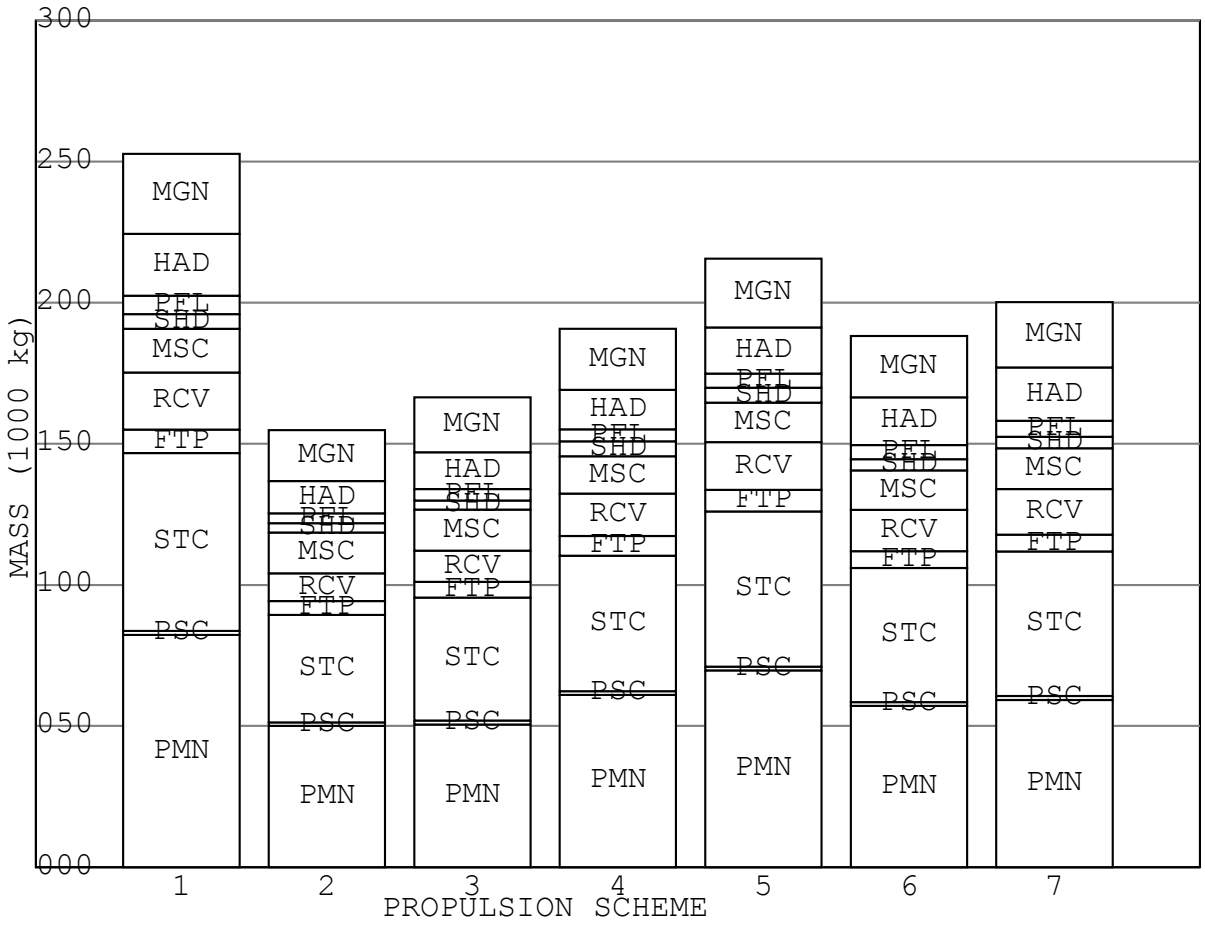

Figure 4.01.02-01: Absolute empty mass breakdown bar chart

For all propulsion schemes, the structure and main propulsion subsystem account for slightly under three-fifths of the empty mass. The relative mass breakdowns are similar for all schemes considered.

One of the main objectives of this study is to evaluate the HIAD/XAC, from the standpoint of reducing the mass of the recovery/protection provisions. The relative mass is tabulated:

Table 4.01.02-03: Tabulation of relative mass of recovery provisions

SCHEME	RCV + HAD + FTP + PFL	RCV	HAD	FTP	PFL	RATIO
1	0.2253	0.0802	0.0866	0.0328	0.0257	3.35:1
2	0.1921	0.0639	0.0736	0.0317	0.0229	4.10:1
3	0.2021	0.0666	0.0782	0.0331	0.0242	3.85:1
4	0.2108	0.0783	0.0729	0.0370	0.0226	3.61:1
5	0.2130	0.0783	0.0759	0.0356	0.0232	3.58:1
6	0.2259	0.0776	0.0898	0.0314	0.0271	3.33:1
7	0.2338	0.0807	0.0949	0.0298	0.0284	3.19:1

The non-sacrificial recovery provisions (the XAC, landing gear, etc.) mass about as much as the HIAD itself. RCV includes the mass of the landing gear. The figure of merit (RATIO) is the empty mass of the vehicle, less the forward shroud and all recovery provisions, a unit mass of the recovery provisions will recover. These figures somewhat understate the performance of the HIAD/RCV, since the reference mass used does not include, among other items, the mass of the landing propellants.

By comparison, on its tenth flight, OV-103 (Discovery) had a total dry mass of 172397 lb_M (78198 kg), of which 50720 lb_M (23006 kg) was induced environmental protection, wing-group structure, and landing gear. The gross vehicle weight was 249502 lb_M (113172 kg), including various propellants and other fluids [62]. For the Shuttle, the analogous provisions recover about four kilograms (3.92:1) of vehicle from orbit, in addition to their own mass. This figure somewhat overstates the performance of the Shuttle's recovery provisions, since it includes the payload, as well as the mass of propellants that would be consumed prior to entry. With respect to the empty mass only, the ratio is 2.40:1.

Analogous (i.e. directly comparable to the TFU as used here) cost figures for the Orbiters are hard to obtain. It is assumed that OV-103 costs $5.76 billion in 2014 USD, or $2 billion in 1980 USD. Assuming that component costs are linearly proportional to mass, the recovery provisions cost $1.69 billion. It is assumed that these can last for 300 flights with no upkeep. Given the same assumption, the non-sacrificial recovery provisions for the metholox vehicle, plus sufficient HADs for 300 flights, with no production-curve effects, cost $1.51 billion, most of which is for replacement HIADs. Going by the orbiter gross vehicle mass and the metholox empty mass, the recovery provisions for the orbiter and the metholox VTVL SSTO return a total of 33951600 kg and 60066600 kg respectively, for costs of about $50/kg and $25/kg, again respectively.

The concept recovery provisions can recover an average of almost 50% more mass from orbit than the wings, landing gear and induced environmental protection on the Shuttle, at the expense inferior cross-range capability. They also provide for a gentle aerothermodynamic environment on reentry. And they can recover about twice the mass for a given cost, even without taking into account the expensive refurbishment the Shuttle's TPS required. However, probably only actual operational experience can establish the advantage for certain. Other winged/lifting vehicles - either single-stage, or the orbiter stages of multi-stage systems - may well outperform the Shuttle and compare more favorably in these respects. Unlike most of these, however, the Shuttle has actually been built and flown.

4.02: Structural mass growth effects

4.02.01: Empty/gross mass and empty mass growth factor

The results presented here are both with the input mass properties as per Appendix B, and for the several cases corresponding to various relative changes (-10%, -05%, +05% and +10%) in the structural mass. Missing bars in these bar charts correspond to cases where the design cannot make it to orbit with a non-negative payload. These cases are said not to have closed.

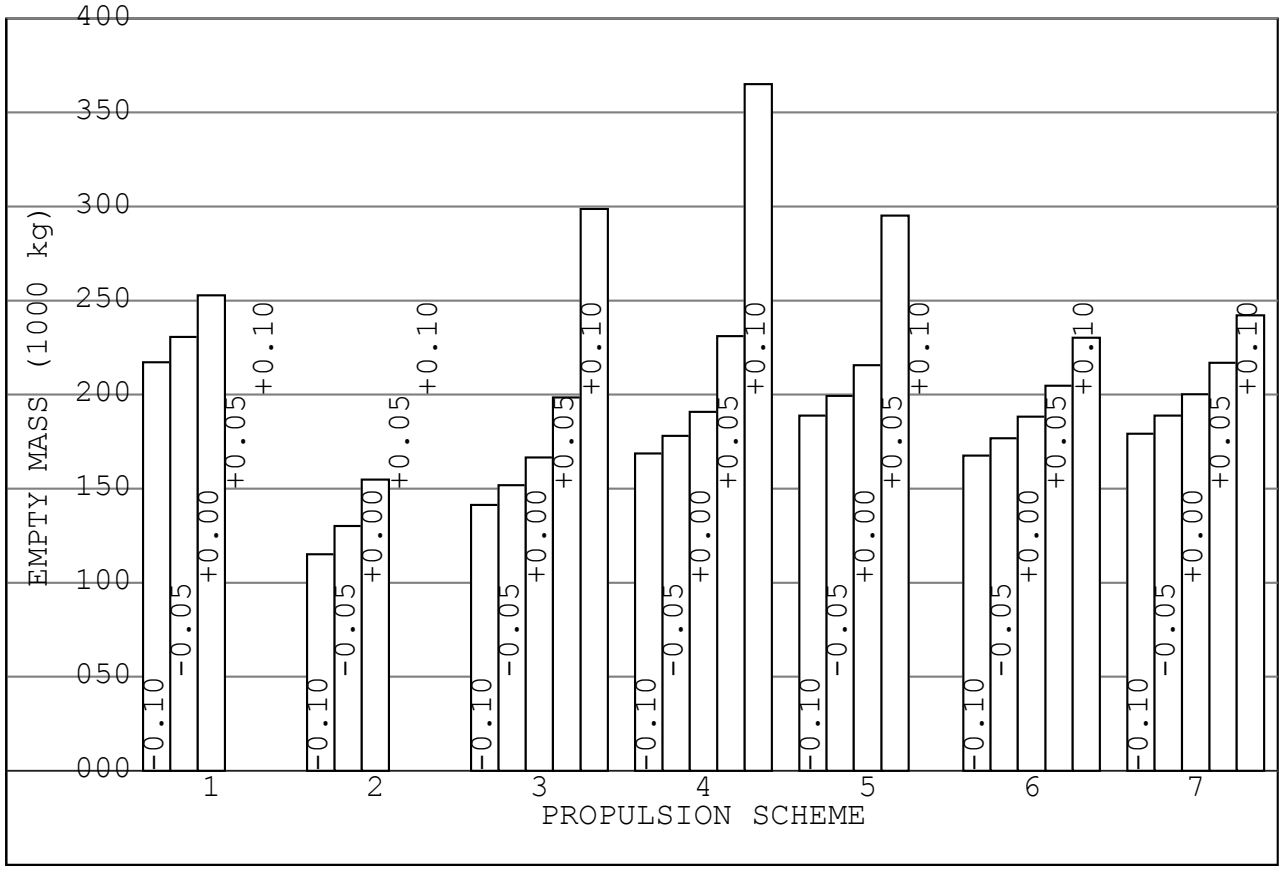

Figure 4.02.01-01: Empty mass bar chart

As expected, structural mass growth results in a heavier empty vehicle. The various propulsion schemes maintain their relative standing at corresponding structural mass growth cases. The pure hydrolox and pure kerolox vehicles do not close for either of the two positive growth cases, while the mixed hydrolox/kerolox vehicle does not close at +10% structural mass growth. The tripropellant vehicles grow much less than the mixed propulsion and pure metholox vehicles. Note that even with a 10% increase in structural mass, both mixed-propulsion vehicles are lighter than the pure hydrolox vehicle with no increase.

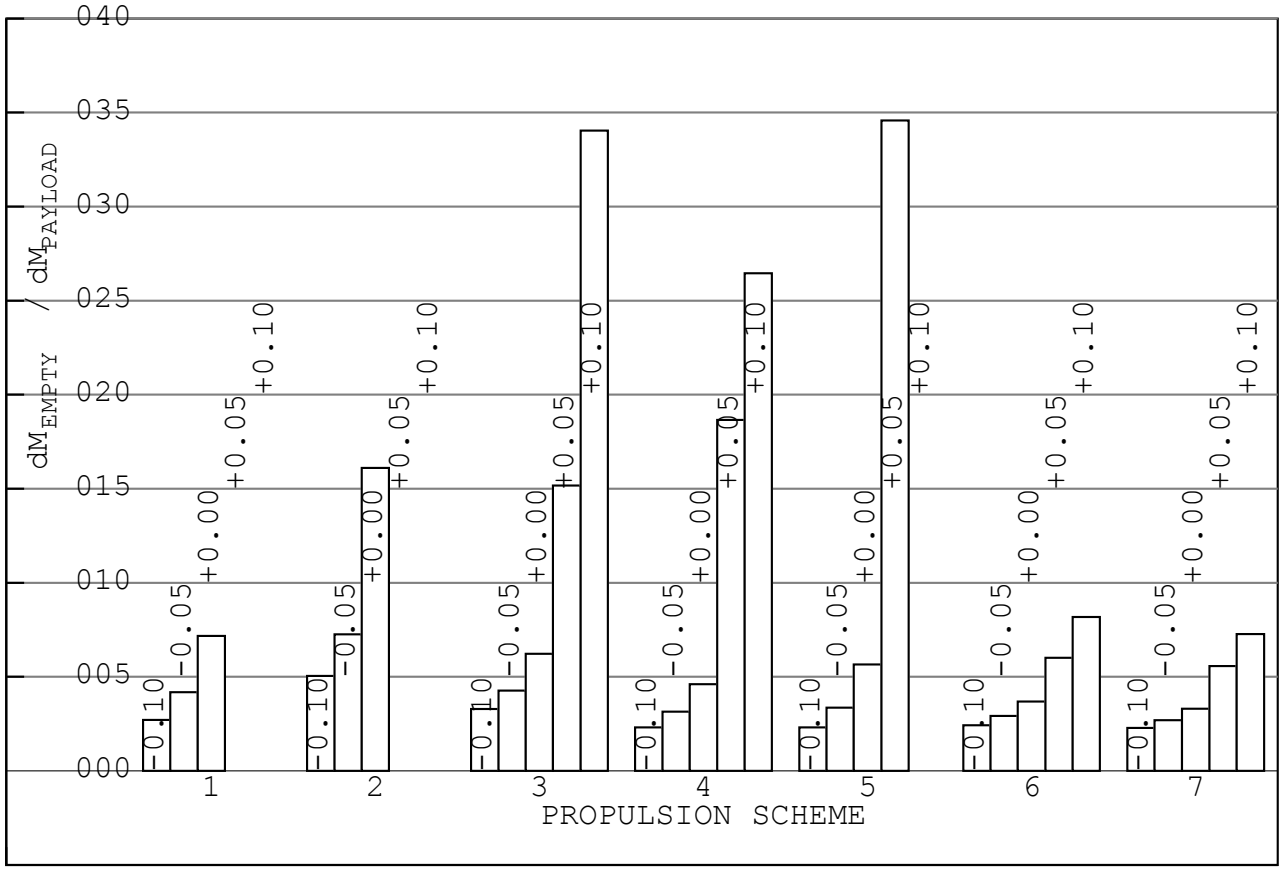

Figure 4.02.01-02: Empty mass growth factor bar chart

These data show that the empty mass growth factor, at least as defined here - the increase in the empty mass of the vehicle for a unit increase in payload mass - is not simply the ratio between the empty mass of the vehicle and the payload, as some sources define it. However, they are clearly related - the pure kerolox vehicle, which has the poorest relative payload performance, is also the most sensitive to weight growth, while the tripropellant vehicles, which have the best relative payload performance, are the least sensitive.

Empty mass growth factor predicts which vehicles will not close with an increase in structural mass - the pure hydrolox and kerolox and mixed hydrolox/kerolox vehicles are the three most sensitive among the designs considered.

The results obtained for the mixed hydrolox/metholox vehicle are interesting - the design does close for a 5% structural mass increase, but there is an enormous leap in the empty mass growth factor. This can be attributed to the use of SSMEs and the relatively low bulk density.

Apart from the pure kerolox vehicle, all of these designs achieve a growth factor under 10 at a 0% structural mass increase.

The more growth-sensitive designs benefit from decreases in the structural mass most, in the sense of achieving a reduction in the empty mass growth factor. This indicates that these designs are the most sensitive to structural mass growth in particular.

These results, as with the others obtained, indicate the advantages of using dense fuels to increase the propellant bulk density, and of achieving a high frontal thrust density/engine thrust-to-weight ratio. Once again, the mixed-propulsion vehicles outperform the pure-propulsion vehicles, and are outperformed in turn by the tripropellant vehicles.

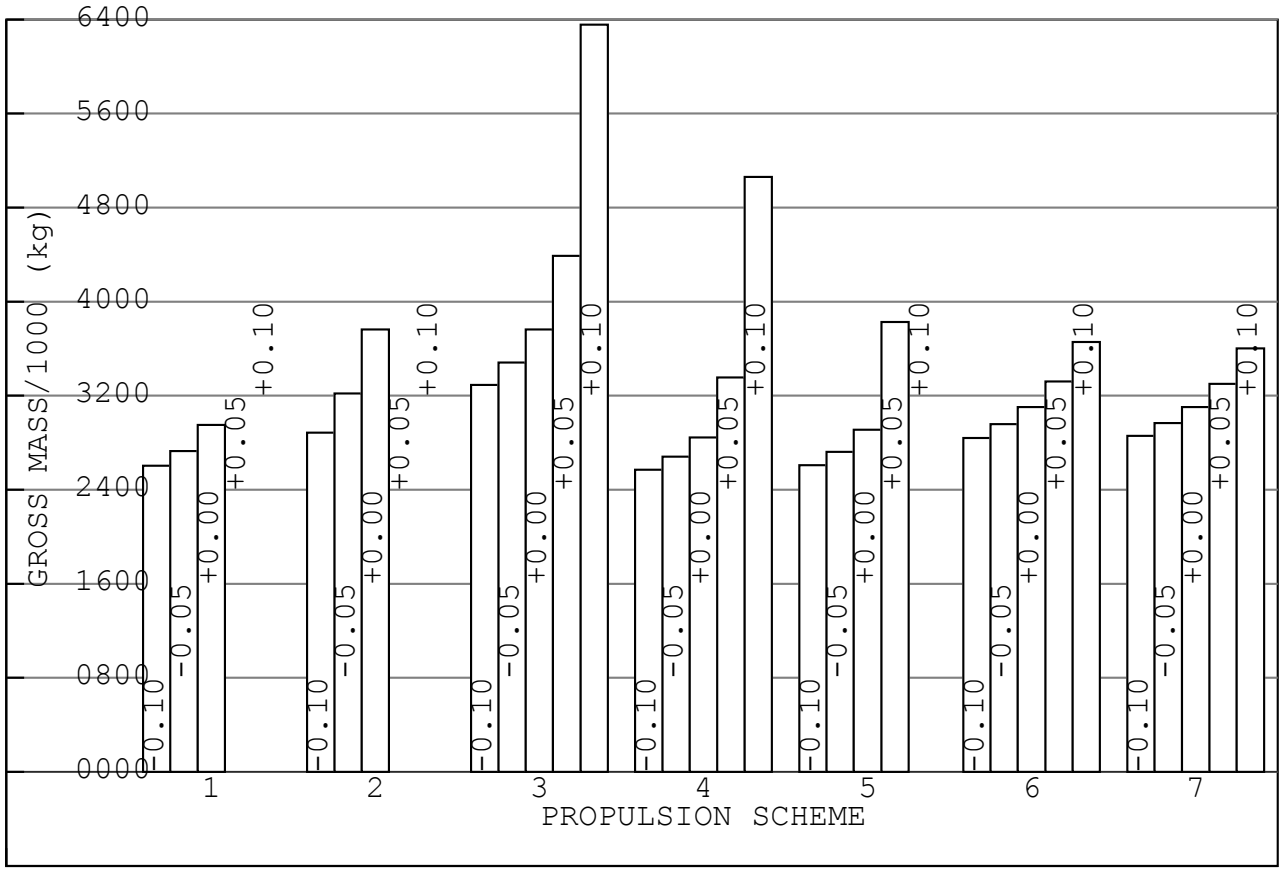

Figure 4.02.01-03: Gross mass bar chart

These gross mass results have been obtained mainly for the sake of completeness. The empty mass/empty mass growth factor are of more interest, since these results are the main predictor of cost/difficulty of development, respectively, whereas the GLOM is mostly cheap propellant that is used to fill the tanks only when the vehicle is secure on the pad.

4.02.02: Empty mass breakdown effects

The category codes for these relative empty mass breakdowns are:

01. A: Main propulsion
02. B: Structure
03. C: Non-sacrificial recovery provisions, HIAD bladder/envelope
04. D: Forward TPS, secondary propulsion, forward shroud, recovery parafoil, misc./other
05. E: Growth

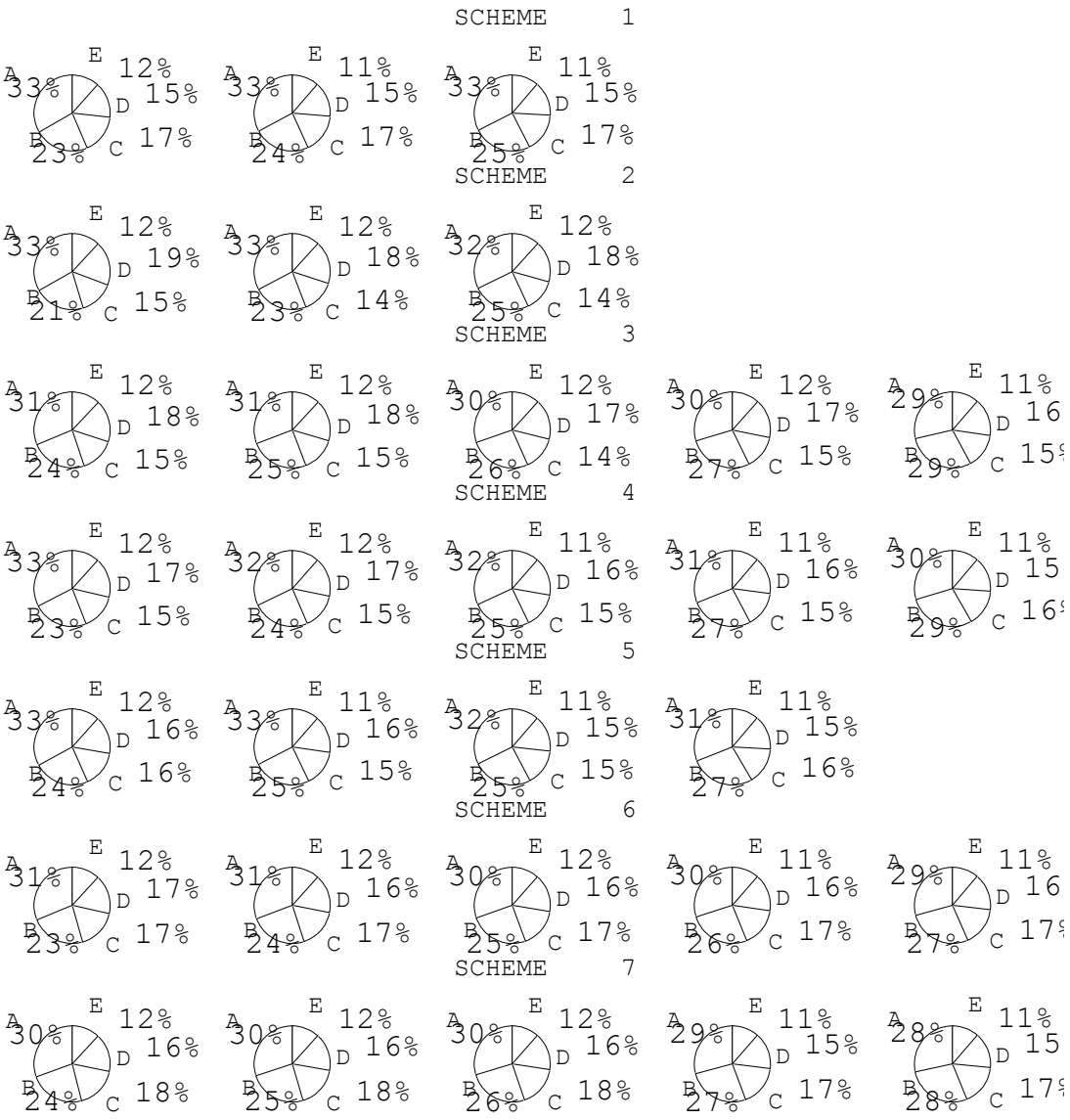

Figure 4.02.02-01: Relative empty mass breakdown pie charts

Apart from the expected increase in structural mass, the relative masses remain about the same - nothing interesting happens.

4.03: Cost predictions

4.03.01: Basic program cost information

The economic results presented here are with input mass properties as per Appendix B. All costs are in constant-value 2014 USD. The program size parameter is essentially the total number of flights, although given the differing characteristics of the various vehicles, the total payload delivered after some number of flights for two different vehicles will not be the same.

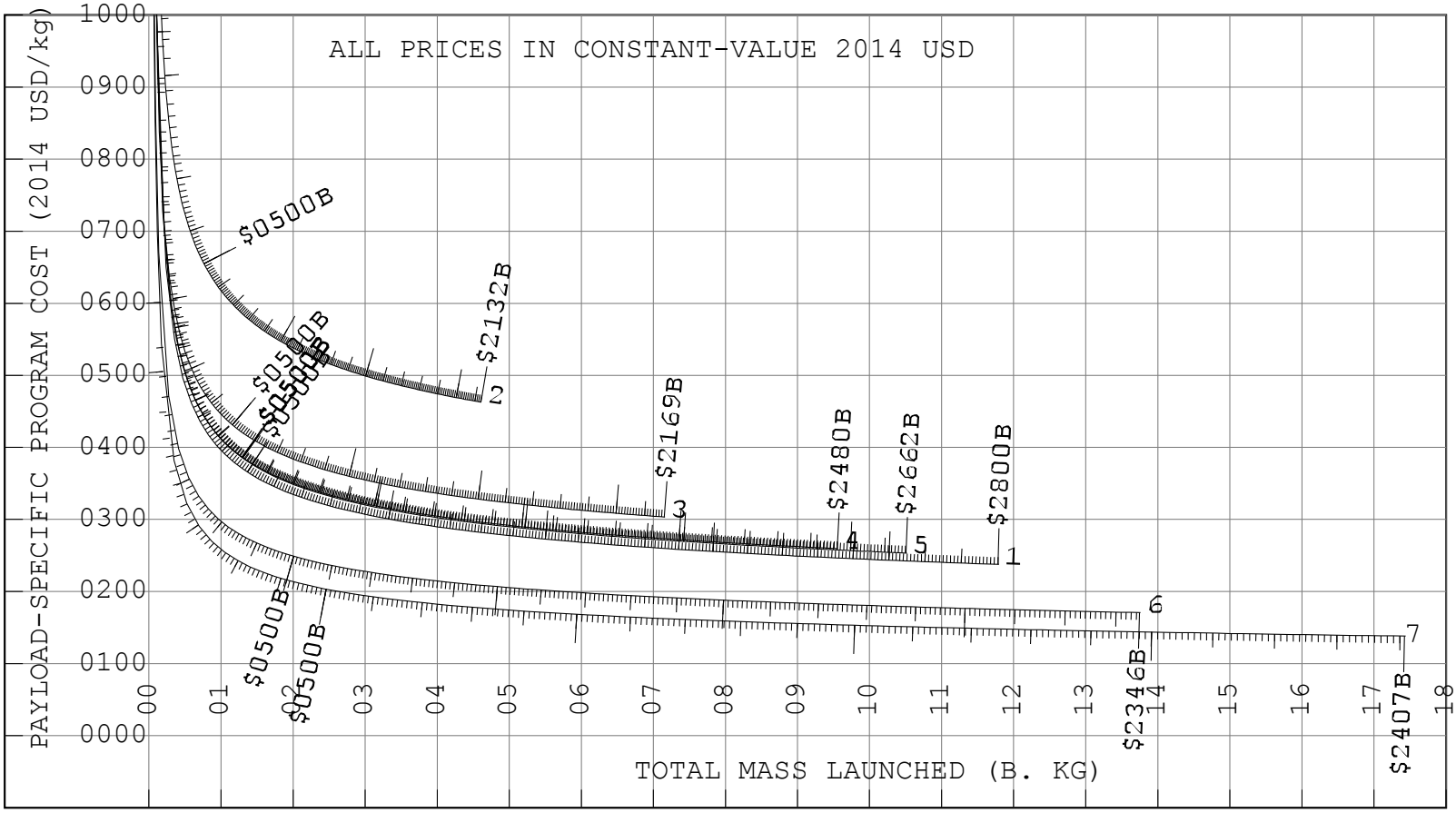

Figure 4.03.01-01: Undiscounted program cost vs. total mass launched

Readers of the PDF version may zoom in to examine the chart in more detail without any loss in quality. Program cost intervals of $10 billion, $100 billion and $500 billion are marked on the curves (as ruler marks) in Figure 4.03.01-01. For all vehicles, the maximum number of revenue flights is 300000 over a 20-year operational period, which corresponds to a total production of 1302 vehicles, of which 300 are attrition spares and 2 are full-sized prototypes. The total number of main engines to be produced varies, but will exceed a hundred thousand for the largest programs.

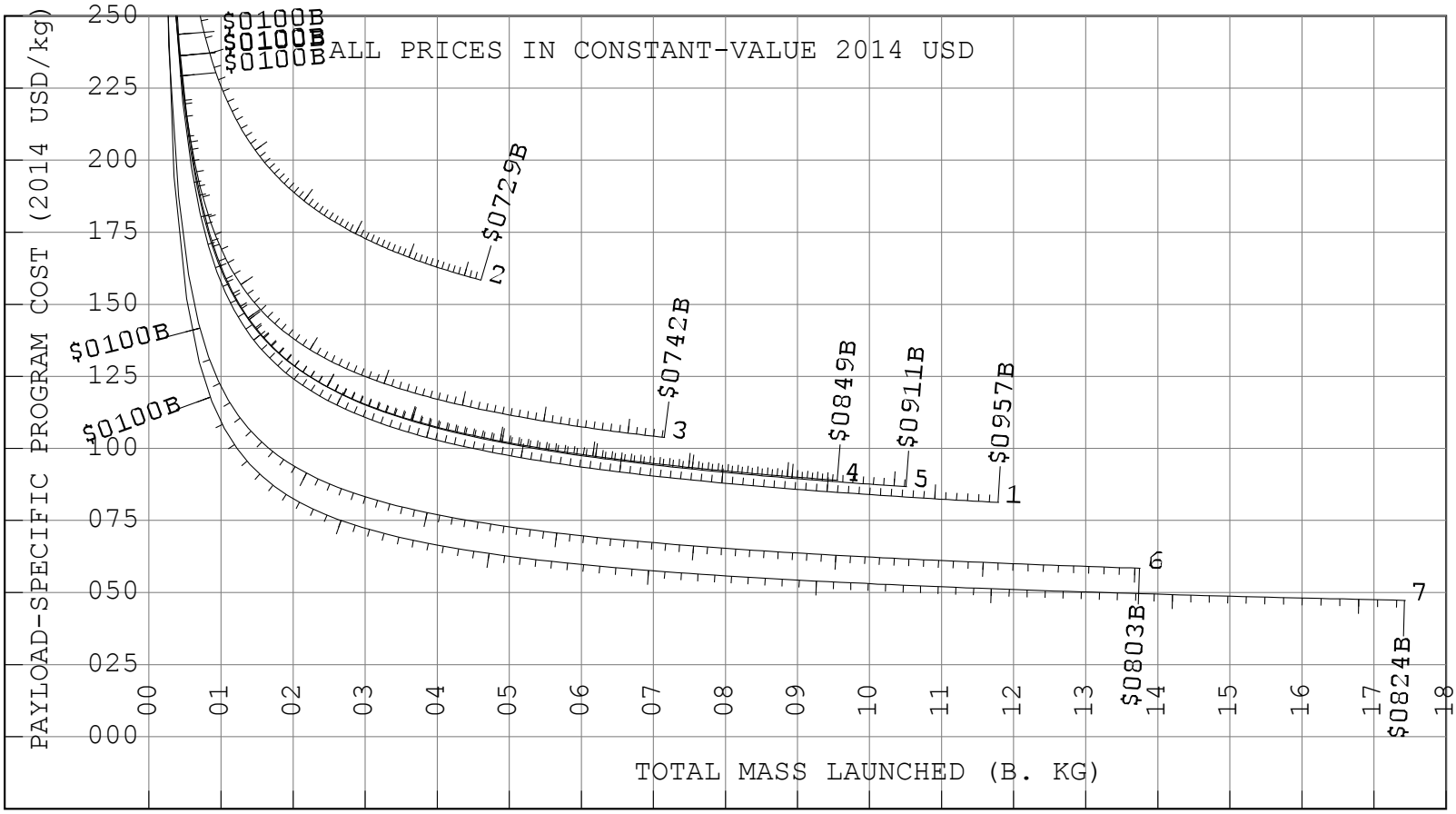

Figure 4.03.01-02: Discounted program cost vs. mass launched

The discounted program costs are calculated on the basis of an 8% annual discount rate. The discounted and undiscounted program cost results are qualitatively similar. Discounted program cost intervals of $100 billion and $10 billion are marked (as ruler marks) on the curves in Figure 4.03.01-02.

For all propulsion schemes, the payload-mass specific program cost - the ordinate - declines rapidly before leveling out. A program curve should level out at the lowest possible total mass launched and smallest possible payload-mass-specific program cost.

The pure kerolox vehicle, due to its poor payload performance, also fares poorly in economic terms, as does the pure metholox vehicle, although to a lesser extent. The two mixed-propulsion vehicles are very close, with the mixed hydrolox/metholox vehicle - 5 - being slightly cheaper.

Surprisingly, for a given total payload mass, the pure hydrolox vehicle undercuts all but the two tripropellant vehicles, since the hydrolox vehicle has the largest absolute payload.

It therefore requires the fewest flights to deliver a given total payload mass, and also the fewest engines and vehicles - which costs dominate the total at large program sizes - to be manufactured. It appears that the absolute payload mass is the best predictor of costs, since the rank order of the various vehicles in economic terms is the same as their rank order in absolute payload mass.

The two tripropellant vehicles perform very well, achieving lower payload costs and passing the knee of the curve earlier than any of the other propulsion schemes.

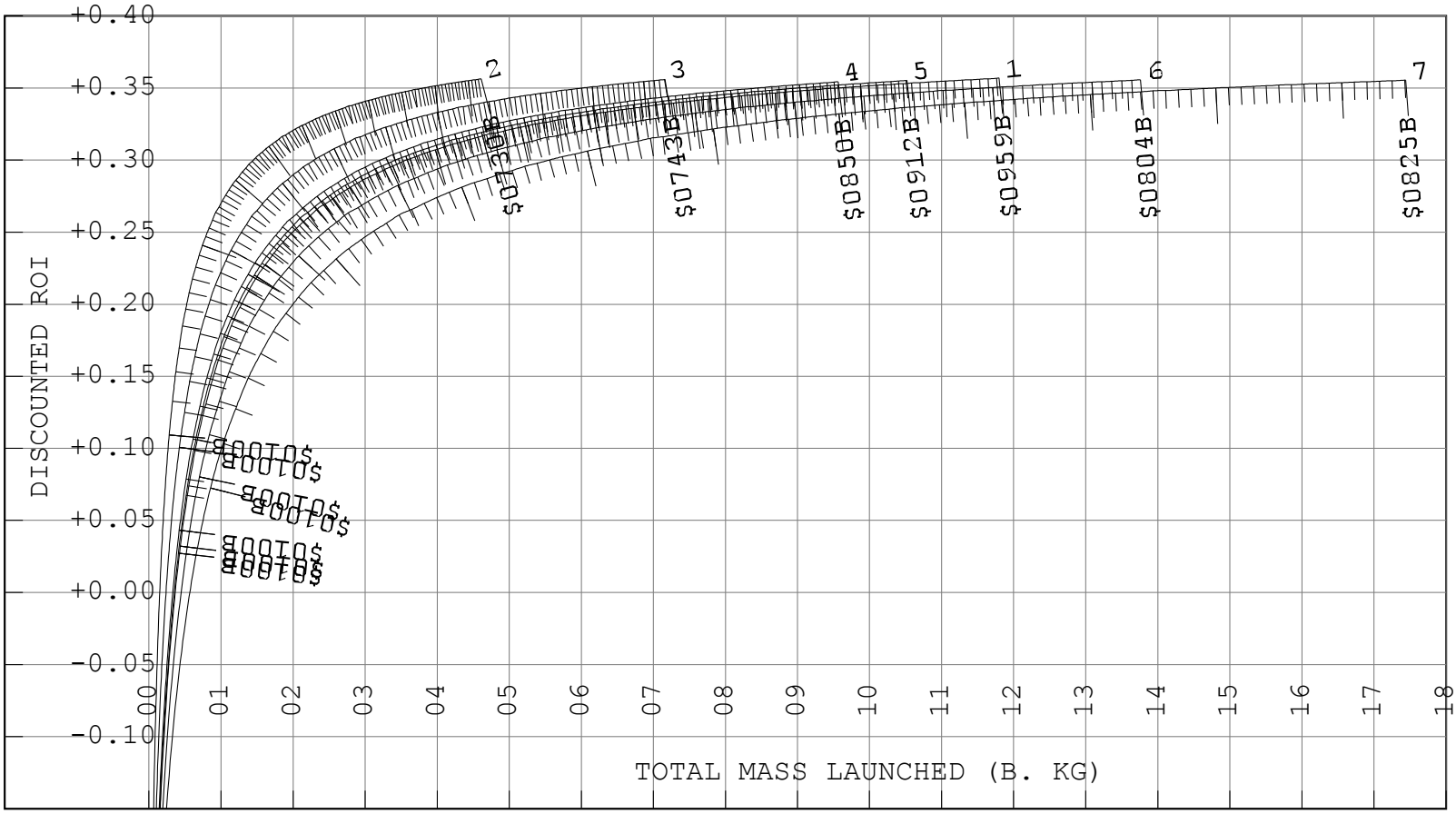

Figure 4.03.01-03: Discounted return on investment vs. total mass transported

These discounted ROI are calculated on the basis of customers being charged at a 50% markup on the undiscounted payload-specific program cost, which corresponds to a 50% undiscounted ROI. For a given number of flights, the discounted ROIs achieved by two different vehicles will be very similar.

Present-day launch costs, using multistage expendable rockets, are usually quoted as around $10000/kg, while SpaceX may achieve, with developments of its current multi-stage rockets, about $1160/kg [63], and the historical OTRAG concept about $3000/kg [64].

According to these data, with hydrometholox tripropellant engines, this concept has the potential to achieve a nearly two orders of magnitude reduction in launch costs as compared with current expendable rockets, and can still significantly undercut more advanced types of expendables.

To put these figures in perspective, the mass of the Great Pyramid at Giza [65] is a mere 6×10^9 kg or so - slightly over a third of the total payload the tripropellant hydrometholox vehicle can launch over the course of 300000 flights. The undiscounted yearly average cost for such a program - about $90 billion USD - is about the GDP of Mississippi, Nebraska or Slovakia [66][67], and the total cost of $2407 billion USD compares with the GDP of the UK, France or California [66].

One interesting result is the lack of intersections/crossovers between these cost curves, at least within the bounds of the chart window. This is addressed as follows.

At least for any respectably-sized program, the non-recurring costs are a pittance. As the results in Subsection 4.03.02 demonstrate, the engine and bare-vehicle development costs rapidly decrease as a fraction of the total for larger program sizes. The initial difference between the various vehicles is therefore relatively small. Any advantage the - for example - kerolox vehicle may have over the metholox vehicle, due to lower upfront costs, is rapidly erased by the metholox vehicle's superior payload performance. For a given total expenditure, the metholox vehicle will have delivered more payload, since the metholox vehicle's superior payload performance makes the expenditure on vehicles and engines go further.

Note also the ordinate limits of the charts. For the undiscounted charts, for example, only the portion of the curve below $1000/kg is plotted. For each propulsion scheme, the program must be fairly large to reduce transportation costs to this level. This ensures that the aforementioned hardware costs dominate the total.

4.03.02: Program cost components

Results are only presented for the pure metholox vehicle. The corresponding results obtained for the other propulsion schemes are similar.

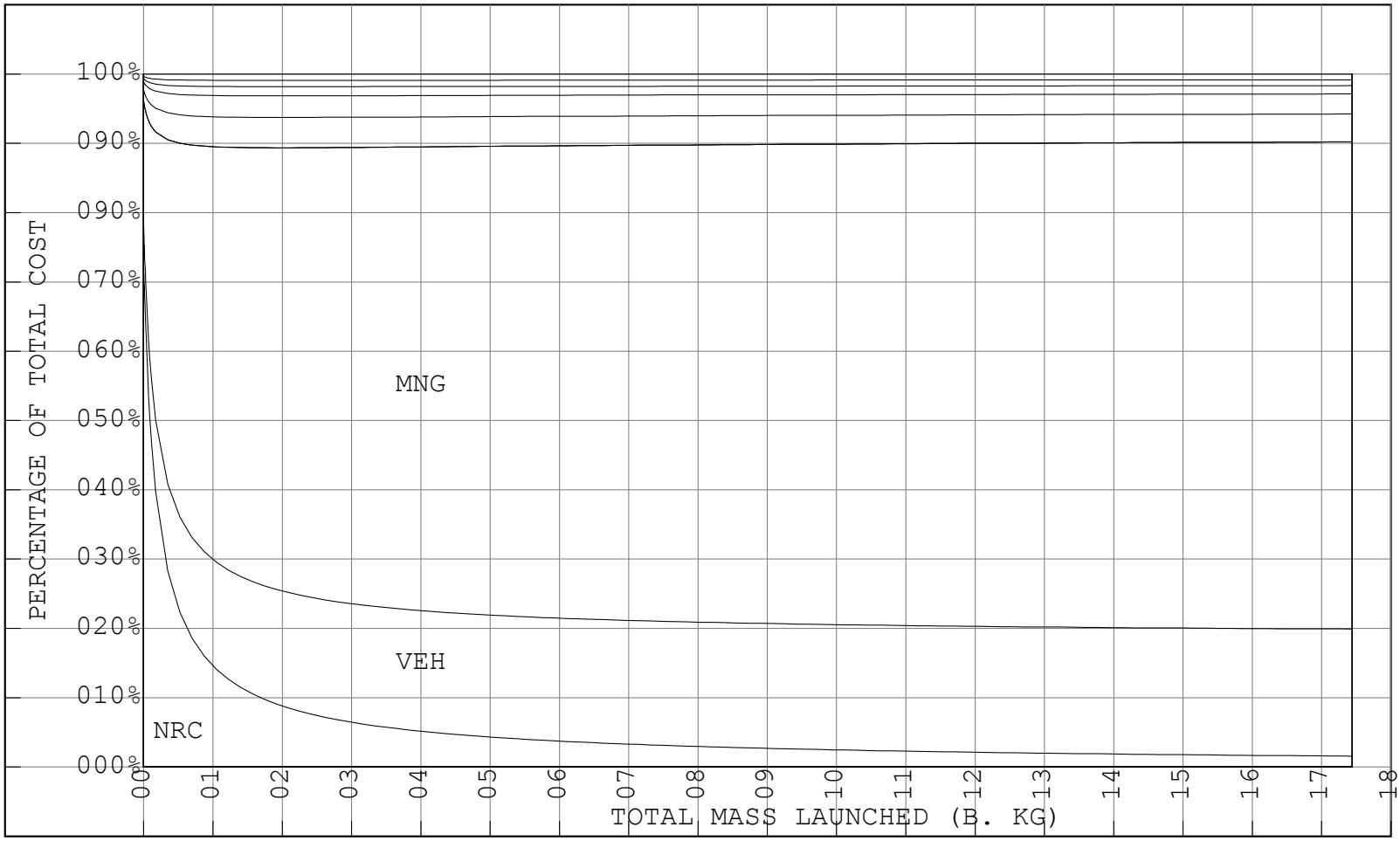

Figure 4.03.02-01: [INDICATIVE PROGRAM COST BREAKDOWN CHART]

At small program sizes, the non-recurring development costs are most of the total, but for larger programs, the cost of vehicles and main engines - whether there is one type or two - dominate. Other costs - the propellants, sacrificial vehicle components, and operations - are a relative pittance.

The change between the non-recurring and the bare vehicle/engine costs comprising most of the total corresponds to the leveling off of the total cost curves in Figures 4.03.01-01 and 4.03.01-02, as the average cost approaches the incremental cost.

In these charts, the spacing between tick marks on the curves narrows and then widens again, but since the curves level off, it takes fewer tick marks to span a given horizontal interval. In other words, the marginal cost, at least according to this model, decreases for larger program sizes.

Figure 4.03.02-01 helps to explain this. Given the assumptions of this analysis, the non-recurring costs are the same for all program sizes using a given vehicle. More payload is delivered by building more vehicles and engines in order to perform more flights. Due to production-curve effects, the cost of a new engine or bare vehicle - as well as the other recurring costs - decreases for larger production runs. And since these dominate the total program cost, and are the only program-size-sensitive term, the incremental cost likewise decreases.

Chapter 5: Recommendations and conclusions

5.01: Conclusions

1. This concept - an all-rocket VTVL SSTO, with a CFRP-laminate structure, pressure-stabilized integral propellant tanks, and a HIAD for reentry - can be realized. According to the results obtained, such a vehicle can be built with sufficient performance to deliver some non-negative payload to orbit and return.
2. The use of dense propellants, even at the expense of some I_{SP}, is advantageous. The increased bulk density reduces the structural mass of the vehicle. Engines consuming dense propellants also have a higher thrust-to-weight ratio, which reduces the mass of the main propulsion subsystem.
3. At least when compared to the example of the Shuttle Orbiter, the recovery mode/provisions chosen are competitive with a winged/lifting-body gliding return and horizontal landing. They are able to recover more mass, in addition to their own mass, than an equivalent system of wings, horizontal landing gear, and Shuttle-type TPS would.
4. Mixed-propulsion vehicles are smaller and lighter than pure-propulsion vehicles, achieve better relative payload performance, and are less sensitive to empty mass growth. Tripropellant vehicles are in turn superior to mixed-propulsion vehicles.
5. This concept has the potential to realize an almost two orders of magnitude reduction in launch costs compared with current expendable rockets, and to economically transport, over sufficiently many flights, very large masses to space.
6. Absolute payload performance is important for achieving reductions in payload-specific costs. For a given expenditure, a vehicle with a greater absolute payload may undercut another vehicle with a smaller absolute payload but superior relative payload performance, since it will not have to perform as many flights - and will therefore require fewer vehicles and engines to be manufactured - as its competitor.

5.02: Recommended course of action

1. The development of tripropellant engines should be pursued, since the best performance and lowest costs are achieved by the two tripropellant (Schemes 6 and 7) vehicles. Although the engines used in this analysis are baselined from existing new designs, new engines would probably have to be developed for this application, since they would be required to withstand a sufficient number of flights and be economically mass-producible.
2. As a backup, the vehicle may use a mixed or pure propulsion scheme if suitable tripropellant engines can not be obtained.

3. Apart from the engines, the concept vehicle varies little between propulsion schemes. There are no radical differences in configuration, and the basic technologies are the same. The same general effort can develop "bare-vehicle" technology that is compatible, albeit at different sizes, with a variety of different engines.

5.03: Recommendations for further research

1. For comparison with the results obtained, other options for space launch - either RLVs with different configurations, or even non-vehicle options - should be investigated, with an emphasis on achieving low payload transportation costs and high throughput.
2. The mass-production of sacrificial components - the forward shroud, HIAD and recovery parafoil - should be investigated in more detail, in order to improve cost estimates.
3. Likewise, the operational aspects of this concept should be investigated in more detail, again in order to better estimate costs.
4. The implications of very large programs, with large total production runs and high daily flight rates, must also be investigated.
5. The key technological prerequisities are improvements in manufacturing/materials processing for the airframe, suitable main engines, and the various aspects of the recovery provisions - primarily a suitable flexible TPS. These must all be further investigated.

Bibliography

[01] A.F. Dissel, "Comparative System Analysis of Reusable Rocket and Air-Breathing Launch Vehicles" (MS thesis), University of Maryland (College Park), 2005

[02] G.P. Sutton, O. Biblarz, "Rocket Propulsion Elements" (8th ed.), 2010, Wiley

[03] "Hydrogen delta-V (Henry Spencer; Mitchell Burnside Clapp)", sci.space.tech, http://yarchive.net/space/rocket/fuels/hydrogen_deltav.html

[04] Mark Wade, "Encyclopedia Astronautica - Atlas", http://www.astronautix.com/fam/atlas.htm

[05] Mark Wade, "Encyclopedia Astronautica - Atlas D", http://www.astronautix.com/lvs/atlasd.htm

[06] Mark Wade, "Encyclopedia Astronautica - SSME", http://www.astronautix.com/engines/ssme.htm

[07] Mark Wade, "Encyclopedia Astronautica - NK-33", http://www.astronautix.com/engines/nk33.htm

[08] V. Lukashevich, "Buran.ru - RD-701", http://www.buran.ru/htm/rd-701.htm

[09] Orloff, Benjamin S. "A Comparative Analysis of Single-Stage-to-Orbit Rocket and Airbreathing Vehicles" (MS thesis). AFIT/GAE/ENY/06-J13 Graduate School of Engineering and Management, Air Force Institute of Technology (AU), Wright-Patterson AFB, OH, June 2006.

[10] S. Gordon and B. J. McBride, "Computer Program for Calculation of Complex Chemical Equilibrium Compositions and Applications," NASA Reference Publication 1311 (1996).

[11] H.J. Allen and A.J. Eggers, Jr., "A study of the motion and aerodynamic heating of ballistic missiles entering the Earth's atmosphere at high supersonic speeds," N.A.C.A. Report 1381, 1958

[12] B.P. Smith, C.L. Tanner et al., "A historical review of inflatable aerodynamic decelerator technology development", 2010 IEEE Aerospace Conference, Big Sky, MT, IEEEAC 1276, March 2010

[13] Maryland Metrics, "Maryland Metrics - Screwjacks", mdmetric.com/prod/pti/Muli.pdf

[14] S.J. Hughes, F. McNeil Cheatwood, et al., "Hypersonic Inflatable Aerodynamic Decelerator (HIAD) Technology Development Overview", 21st AIAA Aerodynamic Decelerator Systems Technology Conference and Seminar, AIAA Paper No. 2011-2524, 2011

[15] M.K. McGuire, M.A. Covington, et al., "Flexible Ablative Thermal Protection Sizing on Inflatable Aerodynamic Decelerator for Human Mars Entry Descent and Landing", 49th AIAA Aerospace Sciences Meeting, AIAA Paper No. 2011-344, 2011

[16] M.C. Lindell, S.J. Hughes, "Structural Analysis and Testing of the Inflatable Re-entry Vehicle Experiment (IRVE)", 47th AIAA/ASME/ASCE/AHS/ASC Structures, Structural Dynamics and Materials Conference, AIAA Paper No. 2006-1803, 2006

[17] M.J. Grant, R.D. Braun, "Analytic Hypersonic Aerodynamics for Conceptual Design of Entry Vehicles", 48th AIAA Aerospace Sciences Meeting, AIAA Paper No. 2010-1212, 2010

[18] Aerospaceweb.org, "Hypersonic Waveriders - Flow Theory", http://www.aerospaceweb.org/design/waverider/theory.shtml

[19] T. Deschenes, "Development of a Hybrid Particle-Continuum Method", http://ngpdlab.engin.umich.edu/static-pages/hybrid-particle_continuum-simulation.html

[20] D.M. Curry, E.W. Stephens, "Apollo Ablator Thermal Performance at Superorbital Reentry Velocities", NASA Technical Note, TN-D5969, 1970

[21] R.N. Bell, "A Closed-Form Solution to Lifting Reentry", Air Force Flight Dynamics Laboratory Technical Report, AFFDL-TR-65-65, 1965

[22] J.S. Lingard, "Ram-Air Parachute Design", 13th AIAA Aerodynamic Decelerator Systems Technology Conference Precision Aerial Delivery Seminar, 1995

[23] Airborne Systems, "FireFly - Guided Precision Aerial Delivery System", http://www.airborne-sys.com/files/pdf/firefly_spec_sheet.pdf

[24] Airborne Systems, "DragonFly - Guided Precision Aerial Delivery System", http://www.airborne-sys.com/files/pdf/dragonfly_spec_sheet.pdf

[25] H. Stenzenberger, "BMI Resin Chemistry", https://polycomp.mse.iastate.edu/files/2012/01/6-Bismaleimide-Resins.pdf

[26] A. A. Case, "Permeability of hybrid composites subjected to extreme thermal cycling and low-velocity impacts" (MS thesis), Georgia Institute of Technology, 2004

[27] B.W. Grimsley, R.J. Cano et al., "Hybrid composites for LH2 fuel tank structure", NASA LaRC/MSFC, 2001

[28], S. Black, "An update on composite tanks for cryogens", High Performance Composites, Nov. 2005, http://www.compositesworld.com/articles/an-update-on-composite-tanks-for-cryogens

[29] Composite World Staff, "Fabrication methods", http://www.compositesworld.com/articles/fabrication-methods

[30] J. Cornforth, "The automation revolution", http://www.aero-mag.com/features/38/200910/62

[31] D.A. McCarville, J.C. Guzman, et al. "Manufacturing Overview of a 2.4 Meter (7.9 Foot) Composite Cryotank", SAMPE Journal, Sept./Oct. 2013

[32] T.F. Johnson, D.W. Sleight, R.A. Martin, "Structures and design Phase I summary for the NASA Composite Cryotank Technology Demonstrator project", NASA LaRC

[33] NASA, "NASA Completes Successful Battery of Tests on Composite Cryotank", NASA HQ/MSFC, 2014, http://www.nasa.gov/press/2014/august/nasa-completes-successful-battery-of-tests-on-composite-cryotank/

[34] "ASC completes world's largest autoclave", http://www.aschome.com/index.php/en/asc-completes-worlds-largest-autoclave

[35] "BMI and benzoxazine battle for future OOA aerocomposites", High-Performance Composites, Jan 2014

[36] J.K. Sutter, W.S. Kenner et al., "Comparison of autoclave and out-of-autoclave composites", NASA

[37] S.H. Levine, "Description of the S-IC Stage Structure", NASA contractor report, NASA-CR-153761 (Bellcomm, Inc.), 1967

[38] "15P165 Topol-M/MZKT-79221 walkaround", http://scalemania.ru/forum/viewtopic.php?f=26&t=58

[39] "MaritimeQuest - USS Samuel B. Roberts FFG-58", us_navy_pages/frigates/pages/samuel_b_roberts_ffg58_page_3.htm

[40] C.M. Green, M. Lomask, "Vanguard - A History", NASA Historical Series, SP-4202, 1969, http://history.nasa.gov/SP-4202/toc2.html

[41] Project 1947, "The RAND World-Circling Spaceship and the 1948 Chiles-Whitted 'rocketship' sighting", http://www.project1947.com/gr/worldcircling.htm

[42] Mark Wade, "Encyclopedia Astronautica - Douglas HATV", http://www.astronautix.com/lvs/doushatv.htm

[43] Mark Wade, "Encyclopedia Astronautica - Martin HATV", http://www.astronautix.com/lvs/marnhatv.htm

[44] Mark Wade, "Encyclopedia Astronautica - NAA HATV", http://www.astronautix.com/lvs/naahatv.htm

[45] G.C. Hudson, "History of the Phoenix VTOL SSTO and Recent Developments in Single-Stage Launch Systems", 4th International Space Conference of Pacific-basin Societies, AAS 91-643, 1991, http://www.spacefuture.com/archive/history_of_the_phoenix_vtol_ssto_and_recent_developments_in_single_stage_launch_systems.shtml

[46] M. Lindroos, "Introduction to future launch vehicle plans", http://www.pmview.com/spaceodysseytwo/spacelvs/index.htm

[47] Mark Wade, "Encyclopedia Astronautica - SASSTO", http://www.astronautix.com/lvs/sassto.htm

[48] Ninfinger Productions: Space Modelers Email Vault List, "Gemini in Neverland", http://www.ninfinger.org/models/vault/Gemini%20in%20Neverland/index.html

[49] Paul Drye, "SERV/MURP: Chrysler's Space Truck", https://falsesteps.wordpress.com/2012/08/18/servmurp-chryslers-space-truck/

[50] Mark Wade, "Encyclopedia Astronautica - MAKS", http://www.astronautix.com/lvs/maks.htm

[51] V. Lukashevich, "Buran.ru - MAKS", http://www.buran.ru/htm/molniya6.htm

[52] Mark Wade, "Encyclopedia Astronautica - RD-701", http://www.astronautix.com/engines/rd701.htm

[53] Office of Space Systems Development (NASA HQ), "Access to Space Study - Summary Report", NASA Technical Memorandum, NASA-TM-109693, 1994

[54] Mark Wade, "Encyclopedia Astronautica - DC-X", http://www.astronautix.com/lvs/dcx.htm

[55] Mark Wade, "Encyclopedia Astronautica - Millennium Express", http://www.astronautix.com/lvs/milpress.htm

[56] V. Pustonski, "Tallinn University of Technology - Introduction to Astronautics, Lecture 15", http://www.aai.ee/~vladislav/Astronautics_Lecture15.pps

[57] R. Rohrschneider, "Development of a Mass-Estimating Relationship Database for Launch Vehicle Conceptual Design" (MS thesis), Georgia Institute of Technology, 2002

[58] D. Wright, "Thin Shells of Revolution - Heads", http://www-mdp.eng.cam.ac.uk/web/library/enginfo/textbooks_dvd_only/DAN/pressVessels/shells/shells.html

[59] E. Stump, "All about learning curves," http://www.galorath.com/images/uploads/LearningCurves1.pdf

[60] Engineering Toolbox, "Present value", http://www.engineeringtoolbox.com/discount-rate-d_1232.html

[61] G. Gstattenbauer, "Cost Analysis of Launch Vehicles" (MS thesis), AFIT/GAE/ENY/06-10. Graduate School of Engineering and Management, Air Force Institute of Technology (AU), Wright-Patterson AFB, 2006.

[62] W. Heienman, Jr. "Design Mass Properties II - Mass Estimating and Forecasting for Aerospace Vhielces Based on Historical Data", NASA JSC, JSC-26098, 1994

[63] Elon Musk, "Prepared Statement by Elon Musk at a Senate Hearing on Space Shuttle and the Future of Space Launch Vehicles", Senate Committee on Commerce, Science and Transportation, 2004, http://www.spaceref.com/news/viewsr.html?pid=12774

[64] Mark Wade, "Encyclopedia Astronautica - OTRAG", http://www.spaceref.com/news/viewsr.html?pid=12774

[65] J. Deschamps, "Measurements of the Great Pyramid", http://repertorium.net/rostau/measures.html

[66] U.S. Department of Commerce Bureau of Economic Analysis, "Widespread But Slower Growth in 2013", news release (2014.06.11), http://www.bea.gov/newsreleases/regional/gdp_state/gsp_newsrelease.htm

[67] Central Intelligence Agency, "The World Factbook 2013-2014", https://www.cia.gov/library/publications/the-world-factbook/index.html

[68] Air Products, "Safetygram 6 - Liquid oxygen", http://www.airproducts.com/~/media/Files/PDF/company/safetygram-6.pdf

[69] Pollet Research, "Energy data - liquid hydrogen", http://www.brunopolletresearch.com/Energy_Data.pdf

[70] Air Liquide, "Gas Encyclopedia - Methane", http://encyclopedia.airliquide.com/Encyclopedia.asp?GasID=41

[71] Defense Logistics Agency, "Aerospace Energy Standard Prices - Prices for FY 2012 Effective Oct 1, 2011", http://www.energy.dla.mil/customers/standard_prices/Documents/Aerospace%20Energy%20Standard%20Prices/Prices%20for%20FY%202012%20Effective%201%20Oct%2011%20R.pdf

[72] U.S. Department of Labor Bureau of Labor Statistics, "CPI Inflation Calculator", http://data.bls.gov/cgi-bin/cpicalc.pl

[73] J. Hulka, J.S. Forde et al. "Modification and Verification Testing of a Russian NK-33 Rocket Engine for Reusable and Restartable Applications", 34th AIAA/ASME/ASEE Joint Propulsion Conference and Exhibit, AIAA Paper No. 98-3361, 1998

[74] N. Brügge, "Russian/Ukrainian space-rocket and missile liquid-propellant engines", http://www.b14643.de/Spacerockets_1/Diverse/Russian_Rocket_engines/engines.htm

[75] United Technologies Corporation, "Design and Analysis Report For the RL10-IIB Breaboard Low Thrust Engine - Final Report", NASA contractor report, NAS3-24238, 1984

[76] Mark Wade, "Encyclopedia Astronautica - RL-10B-2", http://www.astronautix.com/engines/rl10b2.htm

[77] Mark Wade, "Encyclopedia Astronautica - RL-10A-3", http://www.astronautix.com/engines/rl10a3.htm

[78] University of Washington Center of Excellence for Advanced Materials in Transport Aircraft Structures, "CLT" (computer program), https://depts.washington.edu/amtas/courses/computer.html

[79] Hexcel Corporation, "HexTow IM10 Carbon Fiber Product Data", http://www.hexcel.com/resources/datasheets/carbon-fiber-data-sheets/im10.pdf

[80] Cytec Engineering Materials, "CYCOM 5250-4 Prepreg System Technical Data Sheet", http://www.argosyinternational.com/sites/default/files/datasheet/CYCOM_5250-4_032012.pdf

[81] Mark Wade, "Encyclopedia Astronautica - R-40A", http://www.astronautix.com/engines/r40a.htm

Appendix A: Propulsion information

A.01: Propellant data

Table A.01-01: Physical properties of propellants [68][69][70]

Propellant	Temperature (1 atm)	Density	Lower heating value
LO_2	90 K	1141.00 kg/m^3	N/A
LH_2	20 K	70.85 kg/m^3	119.96 MJ/kg
RP−1	Non-cryogenic	820.00 kg/m^3	43.00 MJ/kg
LCH_4	110 K	422.36 kg/m^3	50.00 MJ/kg

Table A.01-02: Propellant costs [71]

Propellant	Cost (2014 USD/kg)
LO_2	$00.14/kg
LH_2	$10.08/kg
RP−1	$02.23/kg
LCH_4	$01.67/kg

These costs have been adjusted to 2014 values based on the Consumer Price Index [72].

A.02: Ascent engine baselines

A.02.01: Aerojet Rocketdyne RS-25 SSME

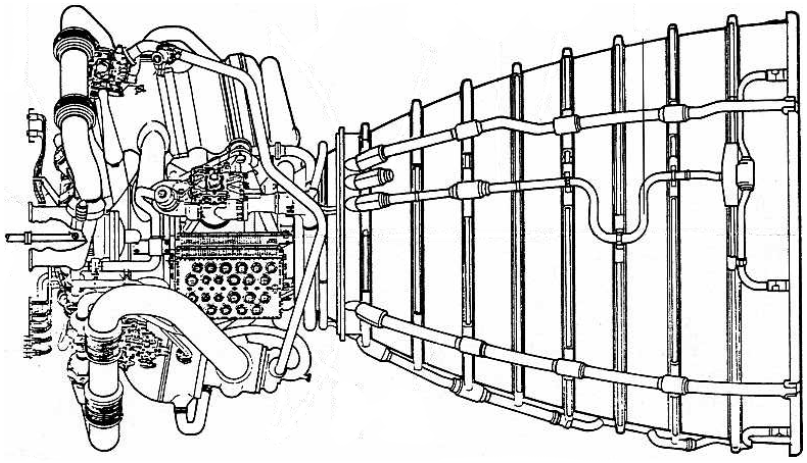

Figure A.02.01-01: The SSME

Table A.02.01-01: SSME engine data [06]

Engine mass	3526 kg
Length	4.27 m
Diameter	2.44 m
LO2 flowrate (100% RPL)	405.4 kg/s
LH2 flowrate (100% RPL)	067.3 kg/s
Throttle range	067% - 109%
Chamber pressure (100% RPL)	190.3 bar
Performance, sea level	366.0 s (1696.6 kN)
Performance, vacuum	452.3 s (2096.7 kN)

A.02.02: OKB-276/OAO Kuznetsov NK-33/Aerojet AJ-26

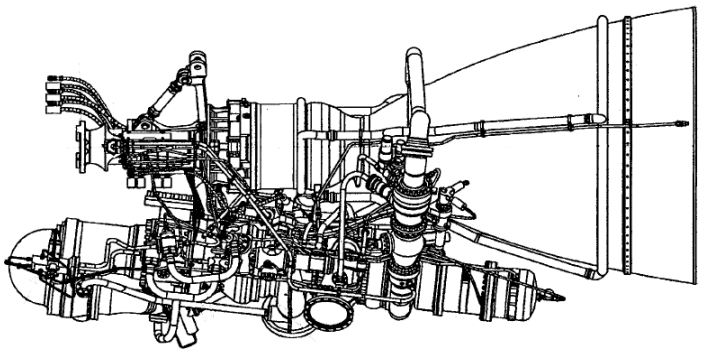

Figure A.02.02-01: The NK-33 [73]

Table A.02.02-01: NK-33 engine data [07][73]

Engine mass	1235 kg/1300 kg
Length	3.32 m/4.27 m
Diameter	1.49 m
LO2 flowrate (100% RPL)	374.2 kg/s
RP-1 flowrate (100% RPL)	144.7 kg/s
Throttle range	049% - 135%
Chamber pressure (100% RPL)	145.2 bar
Performance, sea level	297.0 s (1511.3 kN)
Performance, vacuum	331.0 s (1684.3 kN)

Table A.02.02-02: NK-33 (metholox) engine data [10][73]

Engine mass	1285 kg/1350 kg
Length	3.32 m/4.27 m
Diameter	1.49 m
LO2 flowrate (100% RPL)	374.2 kg/s
LCH4 flowrate (100% RPL)	106.9 kg/s
Throttle range	049% - 135%
Chamber pressure (100% RPL)	145.2 bar
Performance, sea level	306.0 s (1443.7 kN)
Performance, vacuum	341.5 s (1611.2 kN)

A.02.03: OKB-456/NPO Energomash RD-704

Figure A.02.03-01: Energomash RD-704 [74]

Table A.02.03-01: Energomash RD-704 engine data [08]

Parameter	Mode 1	Mode 2
Mass	2000 kg	2000 kg
Length	4.3 m	4.3 m
Exit OD	1.8 m	1.8 m
Nozzle ratio	70:1	70:1
Chamber pressure	290 bar	122 bar
Mass flow rate, LO2	388.4 kg/s	148.5 kg/s
Mass flow rate, LH2	029.5 kg/s	024.7 kg/s
Mass flow rate, RP-1	073.7 kg/s	N/A
Performance, sea level	330.0 s (1590.9 kN)	353.4 s (600.3 kN)
Performance, vacuum	402.7 s (1941.4 kN)	460.0 s (781.3 kN)

Table A.02.03-02: RD-704 (hydrometholox) engine data [08][10]

Parameter	Mode 1	Mode 2
Mass	2100 kg	2100 kg
Length	4.3 m	4.3 m
Exit OD	1.8 m	1.8 m
Nozzle ratio	70:1	70:1
Chamber pressure	290 bar	122 bar
Mass flow rate, LO2	388.4 kg/s	148.5 kg/s
Mass flow rate, LH2	029.5 kg/s	024.7 kg/s
Mass flow rate, CH4	060.4 kg/s	N/A
Performance, sea level	337.1 s (1581.2 kN)	353.4 s (600.3 kN)
Performance, vacuum	418.0 s (1960.6 kN)	460.0 s (781.3 kN)

A.02: Secondary propulsion baselines

A.02.01: RL10 OMS

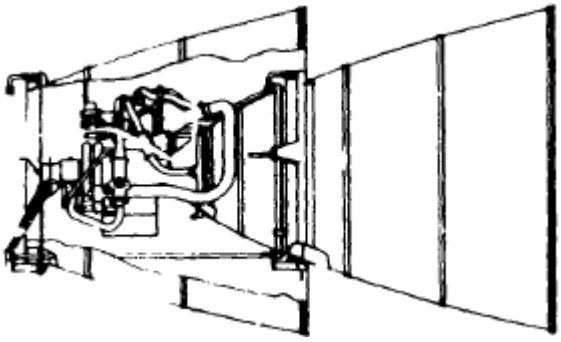

Figure A.02.01-01: The RL10B-2 [75]

Table A.02.01-02: RL10B-2 engine data [76]

Mass	277 kg
Length	4.14 m
Diameter	2.13 m
O/F ratio	5.85:1
Specific impulse	460 s
Thrust	11 kN

A.02.02: RCS

Table A.02.02-01: RCS thruster baseline characteristics [77]

Mass	110 kg
Length	1.03 m
Diameter	0.60 m
O/F ratio	5.85:1
Chamber pressure	32.3 bar
Specific impulse	415 s
Mass flow rate	6 kg/s
Thrust	6000 N

Appendix B: Input mass properties

B.01: Airframe data

Table B.01-01: Properties of structural laminates [78][79][80]

Description	Axial strength	Hoop strength	Density	Safety factor
ITS barrels	250 MPa	500 MPa	1574 kg/m^3	1.25
ITS domes	400 MPa	400 MPa	1574 kg/m^3	1.25
Secondary tanks	400 MPa	400 MPa	1574 kg/m^3	3.00

Table B.01-02: Airframe geometric data

Structure	Smeared thickness
Forward shroud	2.5 mm
Base fairing	2.5 mm
Aft heatshield	2.5 mm

The forward TPS unit weight is 2.5 kg/m^2.

B.02: HIAD data

Table B.02-1: Properties of windward TPS ablator [15]

Thickness	15 mm
Bulk density	160 kg/m^3

Table B.02-2: HIAD material mechanical properties [16]

Description	Material density	Isotropic tensile strength
Restraint layer	560.6 kg/m^3	493.7 MPa
Bladder	1091.0 kg/m^3	380.5 MPs

Appendix C: Sample detailed results

C.01: Tripropellant hydrometholox vehicle

These data pertain to the tripropellant hydrometholox vehicle (Scheme 7), which was found to be the best performer.

Table C.01-01: Mass statement/general data

Engines	20 × RD−704 (metholox)
Length (body - nose to gimbal plane)	47.13 m
Length (OAL - nose to exit plane)	51.43 m
Body (ITS) diameter	15.50 m
Base (fairing) diameter	19.00 m
XAC diameter	7.20 m
HAD diameter	77.86 m
GTOM	3102731 kg
Empty mass	200222 kg
Payload (200 km × 200 km at 19.4°)	58136 kg
Payload (200 km × 200 km at 90.0°)	22506 kg
Total propellants (polar ascent)	1983363 kg
LO_2, ascent	2316487 kg
LH_2, ascent	176189 kg
LCH_4, total	361314 kg
LO_2, secondary	21826 kg
LH_2, secondary	4187 kg
Enclosed volume, ITS LO_2 container	2091.18 m^3
Enclosed volume, ITS LH_2 container	2597.84 m^3
Enclosed volume, secondary LO2 containers	19.52 m^3
Enclosed volume, secondary LH2 containers	60.30 m^3
Enclosed volume, LCH_4 containers	872.92 m^3
Total main engine V_Δ	9365 — 9803 m/s
Useful velocity	7402 — 7840 m/s
Gravity losses	1376 m/s
Drag losses	180 m/s
Back-pressure losses	215 m/s
Margin	192 m/s

Table C.01-02: Empty mass breakdown

Main propulsion	**59231**	kg
Main engines	46200	kg
Actuators	4400	kg
Propellant feed system	5405	kg
Purge, pressurization and dump	3226	kg
Secondary propulsion	**11911**	kg
OMS engines	454	kg
Attachment hardware	336	kg
RCS engines	232	kg
Attachment hardware	172	kg
Gas generators	200	kg
Accumulators, GO2	557	kg
Accumulators, GH2	1524	kg
Secondary tanks, LO2	173	kg
Secondary tanks, LH2	534	kg
Tanks, RP-1 (landing)	7729	kg
Body	**55892**	kg
ITS structure	31352	kg
Anti-slosh, oxidizer	2900	kg
Anti-vortex, oxidizer	259	kg
Anti-slosh, fuel	14	kg
Anti-vortex, fuel	117	kg
Thrust structure	6666	kg
Aft fairing	1505	kg
Base heatshield	1169	kg
Payload shroud	3942	kg
Payload provisions	2000	kg
Forward TPS	5968	kg
Recovery provisions	**40840**	kg
Extensible aft centerbody	709	kg
Screwjack extenders	12024	kg
HIAD TPS	13855	kg
HIAD bladder	3167	kg
HIAD restraint wrap	1976	kg
Landing parafoil system	5693	kg
Landing gear	3416	kg
Other	**9245**	kg
Avionics	1000	kg
Electrical power subsystem	4945	kg
Hydraulic system	3300	kg
Margin	**23103**	kg
Total	**200222**	kg